R-00-14

Modelling of the site scale hydrogeological situation at Beberg using NAMMU

Niko Marsic, Björn Gylling, Bertil Grundfelt
Kemakta Konsult AB

Lee Hartley
AEA Technology, UK

February 2000

Svensk Kärnbränslehantering AB
Swedish Nuclear Fuel
and Waste Management Co
Box 5864
SE-102 40 Stockholm Sweden
Tel 08-459 84 00
+46 8 459 84 00
Fax 08-661 57 19
+46 8 661 57 19

ISSN 1402-3091
SKB Rapport R-00-14

Modelling of the site scale hydrogeological situation at Beberg using NAMMU

Niko Marsic, Björn Gylling, Bertil Grundfelt
Kemakta Konsult AB

Lee Hartley
AEA Technology, UK

February 2000

ISSN 1402-3091
SKB Rapport R-00-14

Modelling of the site scale hydrogeological situation at Beberg using NAMMU

Niko Marsic, Björn Gylling, Bertil Grundfelt
Kemakta Konsult AB

Lee Hartley
AEA Technology, UK

February 2000

Abstract

The purpose of the present study is to perform modelling of the site scale hydro-geological situation at Beberg using the finite element code NAMMU and compare the results with those from HYDRASTAR reported in SR 97. NAMMU was used in the large scale regional hydrogeological modelling at Beberg. The hypothetical repository layout at Beberg is based on geological data from the Finnsjön site.

Four model variants were created in this study. Two variants were compared with the deterministic freshwater case in the HYDRASTAR modelling. The other two variants were created to study the effect of a regionally distributed permeability anisotropy and variable-density groundwater on the groundwater flow pattern. These processes are not considered in HYDRASTAR.

The NAMMU results, including the pathline patterns, agree with those from the HYDRASTAR modelling. The effect of anisotropy and saline groundwater is found significant for the pathlines.

The difference in canister flux between the NAMMU and the HYDRASTAR models is small, while the difference in travel time is more significant. The discrepancies between the results from the NAMMU and the HYDRASTAR simulations can be ascribed to the different numerical discretisation, i.e. different representation of the permeability, and the different pathline algorithms used in the two models.

Sammanfattning

Syftet med den aktuella studien är att utföra modellering av de hydrogeologiska förhållandena för Beberg på lokal skala med FEM-koden NAMMU och jämföra resultaten med de från HYDRASTAR som rapporterades i SR 97. NAMMU användes vid studien av de regionala hydrogeologiska förhållandena för Beberg. Den hypotetiska förvarsplatsen Beberg är baserad på data från Finnsjöområdet.

Fyra modellvarianter har studerats. Två av varianterna jämfördes med den deterministiska sötvattenvarianten i HYDRASTAR-modelleringen. I de två övriga varianterna studerades effekten av regional hydraulisk anisotropi och grundvatten med variabel densitet på grundvattnets flödesmönster. Dessa processer beaktas inte i HYDRASTAR.

NAMMU-resultaten, inklusive flödesmönstren, överensstämmer med de från HYDRASTAR-modelleringen. Effekten av anisotropi och salt grundvatten på partikelbanorna är betydande.

Skillnaden i beräknade flöden mellan NAMMU- och HYDRASTAR-modellerna är liten medan skillnaden i gångtider är mer påtaglig. Avvikelserna mellan resultaten från NAMMU- och HYDRASTAR-simuleringarna kan tillskrivas sättet att representera permeabiliteten samt de algoritmer som används för att beräkna partikelbanor i de två modellerna.

Executive Summary

The purpose of the present study is to perform modelling of the site scale hydro-geological situation at Beberg using the finite element code NAMMU and compare the results with those from HYDRASTAR reported in SR 97. NAMMU was used in the large scale regional hydrogeological modelling at Beberg. The hypothetical repository layout at Beberg is based on geological data from the Finnsjön site.

Variants

Four model variants were created in this study:

- *Base Case*
- *BaseFine Case*
- *Anisotropic Case*
- *Saline Case*

Only the BaseFine Case variant used the same discretisation as the HYDRASTAR model. In the other variants, the discretisation was coarser, reduced by a factor of 2 in the horizontal directions. In the same way as for the HYDRASTAR model, the boundary conditions in this study were taken from the output of the regional scale modelling for Beberg. The permeability field was imported from the HYDRASTAR model assuming a constant fluid density and viscosity.

The Base Case and the BaseFine Case variants were compared with the deterministic freshwater case in the HYDRASTAR modelling, Variant 4. In the Anisotropic Case, the effect of a regionally distributed permeability anisotropy on the groundwater flow pattern was studied. The direction of the major axis of anisotropy was set to N 45 W and the magnitudes of the diagonal components of the permeability tensor were set to 10:1:1 (*horizontal major:horizontal minor:vertical*). In the Saline Case, the effect of the presence of a variable-density groundwater was studied.

Results

For the three freshwater variants, the pathlines are predominantly directed to the northeast through the rock mass away from the repository. This is also in accordance to the regional flow pattern of the surface water runoff. The discharge areas are found around the regional fracture zones situated northeast of the repository. The major part of the released particles exits within the Imundbo Zone and Zone 1. Some particles follow the subhorizontal Zone 2 up to the top of the model domain. These are the particles with the shortest travel times, typically less than 10 years.

The effect of anisotropy and saline groundwater is found considerable on the pathlines. The presence of anisotropic hydraulic permeability drives the pathlines in the direction of the major axis of the anisotropy. The effect of the fracture zones is hereby enhanced in those cases the fractures are aligned parallel to the major axis of anisotropy. In the Saline Case, the presence of the dense saline groundwater is changing the flow field completely compared to the other variants. In this case, the particles travel straight

downwards through the model domain in an almost vertical direction. Hence, the major part of the released particles exits through the bottom of the model.

The pathline patterns for the Base Case, the BaseFine Case and the Saline Case correspond to the results from the HYDRASTAR modelling. The statistical summaries based on the results from the 120 released particles for all variants are presented in Table 1 and Table 2.

Table 1 **Statistical summary for the Base Case, the Anisotropic Case and the Saline Case. The travel time is based on the pathlines exiting through the top of the model domain.**

Statistics		Base Case	Anisotropic Case	Saline Case
$\log_{10}$(Travel Time)	Median	1.751	1.930	1.709
	25th Percentile	1.396	1.821	1.686
	75th Percentile	2.009	2.099	1.714
Fraction exiting through the top		0.858	1.000	0.067
$\log_{10}$(Canister Flux)	Median	-2.754	-2.795	-2.424
	25th Percentile	-2.855	-2.895	-2.506
	75th Percentile	-2.587	-2.624	-2.346

Table 2 **Statistical summary for the BaseFine Case (NAMMU) and Variant 4 (HYDRASTAR). The travel time is based on the pathlines exiting through the top of the model domain.**

	BaseFine Case, NAMMU		Variant 4, HYDRASTAR	
Statistics	**$\text{Log}_{10}(TT_{top})$**	**Log_{10}(CF)**	**$\text{Log}_{10}(TT_{top})$**	**Log_{10}(CF)**
Median	1.828	-2.706	1.433	-2.732
25th Percentile	1.510	-2.837	1.230	-2.817
75th Percentile	1.958	-2.503	1.631	-2.529
Fraction exiting through the top	0.917	-	1.000	-

The median canister flux is $1.9 \cdot 10^{-3}$ - $2.0 \cdot 10^{-3}$ m^3/m^2,year and the difference between the models is much smaller than the variance of the canister flux. The median travel time is 67 years in the BaseFine Case and 27 years in the HYDRASTAR Variant 4, i.e. a factor 2.5 longer travel times in the BaseFine Case. The difference is expected to be larger than for the canister flux, since the calculation of pathlines is more sensitive to the variations in a heterogeneous permeability field. The discrepancies between the results from the NAMMU and the HYDRASTAR simulations can be ascribed the different numerical discretisation, i.e. different representation of the permeability and the different pathline algorithms used in the two models.

Contents

List of Figures

Figures in Appendix

List of Tables

Tables in Appendix

1 Background and Objectives

The Swedish Nuclear Fuel and Waste Management Company (SKB) has completed a safety assessment project called SR 97 wherein a study of three hypothetical repositories in Sweden for spent nuclear fuel has been conducted. The three sites are entitled Aberg, Beberg and Ceberg, which are based on data from the three real sites Äspö, Finnsjön and Gideå respectively where SKB has performed extensive investigations. Hydrogeological modelling has been performed for each of the three sites where the possible transport of radionuclides from the stored waste packages through the host rock has been examined.

The present study is not considered a part of SR 97. The work is meant to be a comparison to the Beberg site scale hydrogeological modelling that is performed with HYDRASTAR in SR 97. In this study, the finite element code NAMMU *[Cliffe et al., 1995]* is used. This was the code used in the investigation of the large scale regional hydrogeological situation at Beberg *[Hartley et al., 1998]*. Because of the more extensive technical capabilities of NAMMU compared to HYDRASTAR, some model variants that are not encompassed by the HYDRASTAR modelling are studied as well. These variants include the effects of anisotropy and salinity on the groundwater flow patterns.

The main objectives of this study are to:

1. Perform a comparison of the results computed by NAMMU and HYDRASTAR for a deterministic case without the effects of anisotropy or variable-density flow. These variants are called the Base Case and BaseFine Case respectively.

2. Study the effect of hydraulic anisotropy on the groundwater flow pattern in the model set up for the Base Case. This variant is called the Anisotropic Case.

3. Study the effect of the presence of a variable-density flow pattern in the model set up for the Base Case. This variant is called the Saline Case.

In addition to this, the tools used for modelling and visualisation are evaluated. The study is divided into the following major sections:

Sections 2 and 3 introduce the Beberg Site and the Model Data used
Section 4 presents the Base Case simulation.
Section 5 presents the BaseFine Case simulation.
Section 6 presents the Anisotropic Case simulation.
Section 7 presents the Saline Case simulation.
Section 8 summarises and discusses the study results.
Section A1 presents an analysis of the discrepancies between the models.
Section A2 contains a performance test on the iterative solver.
Section A3 discusses the tools used.
Section A4 contains Quality Assurance with a list of files and figures produced.

2 Introduction

2.1 The Beberg Site

Beberg is based on the hydrogeological investigations in the Finnsjön area, which is located in the northern part of Uppland in central Sweden, see Figure 2-1. Forsmark, the SKB Final Repository for Radioactive Operational Waste (SFR) is located 15 km northeast of the Finnsjön area, which is one of the most investigated study areas in the SKB program. From a hydrogeological perspective, northern Uppland is notable for the occurrence of saline groundwater at relatively shallow depths and for the presence of relatively shallow subhorizontal fracture zones. The ground surface of the region has little relief, the average elevation of the Finnsjön region is 30 masl ± 30 m and the regional hydraulic gradient is about 0.2-0.3% for the shallow groundwater. The general pattern of surface drainage is toward the Bothnian Sea in the northeast.

The coordinate system used is the National Swedish RAK-system, with offset in East-West of 1 600 000 m and in North-South of 6 600 000 m. All plots in this report refer to this coordinate system.

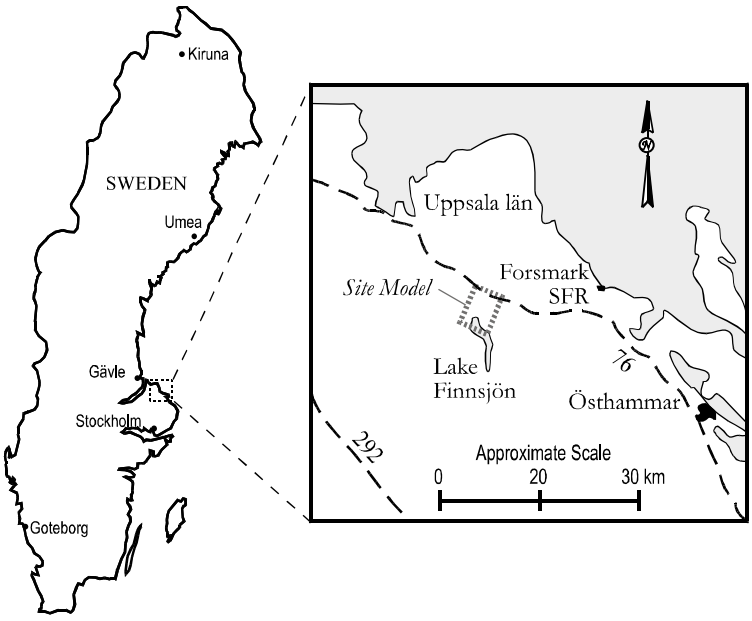

Figure 2-1 Location of the Beberg site.

The current knowledge about this site has been summarised by *Walker et al. [1997]* in a report that serves as a handbook for hydrogeologic modelling at the three hypothetical sites Aberg, Beberg and Ceberg.

2.2 Modelling and Presentation Software

The modelling of the groundwater flow has been carried out with the finite element code NAMMU that uses a porous medium approach. The computer used was a Silicon Graphics Power Challenge at AEA Technology.

The major part of the post-processing has been carried out with the program AVIZIER *[http://www.bssi.no/]*. AVIZIER is a software environment for three-dimensional visualisation of geoscience data developed by Bergen Software Services International A/S, BSSI in Bergen, Norway. AVIZIER is built using the software system Iris Explorer from NAG *[http://www.nag.co.uk/]*.

The commercial statistical data analysis software Statistica *[http://www.statsoft.com/]* has been used for the statistical analysis of the travel times and canister fluxes of the released pathlines. The script developed for the analysis is described by *Marsic [1998]*.

2.3 Regional Model

A modified version of the original regional Beberg model AltK provided by *Hartley et al. [1998]* was used to generate boundary conditions for the site scale model. The AltK variant is an alternative conceptual model suggested by *Walker et al. [1997]* in order to address the conceptual uncertainty associated with the structural model for the fracture zones. The regional base case model for the fracture zones, RCD1, proposed that the permeability of the fracture zones be constant with depth. The AltK model uses a depth dependent permeability for both the fracture zones and the rock mass. A few changes were made to the original AltK regional model in order to meet the restrictions within HYDRASTAR, see below.

The original AltK regional model variant calculated the evolution of groundwater flow and salinity from 4000 years BP to the present day. This gave a prediction of the current groundwater head and salinity distribution. In the site scale modelling with HYDRASTAR it was necessary to use steady state constant density models. This conceptual difference necessitates an approximate method in deriving the site scale boundary conditions from the larger regional scale model. Two approximation methods are considered. The first is to recalculate the AltK variant for a steady state freshwater flow condition. The results are used here generating the residual pressure boundary conditions of the Base Case, the BaseFine Case and the Anisotropic Case. The second is to use the current day variable-density flow, as predicted by the original AltK regional model. The model predictions of the residual pressure and salinity at the present day are used as boundary conditions in the Saline Case.

Since it is usually much easier to choose adequate boundary conditions for a larger model, the nested modelling approach used here makes it possible to apply a set of realistic Dirichlet (prescribed head) boundary conditions for the site scale model.

The boundary conditions for the freshwater case in **the regional model** are:

1. topographic (prescribed) head boundary conditions on the top surface

2. hydrostatic hydraulic head on the vertical sides

3. no flow across the base

The Dirichlet boundary conditions for the site scale model were taken from the regional model, see section 3.3.

3 Site Scale Model

3.1 Model Domain

The boundaries of the site scale model were chosen to be the same as in the HYDRASTAR model for the site scale. This means that a regular three dimensional grid with rectangular blocks was used. The HYDRASTAR model uses a block side size of 35 m in all three dimensions.

The origin of the model is located at (14050, 94610, -1505) m in RAK with the earlier given offset and rotated 14° clockwise in the horizontal plane. From the origin, the model extends (4130, 5355, 1505) m in the x, y and z direction respectively. This means that the HYDRASTAR model contains (118, 153, 43) cells in the three directions respectively. The model domain and the deposition tunnels in the northern and the southern blocks are shown in Figure 3-1.

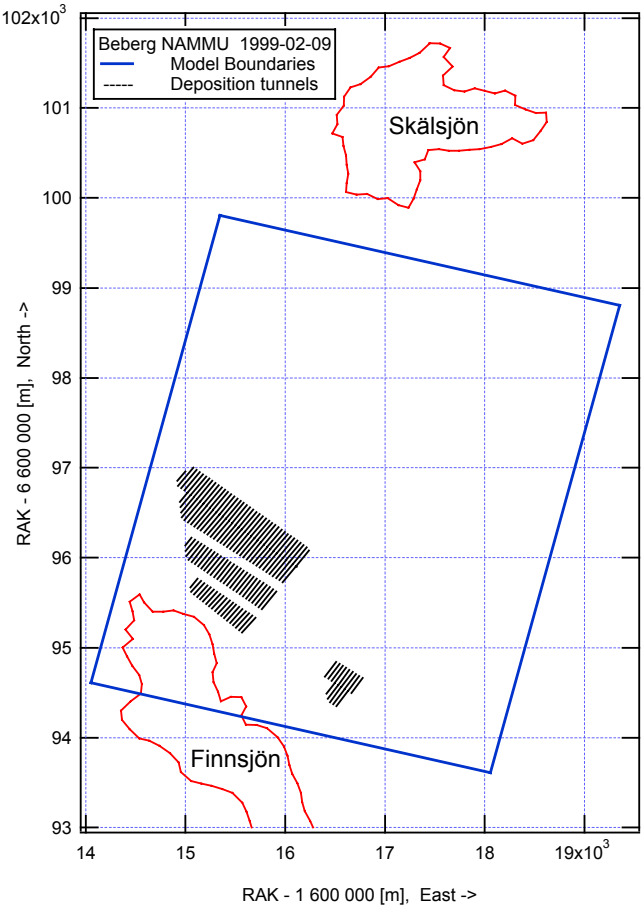

Figure 3-1 *Beberg site scale model domain (blue line). Tunnels of the hypothetical repository at -600 masl are shown projected to ground surface (Plan view, RAK- coordinate system with local off-set).*

The fracture zone representation within the site scale model is shown in Figure 3-2 and Figure 3-3.

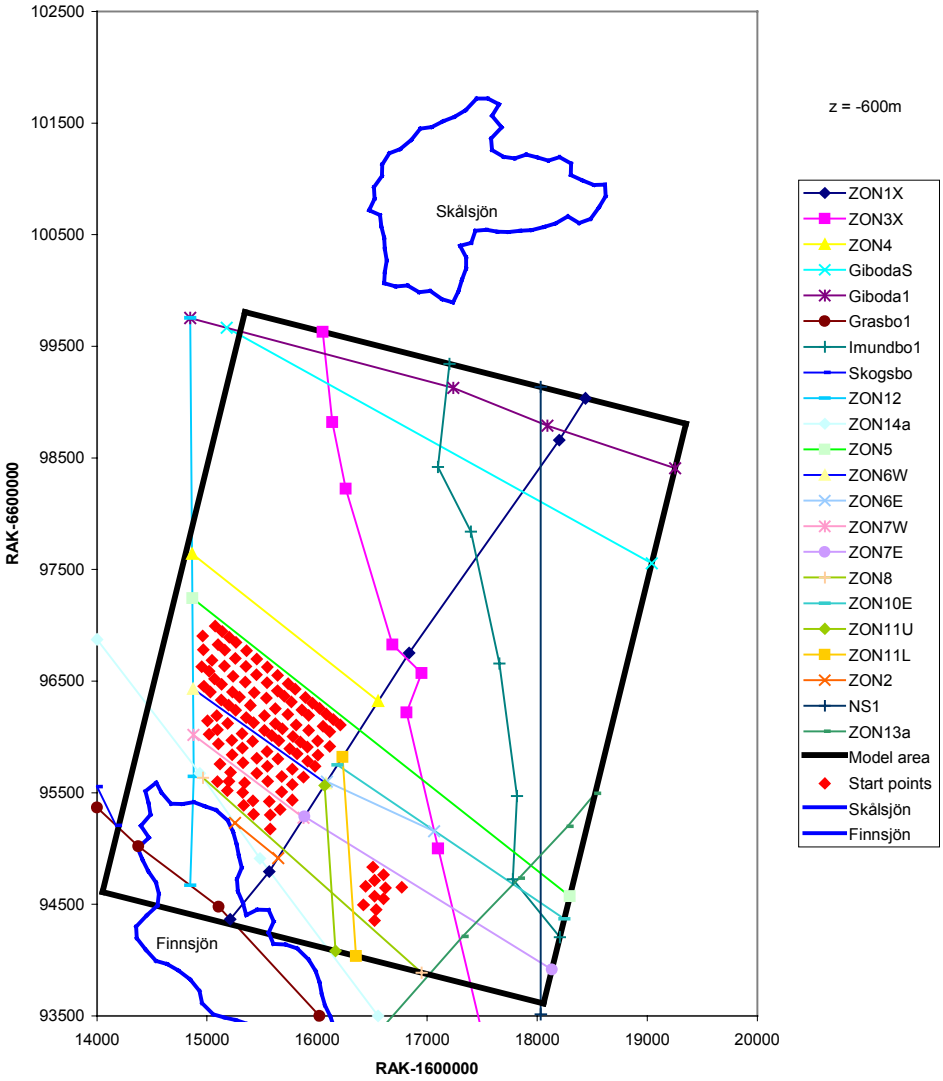

Figure 3-2 *Plan view of the site scale model for Beberg at the depth of the repository (-600 m). The fracture zone representation within the model is shown in the picture. All starting positions for the particle tracking are marked with a point.*

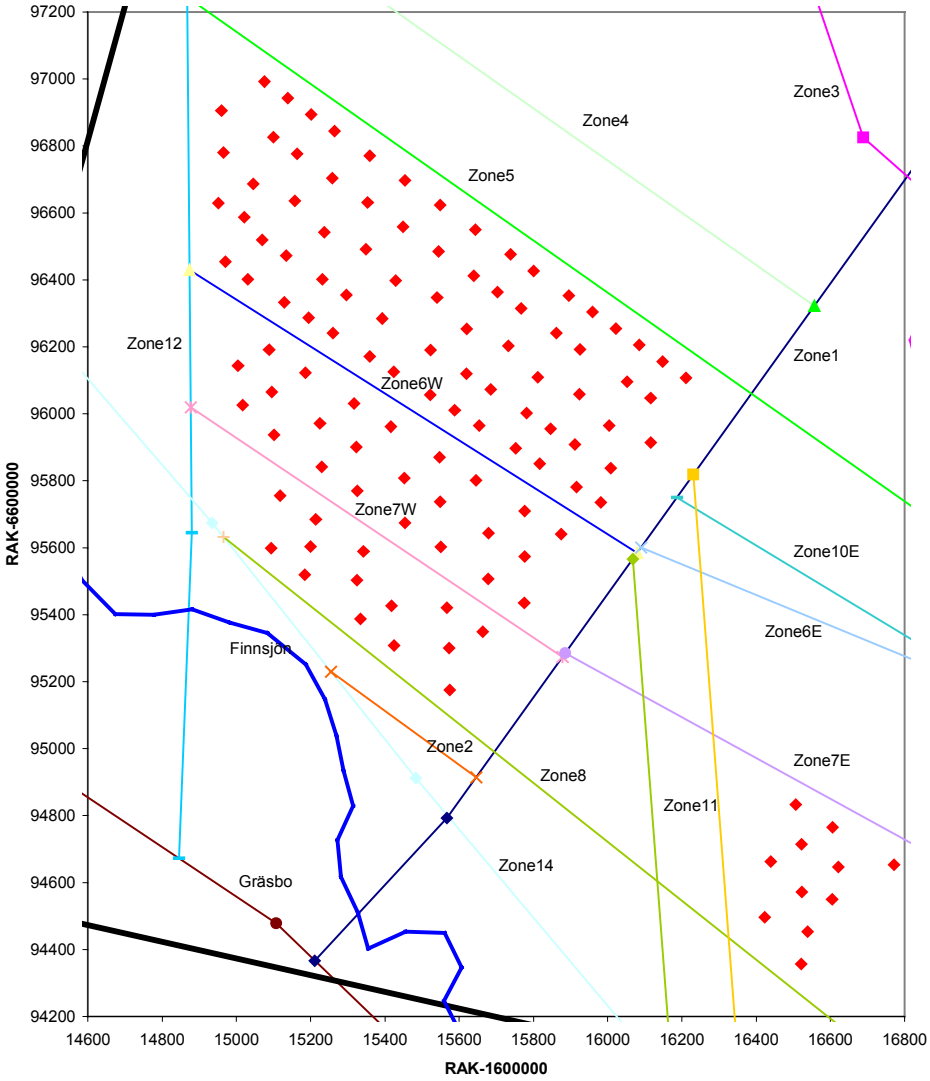

Figure 3-3 *Plan view of the repository area within the site scale model for Beberg at the depth of the repository (-600 m). All starting positions for the particle tracking are marked with a point.*

3.1.1 Base Case, Anisotropic Case and Saline Case

The direct solver in NAMMU, used for the three variants Base Case, Anisotropic Case and Saline Case, uses a lot of memory and is quite slow for large problems. A practical limit in model size is reached at a level of about 400 000 elements. To avoid this problem a change was made to the model to reduce the large number of elements. In these three variants, the discretisation was reduced by a factor two (2) in the x and y directions compared to the HYDRASTAR model (the number of elements is reduced by a factor four (4)). This gives a block size of 70×70×35 m in the x, y and z directions respectively for the three NAMMU models and causes the coarse NAMMU models to be 35 m shorter in the y direction due to the lower discretisation used.

3.1.2 BaseFine Case

At a later stage in the project, a new iterative solver together with a preconditioner (GMRES/ILU) was implemented into NAMMU. This new solver reduced the execution times by a factor of up to 300 compared to the direct solver. In addition, the memory requirements for this solver are much lower than with the direct solver. This made it possible to run the model with full discretisation (i.e. the same as the HYDRASTAR model). The iterative solver was only used for the BaseFine Case where a block side size of 35 m in all three directions was used.

3.2 Permeability Field

The permeability values used in the NAMMU models were imported from HYDRASTAR. NAMMU uses the permeability tensor in the formulation of the groundwater flow equation. Since HYDRASTAR uses the hydraulic conductivity in the equations, the values imported to NAMMU from HYDRASTAR had to be converted to permeability values. The conversion was done with the use of the following equation,

$$K = k \frac{\mu}{\rho g}$$

where K is the specific permeability, k the hydraulic conductivity, μ the viscosity of the water, ρ the density of the water and g the gravitation (μ and g were assumed to be constant). For the sake of convenience and because of the presence of salt in some of the models, only the term permeability will be used when talking about the hydraulic conductivity (used in HYDRASTAR) and the permeability (used in NAMMU) in the remainder of the report.

3.2.1 Base Case

The permeability field used for the Base Case was imported from the HYDRASTAR Deterministic Case. In the process of exporting the permeability field from HYDRASTAR to NAMMU two significant compromises were necessary:

1. Averaging the directional components of the HYDRASTAR permeability field.

2. Upscaling the HYDRASTAR permeability to the larger NAMMU element size.

Relating to (*1*) above, the values exported from HYDRASTAR are actually not equal to the ones HYDRASTAR uses in the calculations but correspond to the ones that are generated for the visualisation of the HYDRASTAR permeability field with the AVS application HYDRAVIZ *[Hultman, 1997]*. In HYDRASTAR, the permeability is defined along connections between the nodes in the rectangular grid, see Figure 3-4. For visualisation purposes, these permeability values are replaced by calculating the resultant for the three permeability values corresponding to each node and then assigning this value to the element volume defined by the three directions in the grid, see Figure 3-5. The resultant is calculated as,

$$k_{AVS} = \sqrt{k_X^2 + k_Y^2 + k_Z^2}$$

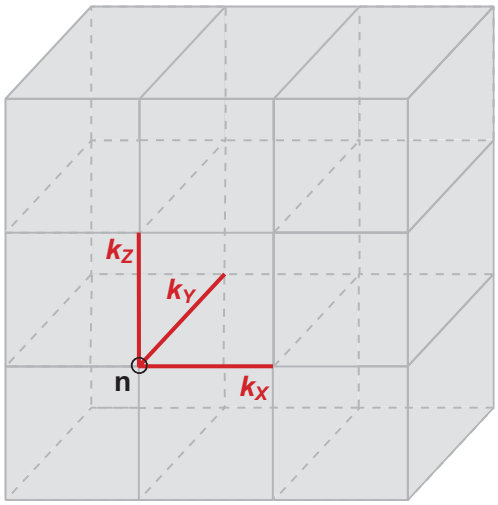

Figure 3-4 *Schematic view of the permeability representation in HYDRASTAR. The permeability is assigned to the red edges in the grid.*

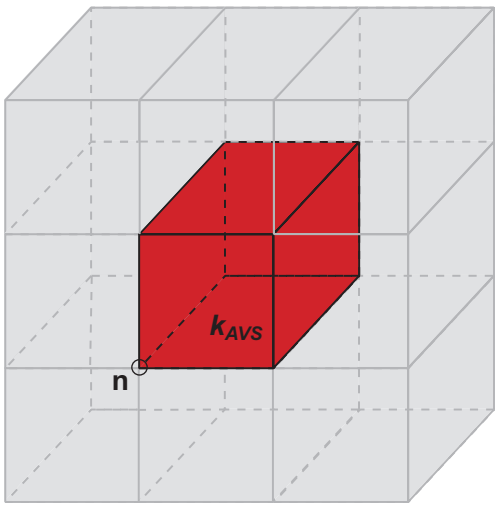

Figure 3-5 *Schematic view of the permeability representation in AVS. The permeability assigned to the element volume is defined by the permeability assigned to the three red edges in Figure 3-4.*

Relating to (*2*) above, since the size of the NAMMU elements was double in the horizontal directions compared to the HYDRASTAR cells a form of upscaling was applied to the HYDRASTAR field. The method considered most appropriate was calculating each value in the permeability field in NAMMU ($K_{i,j,k}$) by averaging the four corresponding values in the HYDRASTAR model (k_1, k_2, k_3 and k_4), see Figure 3-6. The horizontal permeability (K_{xx} and K_{yy}) was calculated using the geometric mean while the vertical permeability (K_{zz}) was calculated using the arithmetic mean. In this way the calculated permeability values were somewhat adjusted for the occurrence of vertical fracture zone elements in the model. An effect of this is that some anisotropy is invoked in the NAMMU model (only in the diagonal components of the permeability tensor, the off diagonal components are zeros) so that near a fracture zone you get a higher vertical permeability. This should be kept in mind when evaluating the results and comparing them to HYDRASTAR results. No averaging was needed in the z direction because the discretisation was not changed between the two models.

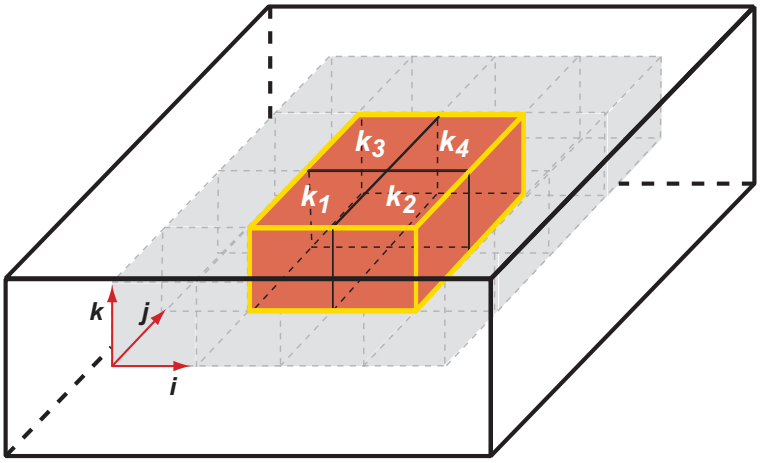

Figure 3-6 *Because the elements in the NAMMU model are a factor two larger in the x and y directions (i, j) compared to the HYDRASTAR model, each element in the NAMMU model (yellow border) corresponds to four cells in the HYDRASTAR model (coloured in red).*

The definitions of the averaging methods used are given below,

$$k_1 = k_{AVS(2i-1,2j-1,k)}$$
$$k_2 = k_{AVS(2i,2j-1,k)}$$
$$k_3 = k_{AVS(2i-1,2j,k)}$$
$$k_4 = k_{AVS(2i,2j,k)}$$

$$K_{xx(i,j,k)} = K_{yy(i,j,k)} = \sqrt[4]{k_1 k_2 k_3 k_4}\,\frac{\mu}{\rho g}$$

$$K_{zz(i,j,k)} = \frac{1}{4}\left(k_1 + k_2 + k_3 + k_4\right)\frac{\mu}{\rho g}$$

where K_{xx}, K_{yy} and K_{zz} are the diagonal components for each permeability tensor $K_{(i,j,k)}$ in the NAMMU model. μ and g are treated as constants.

The permeability field used for the Base Case was also used for the Saline Case.

3.2.2 BaseFine Case

This variant represents a more precise comparison between NAMMU and HYDRASTAR. In this case the permeability field exported from HYDRASTAR is the same as the one that is used in the HYDRASTAR calculations and not the one used for visualisation within the AVS application HYDRAVIZ, where the resultants of the three components are visualised. The representation of the permeability field in HYDRASTAR is shown in Figure 3-4. The discretisation of the model in the BaseFine Case is the same as for the HYDRASTAR model, i.e. cubic elements with a side of 35 m. This means that no averaging of the permeability values is needed and consequently no new discrepancies between the two models are introduced.

The approach used assigning the permeability field to the BaseFine Case resembles the one shown in Figure 3-4 and Figure 3-5 which means that each element in the NAMMU model takes its permeability values from the three corresponding permeability values in the HYDRASTAR model. The difference compared to the representation in AVS (and the other NAMMU variants) is that the permeability tensor, $\underline{\underline{K}}$, in NAMMU is defined by directly assigning the three permeability components (k_X, k_Y and k_Z) from the HYDRASTAR model to the three diagonal elements (K_{xx}, K_{yy} and K_{zz}) of the corresponding permeability tensor in the NAMMU model.

Because of these differences in the numerical discretisation, you would expect some local discrepancies between the two models (NAMMU and HYDRASTAR) and of the order of the variation in velocity over one grid cell.

3.2.3 Anisotropic Case

For the Anisotropic Case, the permeability field used for the Base Case was adjusted for the effects of hydraulic anisotropy in the region. The direction of the major axis was set to N 45 W, which slightly differs from the value, N 48 W, given by *Walker et al. [1997]* but stays within the standard deviation range of ±10° as given by *Walker et al. [1997]*. *Carlsson et al. [1986]* proposed a degree of anisotropy in the permeability of 10:1:1 (*horizontal major:horizontal minor:vertical*) for SFR studies and this is also the ratio used here. Under idealised conditions, the apparent isotropic permeability K_a can be shown to be the geometric mean of the diagonal components of the anisotropic tensor of $\underline{K}$ *[de Marsily, 1981]*,

$$K_a = \sqrt[3]{K_1 K_2 K_3} = \sqrt[3]{10 K_2 K_2 K_2} = \sqrt[3]{10} K_2$$

$$K_1 = 4.64 K_a$$
$$K_2 = 0.464 K_a$$
$$K_3 = 0.464 K_a$$

where K_1 is the permeability in the horizontal major principal direction, K_2 is the permeability in the horizontal minor principal direction and K_3 is permeability in the vertical direction. In this case, K_a is defined as the isotropic value used for the Base Case and the Saline Case,

$$K_a = \sqrt[3]{K_{xx} K_{yy} K_{zz}}$$

$$\{K_{xx} = K_{yy}\}$$

Finally, the components of the tensor are calculated with regards to the orientation of the major axis, as

$$\underline{K} = \begin{pmatrix} K_{xx} & K_{xy} & K_{xz} \\ K_{yx} & K_{yy} & K_{yz} \\ K_{zx} & K_{zy} & K_{zz} \end{pmatrix} =$$

$$= \begin{pmatrix} K_1 \cos^2\alpha + K_2 \sin^2\alpha & (K_1 - K_2)\sin\alpha\cos\alpha & 0 \\ (K_1 - K_2)\sin\alpha\cos\alpha & K_1 \sin^2\alpha + K_2 \cos^2\alpha & 0 \\ 0 & 0 & K_3 \end{pmatrix}$$

where $\alpha = -45°$.

3.2.4 Saline Case

The Saline Case uses the same permeability field as the Base Case, see section 3.2.1.

3.3 Boundary Conditions

The Dirichlet boundary conditions were imported from the regional NAMMU model and interpolated to the site scale model. The Base Case, the BaseFine Case and the Anisotropic Case use the residual pressure solution from the same regional scale model, called *'grlfresh62a.gfs'*. This is a freshwater simulation created exclusively for the HYDRASTAR model since HYDRASTAR can not handle variable-density flow.

The residual pressure boundary conditions used for the Saline Case was imported from a transient NAMMU model including salt, *'grltrans62a.gfs'*. The imported data correspond to the present day situation. In the Saline Case the salt concentration is interpolated to the entire site scale model from the regional NAMMU model. The pressure boundary conditions and the salt concentration inside the model are held constant throughout the simulation. This means that no transient or steady state coupled transport of salt was performed.

The variable solved for in all variants is the residual pressure, P^R. See section 3.5 for definitions of the parameters used.

3.4 Pathlines

A set of 120 particles was released from the northern and the southern blocks (the area of the repository). This is the same number of particles as was released in the HYDRASTAR model and exactly the same starting positions were used. The particles were released at a depth of 604.5 m (z = -604.5 m) which corresponds to the depth of the the centre of the copper canisters used for the encapsulation of spent nuclear fuel. The repository is placed at a depth of 600 m (z = -600 m).

The pathlines show the advective transport of a tracer moving at the pore water velocity. The path, the total travel time (TT) and the canister flux (CF) at the starting position for each of the particles were determined. The results were used for the statistical evaluation for each variant presented later in the report. The numbers and positions of the released particles are shown in Figure 3-7. Note that the figure is not showing the entire model domain.

A constant flowing porosity, ε_f, of $1.0 \cdot 10^{-4}$ was used for the entire model domain in all variants.

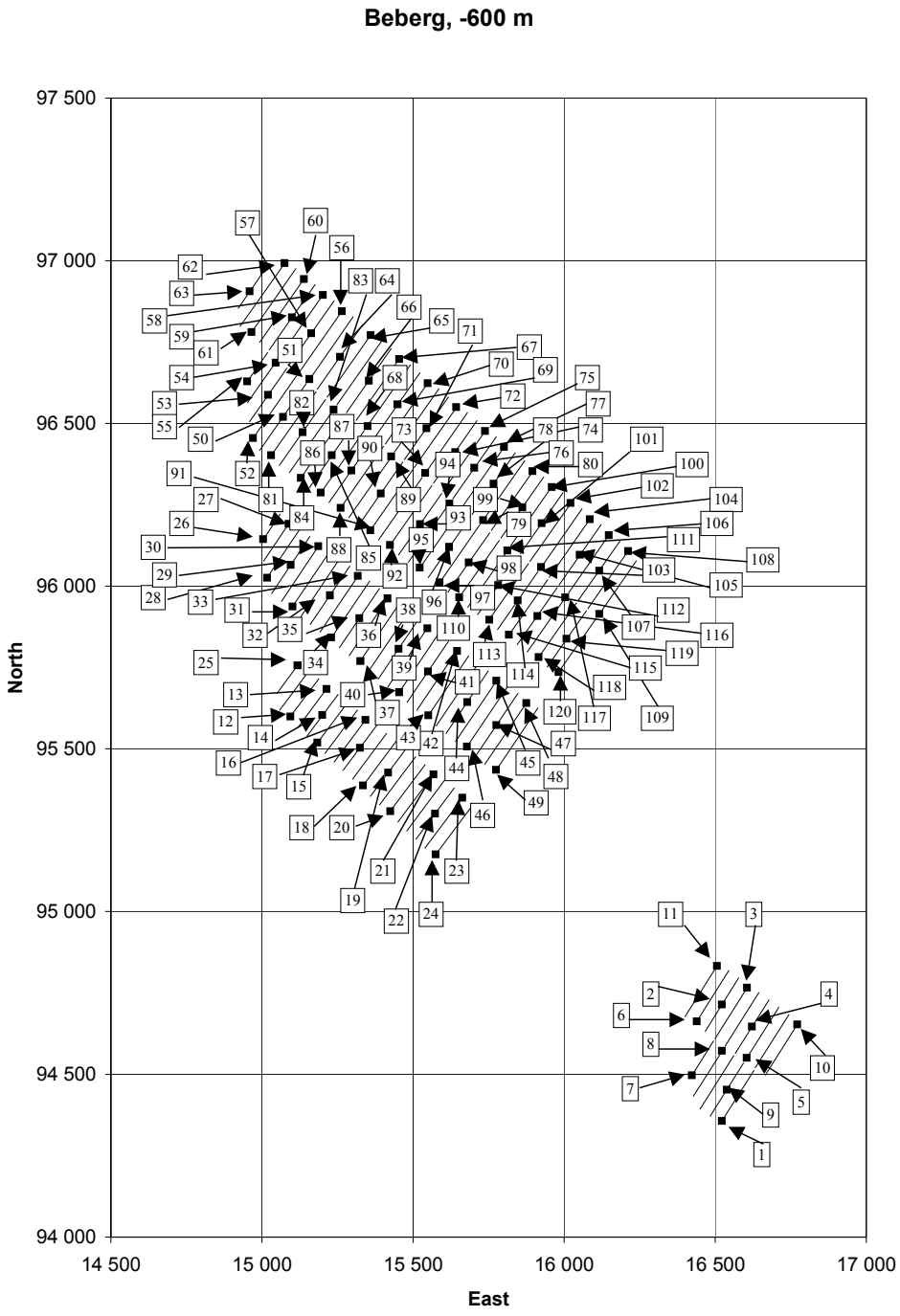

Figure 3-7 *Beberg hypothetical repository tunnel layout at -600 masl with the 120 particle release positions as representative canister positions (Plan view, RAK coordinates with local off-set).*

3.5 Definitions

3.5.1 Pressure

For the standard finite element formulation groundwater flow is modelled in terms of the residual pressure, P^R, using the following equations *[Cliffe et al., 1998]*:

$$\frac{\partial}{\partial t}(\phi\rho)+\nabla(\rho q)=0$$

$$q=-\frac{K}{\mu}\left(\nabla P^R-(\rho-\rho_0)g\right)$$

where ϕ is the flowing rock porosity, q is the Darcy velocity, K is the permeability and μ is the fluid viscosity. Normally the reference fluid density ρ_0 will be taken equal to the fluid density ρ,

$$q=-\frac{K}{\mu}\left(\nabla P^R\right)$$

The residual pressure, P^R, is defined as,

$$P^R = P^T + \rho_0 gz - P^0$$

where P^T is the total pressure, P^0 is the atmospheric pressure and z is the elevation. The z-coordinate is measured vertically upwards from a datum level that equals z = 0.

The hydraulic head, h, is related to the residual pressure by,

$$h=\frac{P^R}{\rho_0 g}$$

3.5.2 Salt Concentration

The salt concentration given by the regional NAMMU model of the Beberg site was interpolated to the site scale model. In the Saline Case the concentration of the saline water was used to determine the density of the saline water. The dependence of density upon the salt variable, C is given by *Cliffe et al. [1998]*,

$$\frac{1}{\rho}=\frac{1-C}{\rho_0}+\frac{C}{\rho_s}$$

The variable C represents a mass fraction of saline water to fresh water. ρ_0 is the freshwater density, ρ_s is the density of the saline water and ρ is the density of the mixed water.

If the density difference is small, i.e.,

$$\left(\frac{(\rho_s - \rho_0)}{\rho_s} \right) << 1$$

then the relationship between the density and the concentration can be approximated by a linear expression,

$$\rho \approx \rho_0 \left(1 + \frac{(\rho_s - \rho_0)}{\rho_s} C \right)$$

For Beberg the values ρ_0 = 998.3 kg/m^3 and ρ_s = 1006.29 kg/m^3 are used. Hence, the density can be expressed in terms of a linear relationship to the mass fraction C,

$$\rho = 998.3(1 + 0.008C)$$

This gives that a salt concentration of C = 1.0 corresponds to a salinity of 0.8 % or a water density of 1006.29 kg/m^3.

3.5.3 Boundary Flow

The boundary flow across the model surfaces was calculated with NAMMU that uses an approximate integration algorithm to determine the mass balance over a specified plane in the model. This can cause errors when calculating the overall mass balance. In addition to this, the boundary flows were calculated on the surfaces of a smaller box defined inside the model domain. The box was moved 5 m away in all directions from the model domain giving a box that was 10 m shorter in all three directions. The reason for this is that the algorithm may have difficulties integrating on surfaces that are too close to the model boundaries and therefore present strange results.

In a finite element model, by definition, the mass is conserved over the whole model domain. This means that if the boundary flows were calculated properly using the Gaussian quadrature method, the mass balance would be found to be within the range of the numerical errors, i.e. approximately 10^{-8}.

Since the groundwater flow is calculated as a net value it does not describe the complex pattern of in- and outflow through the boundaries. This is particularly the case on the top surface where there are large differences between areas with large recharge (the southwest of the model domain) and some areas with a large discharge (the northeast of the model domain). Therefore the net flow might be somewhat misleading trying to describe the actual groundwater flow situation.

3.5.4 Statistical Measures

The statistical summaries in the report are based on the results from the 120 released particles in each variant. The statistical calculations are presented using relative frequency histograms and floating histogram. The relative frequency histogram is a bar chart with a bar width determined by default algorithms in Statistica so that 30 bars are fitted inside the data range. Since the data range varies between the different variants, the bar width will also vary.

An alternative method of constructing a frequency distribution histogram is to use a floating histogram. Floating histograms are single curved line representations of the frequency of the data. Although floating histograms are smoothed representations of the data, they are more legible when superimposed for the comparison of multiple histograms.

Statistica calculates smoothed histograms using a moving window as a filter passing over the ordered sequence of the data. For each data value centred in the window, the frequency is calculated as the fraction of the data falling within the window. The width of the window in Statistica is set to ±½ an order of magnitude around the data value in the centre of the window.

3.6 Figures

Some of the figures in this report are shown in a special view that needs some explanation. The view consists of the six separate surfaces of the model domain and it is put together by opening the model in the way shown in Figure 3-8. Hence, the final view is showing the model surfaces as they look from the outside of the model. This view is used to visualise the boundary conditions and the permeability fields.

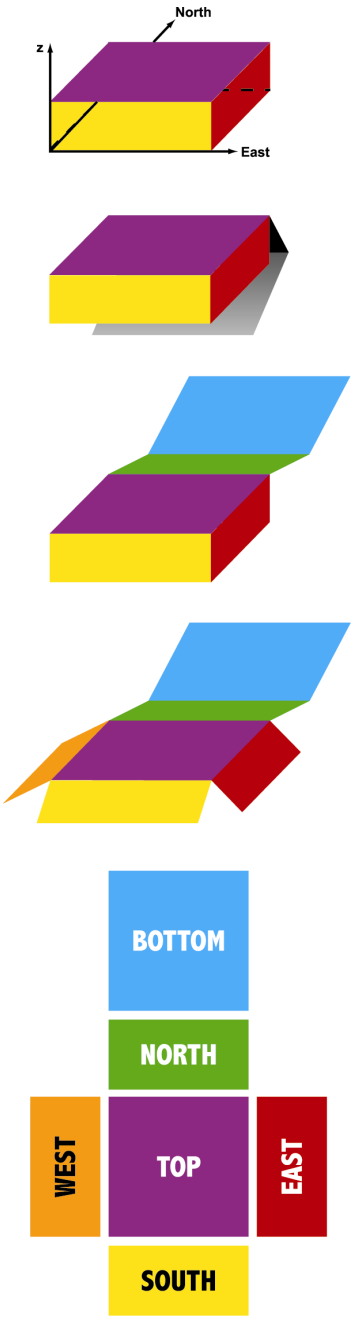

Figure 3-8 *Description of the transformation of the model domain from the oblique view to the plan view.*

3.7 Variants

Table 3-1 summarises the input for the variants performed. A more extensive summary is given in Table A - 10.

Table 3-1 Summary of input data used for all variants.

	Base Case	BaseFine Case	Anisotropic Case	Saline Case
HYDRASTAR Permeability field obtained from	HYDRASTAR Variant 4, Permeability resultant	HYDRASTAR Variant 4, Permeability components	HYDRASTAR Variant 4, Regional Anisotropy (N 45 W)	HYDRASTAR Variant 4, Permeability resultant
Corresponding HYDRASTAR variant	Variant 4	Variant 4	-	Variant 1

4 Base Case

The Base Case represents the expected site conditions that formed the base for the HYDRASTAR models. In the nested modelling approach used here with NAMMU the boundary conditions are interpolated from the much larger regional NAMMU model for Beberg. This model was set up by *Hartley et al. [1998]* and is a modification of the AltK variant. The model was rerun without salt and the steady state freshwater residual pressure values from this simulation were used calculating the boundary conditions for the local scale model.

4.1 Boundary Conditions

Figure 4-1 shows the constant residual pressure (Dirichlet) boundary conditions on each face of the model domain for the Base Case. The red colour indicates higher pressure and the blue colour indicates lower pressure. The northeast direction of the major hydraulic gradient in the region is apparent.

The boundary conditions used in the Base Case were also used for the BaseFine Case and the Anisotropic Case.

4.2 Permeability Field

Figure 4-2 - Figure 4-5 visualise the $\log_{10}$ of the horizontal and the vertical permeability field used for the Base Case. The field is based on permeability values imported from Variant 4 in HYDRASTAR, see section 3.2.1 for details. The red colour indicates higher permeability and the blue colour indicates lower permeability. The effects of different averaging methods used are clearly visible when comparing Figure 4-2 with Figure 4-3. The geometric mean used for calculating the horizontal permeability gives a slightly lower value than the arithmetic mean used for the vertical permeability. In this way the calculated permeability value is somewhat adjusted for the occurrence of fracture zone elements in the model. The highly permeable top layer appears in a lighter colour in all the figures and so do the two repository areas. Another interesting feature is the highly permeable Zone 2 situated directly above the northern repository. Both the horizontal and the vertical permeability range from $1.3 \cdot 10^{-15}$ m^2 to $1.3 \cdot 10^{-11}$ m^2.

The permeability field used in the Base Case was also used for the Saline Case.

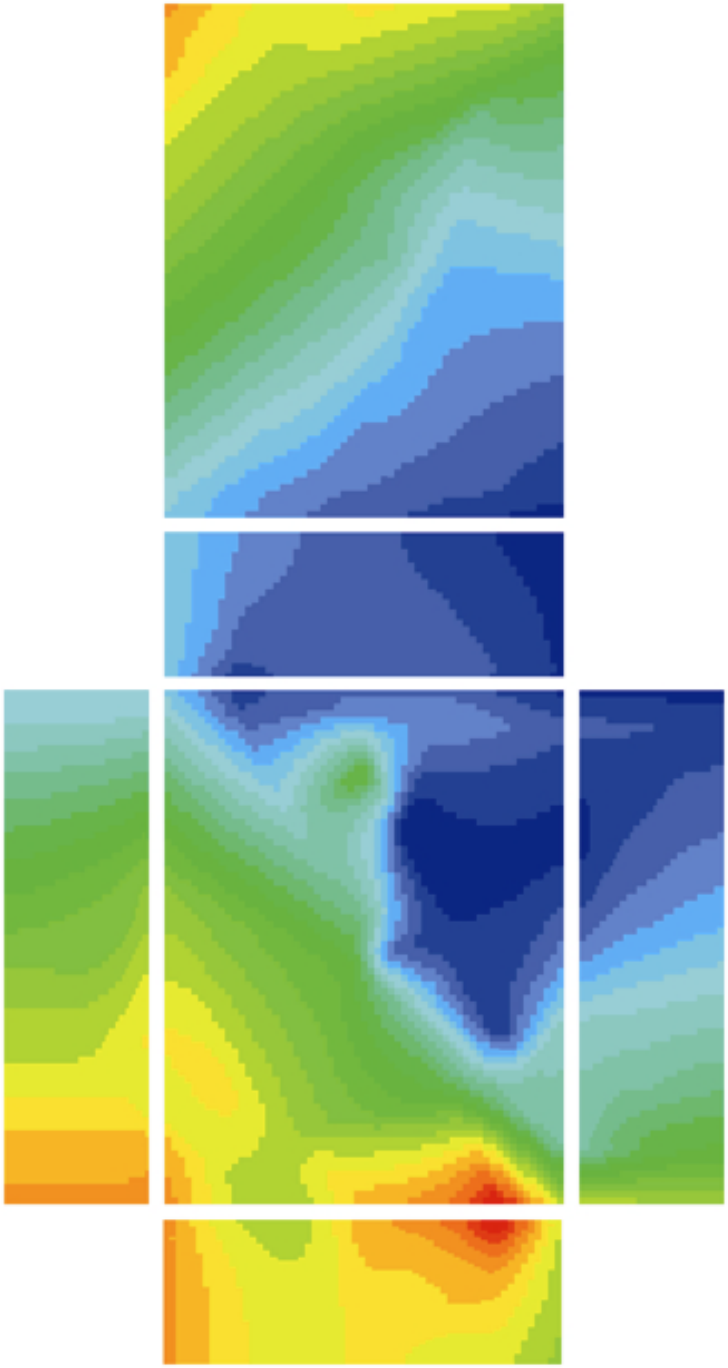

Figure 4-1 *The constant residual pressure (Dirichlet) boundary conditions on each face of the model domain for the Base Case. The red colour indicates higher pressure and the blue colour indicates lower pressure.*

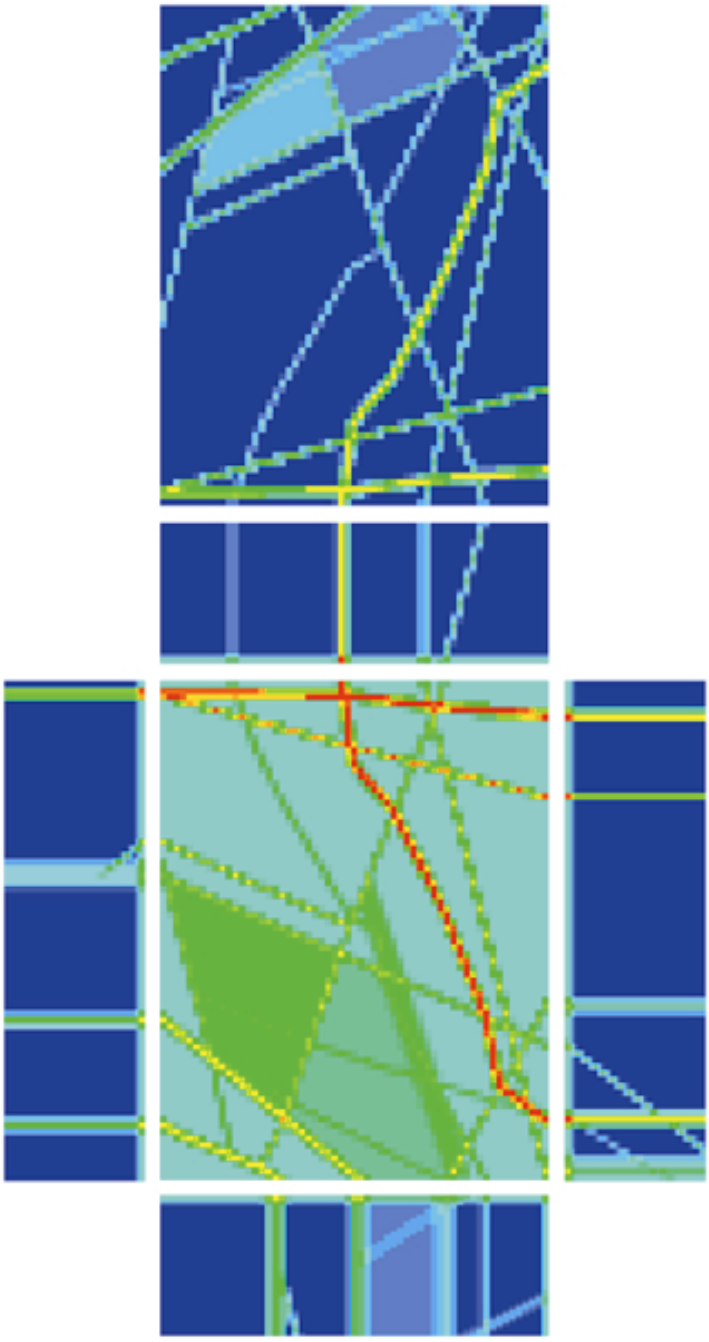

Figure 4-2 *The $\log_{10}$ of the horizontal permeability field on each face of the model domain for the Base Case. The red colour indicates higher permeability and the blue colour indicates lower permeability.*

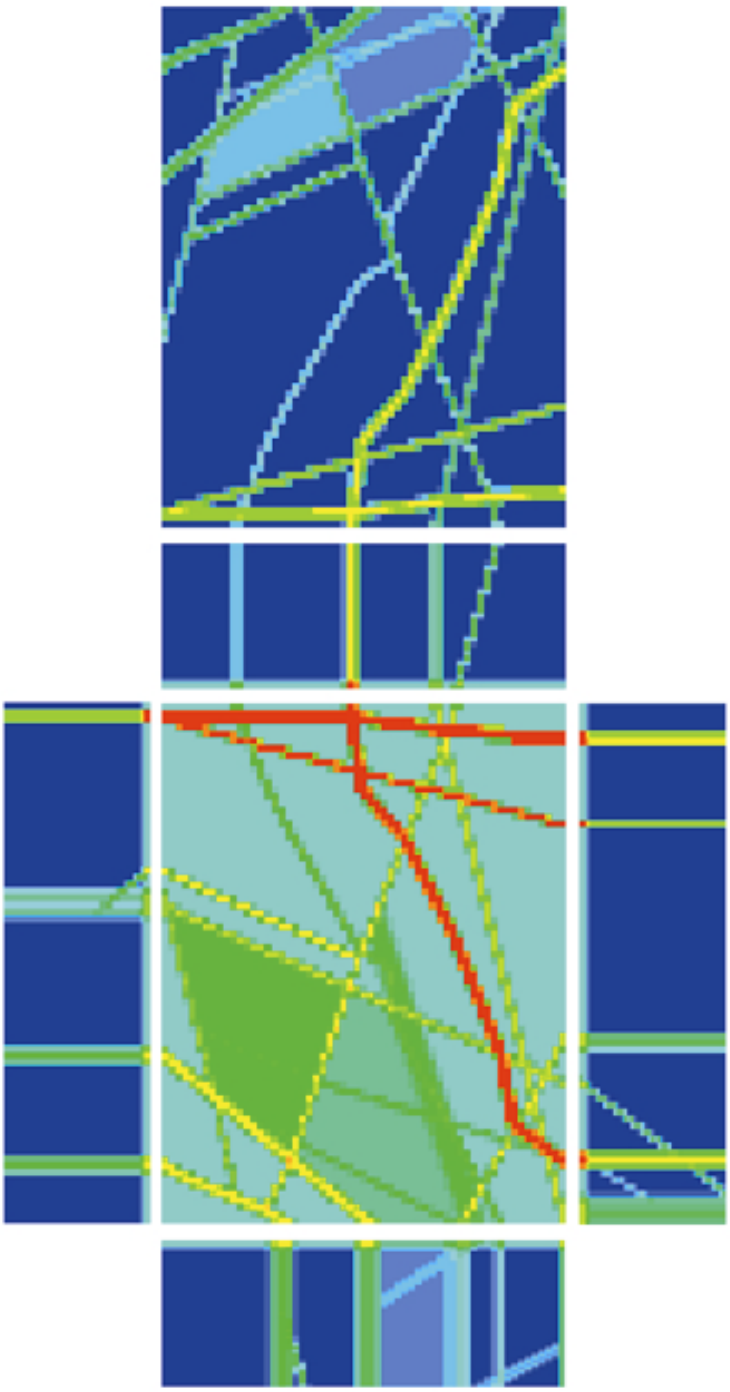

Figure 4-3 *The $\log_{10}$ of the vertical permeability field on each face of the model domain for the Base Case. The red colour indicates higher permeability and the blue colour indicates lower permeability.*

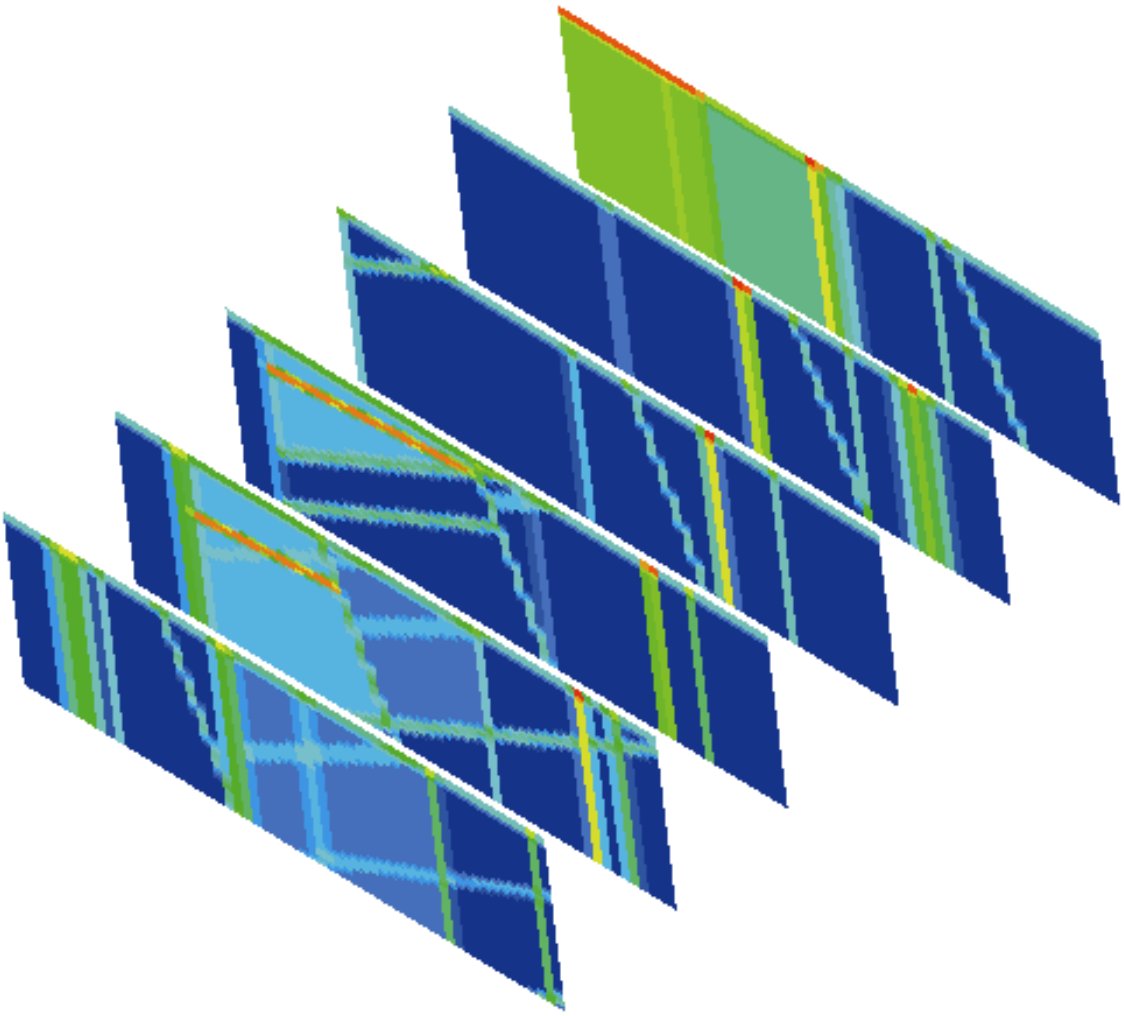

Figure 4-4 *The $\log_{10}$ of the horizontal permeability field distribution shown on six slices cutting through the model domain in the west-east direction for the Base Case. The red colour indicates higher permeability and the blue colour indicates lower permeability. View from the southeast.*

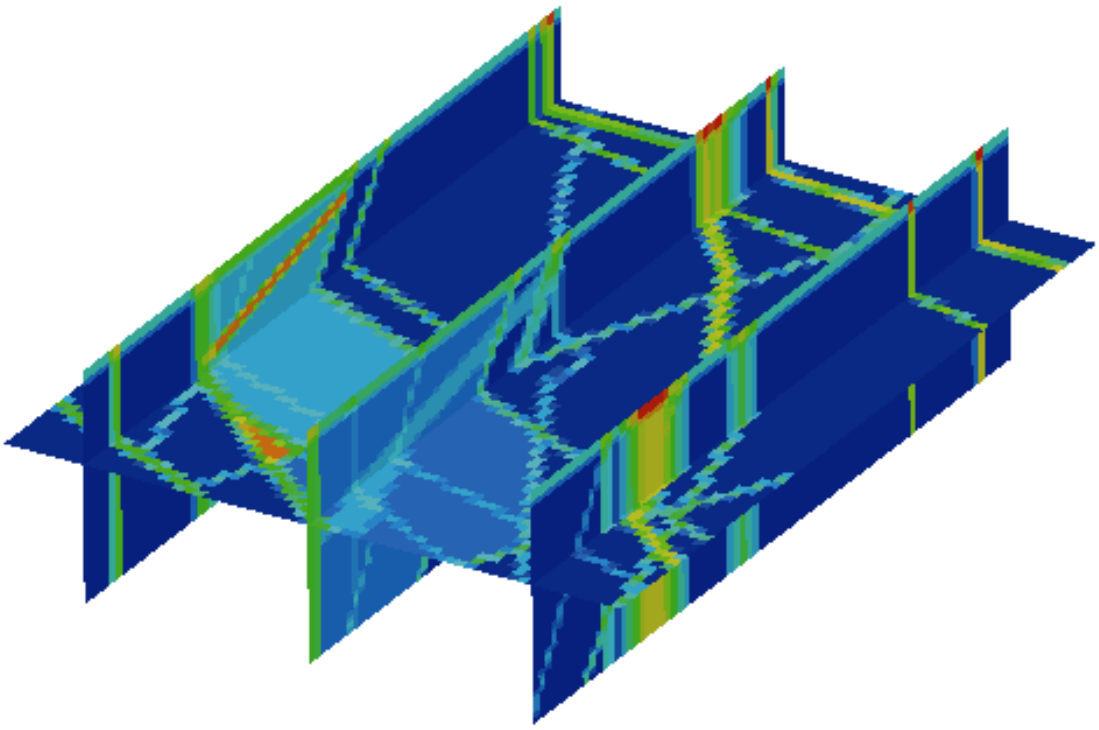

Figure 4-5 *The $\log_{10}$ of the horizontal permeability field shown on four slices cutting through the model domain in the south-north direction for the Base Case. The horizontal plane is placed at a depth of z = -604.5 m. The red colour indicates higher permeability and the blue colour indicates lower permeability. View from the southeast.*

4.3 Results

Figure 4-6 and Figure 4-7 show the calculated residual pressure distribution on slices cutting through the model domain for the Base Case. The view of the model is taken from the southeast for both figures. The hydraulic head range from 16.6 m to 33.4 m. The residual pressure can be thought of as a driving pressure in the model, see section 3.5.1 for the definition. The red colour indicates higher pressure and the blue colour indicates lower pressure. The northeast direction of the major hydraulic gradient in the region is apparent. Around the northern repository some impact of the fracture zones on the pressure distribution can be seen as a decreased residual pressure caused by the conductive Zone 2, see Figure 4-6.

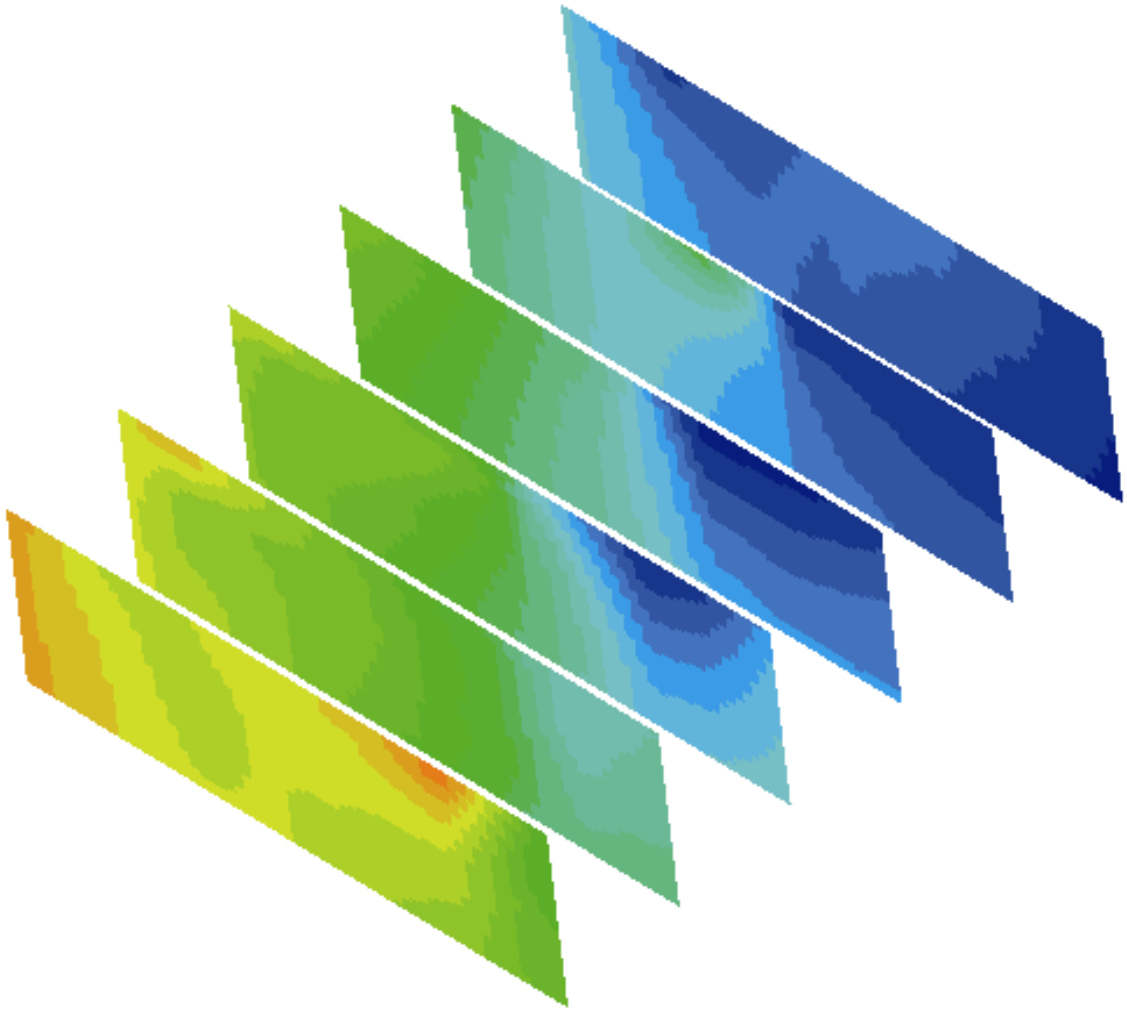

Figure 4-6 *The residual pressure distribution shown on six slices cutting through the model domain in the west-east direction for the Base Case. The red colour indicates higher pressure and the blue colour indicates lower pressure. View from the southeast.*

In Figure 4-7 the effects of the Imundbo Zone appears in the residual pressure distribution where the pressure contours are aligned with the zone. Apart from the discussed effects the impact of the fracture zones on the pressure distribution is difficult to see.

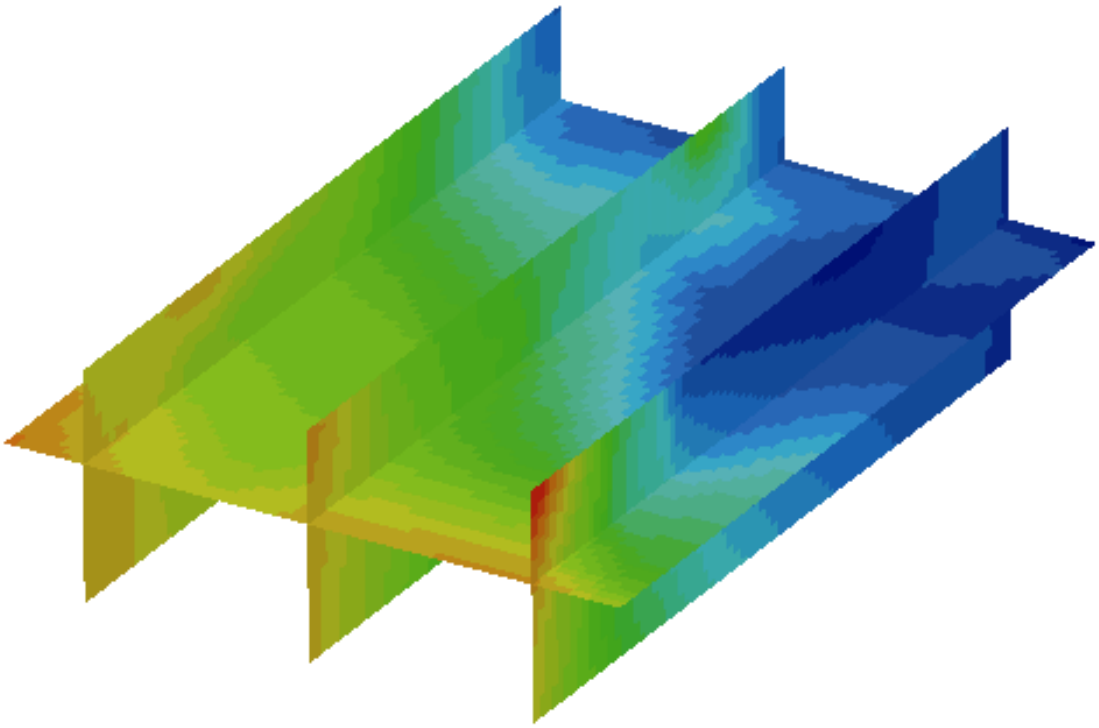

Figure 4-7 *The residual pressure distribution shown on four slices cutting through the model domain in the south-north direction for the Base Case. The horizontal plane is placed at a depth of z = -604.5 m. The red colour indicates higher pressure and the blue colour indicates lower pressure. View from the southeast.*

4.3.1 Exit Locations

A set of 120 particles were released at a depth of z = -604.5 m from the northern and southern blocks (the area of the repository), 109 from the northern block and 11 from the southern block. Figure 4-8 shows the pathlines in three views calculated with NAMMU. The pathlines are coloured with respect to travel time. The exit locations, shown in Figure 4-9, are defined as the points where the released particles reach the boundary in the model domain. The pathlines are predominantly directed to the northeast through the rock mass away from the repository. This is also corresponding to the regional flow pattern. The discharge areas are found around the regional fracture zones situated northeast of the repository. The major part of the released particles exits within the Imundbo Zone. This is also where we find the pathlines with the longest travel times. A couple of these paths tend to follow Zone 1 until they reach the intersection with the Imundbo Zone where they discharge.

A smaller group of pathlines exits within Zone 3 and another group exits within Zone 4. Both of these groups follow the permeable Zone 2 upward in a northeast direction until they reach the discharge areas in Zone 3 and 4. The pathlines following Zone 2 have the shortest travel times (less than 10 years up to the top of the model) among the released particles.

All the particles released from the southern repository follow the same path, at the beginning horizontally through the rock mass until they reach the Imundbo Zone where they exit vertically. These pathlines clearly demonstrate the influence of the fracture zones. A few particles exit through the bottom of the model. Some of these particles follow the Imundbo Zone far up north while another group exit not very far northeast of the northern repository where they were released.

The exit locations and travel times are comparable to those of the regional steady state freshwater model used to determine the boundary conditions for this study. Some of the pathlines tend to go a bit deeper in this site scale model compared to the ones in the regional model. The reason for that might be the higher vertical permeability, which is the result from the averaging method used here when applying the permeability field from HYDRASTAR.

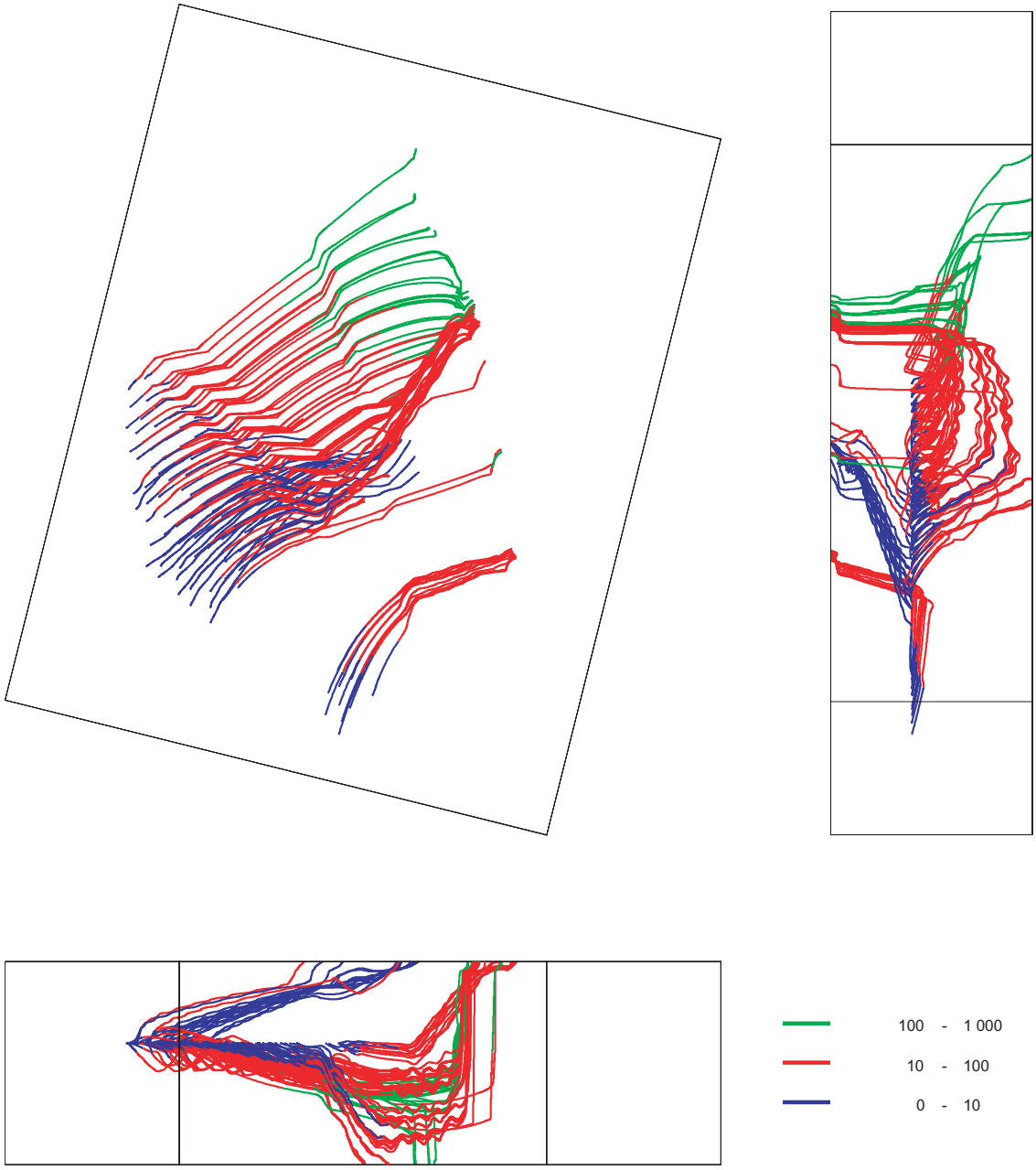

Figure 4-8 *Forward pathlines for the Base Case. A set of 120 particles are released at a depth of z = -604.5 m, 109 from the northern block and 11 from the southern block. The pathlines are coloured with respect to travel time given in years. Upper left: Plan view of the model from above. Upper right: Elevation view from the east. Lower left: Elevation view from the south.*

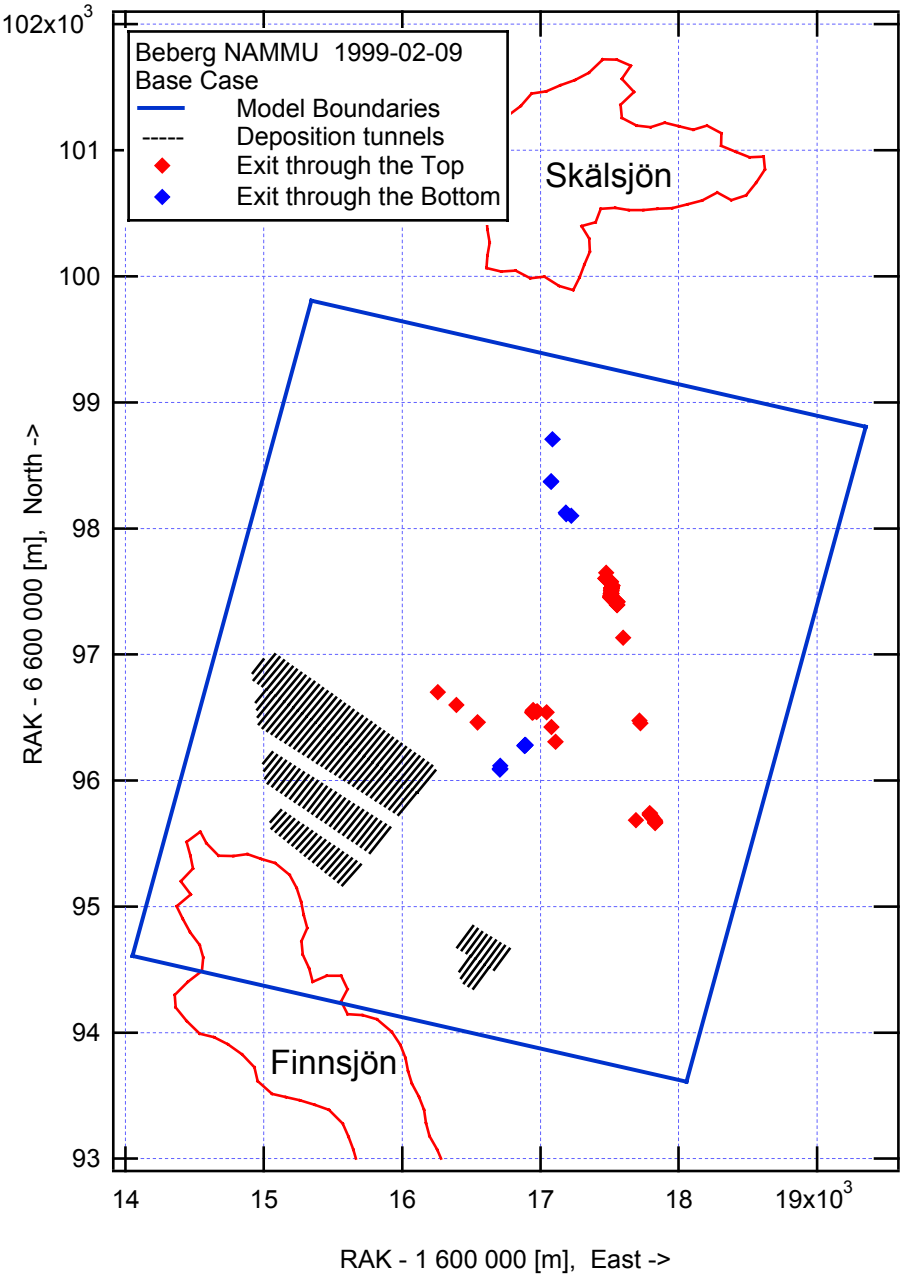

Figure 4-9 *Exit locations for the released particles in the Base Case. The red markers show particles exiting the top of the model and the blue markers show particles exiting the bottom of the model. View from the top of the model.*

4.3.2 Boundary Flow

Figure 4-10 shows the boundary flows for the Base Case. The direction of the arrows denotes the direction of the net flow over the model surface. The size of the arrows has been altered to symbolise the magnitude of the flow. The actual size should only be regarded as an illustration and not as an exact measure. The direction of the boundary flows is in agreement with the regional flow pattern.

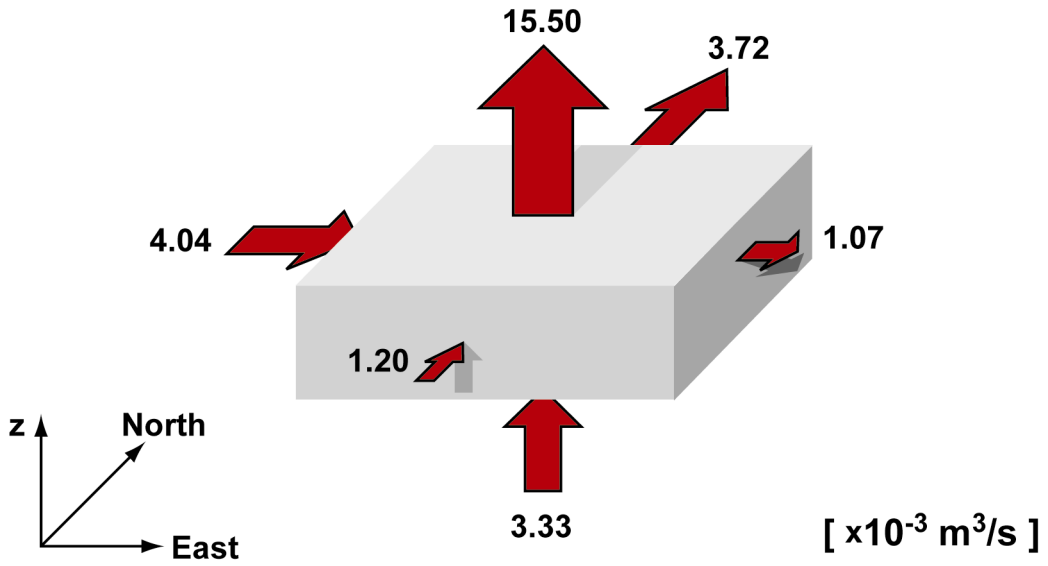

Figure 4-10 *Boundary flows for the Base Case. Arrows show the direction of the calculated net flow through each of the boundary surfaces.*

Table 4-1 summarises the calculated groundwater boundary flows for the Base Case. A positive boundary flow is directed out from the model domain. Although the directions of the flow coincide with the regional flow pattern, i.e. in the northeast direction, the calculated mass balance shows a large discrepancy. Looking at the net flows, the outflow from the model is more than a factor two larger than the inflow to the model. Studying the gross flows for each surface of the model gives us an explanation to the discrepancy in the mass balance. In fact, the total residual from the mass balance is only about 10 % of the gross flows through the top boundary surface, which is also the predominating outflow area. See section 3.5.3 for an explanation of the boundary flow calculations.

Table 4-1 Groundwater flow through the model boundaries for the Base Case. Positive flow is directed out from the model.

Site Model Surface	Gross Inflow $[\cdot 10^{-3}\ m^3/s]$	Gross Outflow $[\cdot 10^{-3}\ m^3/s]$	Net Flow through Surface $[\cdot 10^{-3}\ m^3/s]$
Top	-75.00	90.50	15.50
Bottom	-6.25	2.92	-3.33
South	-1.23	0.04	-1.20
North	0.00	3.72	3.72
West	-4.11	0.07	-4.04
East	-1.69	2.76	1.07
Total Inflow	-88.28	-	-8.57
Total Outflow	-	100.00	20.29
Mass balance			***11.72***

4.4 Statistics

Table 4-2 shows the statistical summary of the 120 canister positions in the Base Case. The calculated performance measures are the travel time (TT) and the canister flux (CF). The travel time is the time used by the particles released in the model to be transported by advection from the starting position to any boundary of the model domain. The canister flux is the Darcy groundwater velocity calculated by NAMMU as the resultant of the three velocity components (u_x, u_y and u_z) at each of the 120 particle starting positions.

All particles are released at a depth of -604.5 m. For the statistical calculations the particles were also grouped with respect to what boundary they exited through.

Table 4-2 Statistical summary for the Base Case.

Statistics	$Log_{10}(TT_{tot})$	$Log_{10}(TT_{top})$	$Log_{10}(TT_{bottom})$	$Log_{10}(CF)$
Mean	1.657	1.646	1.724	-2.712
Median	1.701	1.751	1.559	-2.754
5th Percentile	0.677	0.667	1.185	-2.944
25th Percentile	1.396	1.396	1.360	-2.855
75th Percentile	2.017	2.009	2.230	-2.587
95th Percentile	2.286	2.248	2.354	-2.384
St Deviation	0.470	0.476	0.439	0.189
Variance	0.221	0.227	0.193	0.036
Min Value	0.044	0.044	1.185	-3.029
Max Value	2.353	2.305	2.353	-1.937
Fraction	1.000	0.858	0.142	1.000

4.4.1 Travel Time

Table 4-2 summarises the result for the travel time and indicates a median travel time of 56 years, with an interquartile range from 25 years to 102 years for the particles exiting the top of the model. The variance of the $\log_{10}$(TT) for the particles exiting through the top is 0.227. The 5^{th} percentile is less than 5 years which tells us that a few particles reach the top boundary very quickly. These particles are all released from within the northern repository. 85.8 % of the released particles are exiting through the top of the model, the rest of the particles exit through the bottom of model. No particles were stuck in the model for the Base Case. Figure 4-11 presents the relative frequency histogram of $\log_{10}$ travel time for 120 starting positions. The histogram is normalised with respect to the total number of starting positions. The lower tail in the histogram (<10 years) represents the fast particles released from within the northern repository following Zone 2 up to the top of the model.

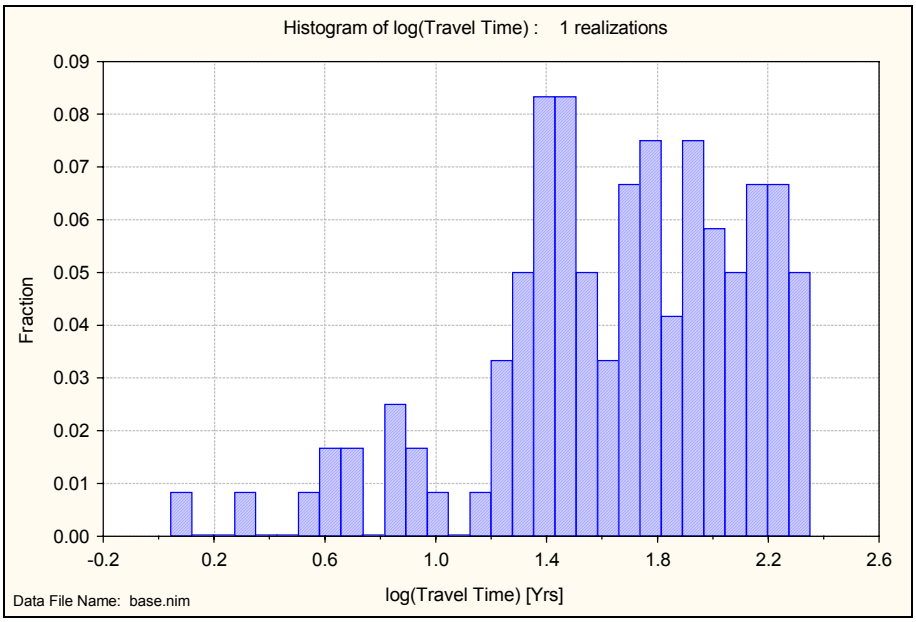

Figure 4-11 *Relative frequency histogram of $\log_{10}$ travel time for the Base Case. The histogram is normalised with respect to the total number of starting positions. Results for 120 starting positions.*

Figure 4-12 presents the floating histogram of $\log_{10}$ travel time for 120 starting positions. The histogram is normalised with respect to the total number of starting positions and it is slightly skewed with a larger lower tail.

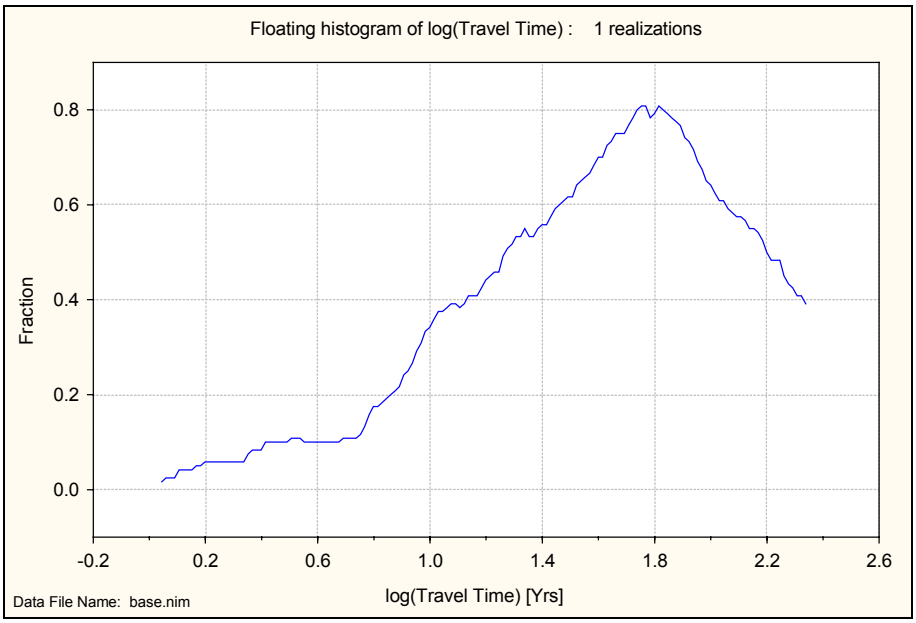

Figure 4-12 *Floating histogram of $\log_{10}$ travel time for the Base Case. The histogram is normalised with respect to the total number of starting positions. Results for 120 starting positions.*

Figure 4-13 presents a box plot of $\log_{10}$ travel time for 120 starting positions.

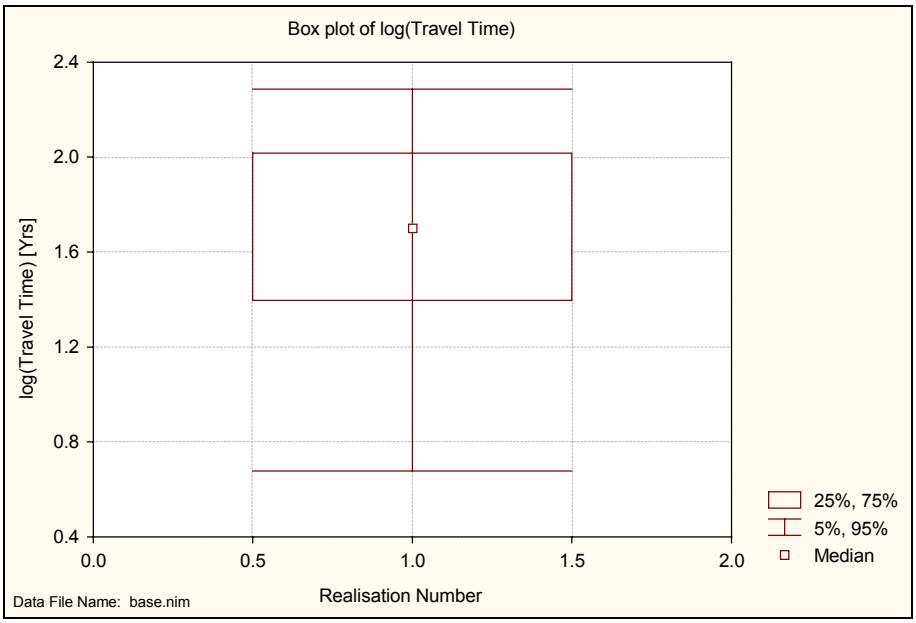

Figure 4-13 *Box plot of $\log_{10}$ travel time showing the median and the 5th, 25th, 75th and 95th percentiles for the Base Case. Results for 120 starting positions.*

4.4.2 Canister Flux

Table 4-2 summarises the result for the canister flux and indicates a median canister flux of $1.8 \cdot 10^{-3}$ m/year, with an interquartile range from $1.4 \cdot 10^{-3}$ m/year to $4.1 \cdot 10^{-3}$ m/year. When calculating the canister flux the particles are not divided into subgroups since the canister flux is measured at the starting position and therefore independent of exit location. The variance of the $\log_{10}$(CF) for all particles is 0.036. Figure 4-14 presents the relative frequency histogram of $\log_{10}$ canister flux for 120 starting positions. The histogram is normalised with respect to the total number of starting positions and is slightly skewed with a larger upper tail, this can also been seen in Figure 4-15.

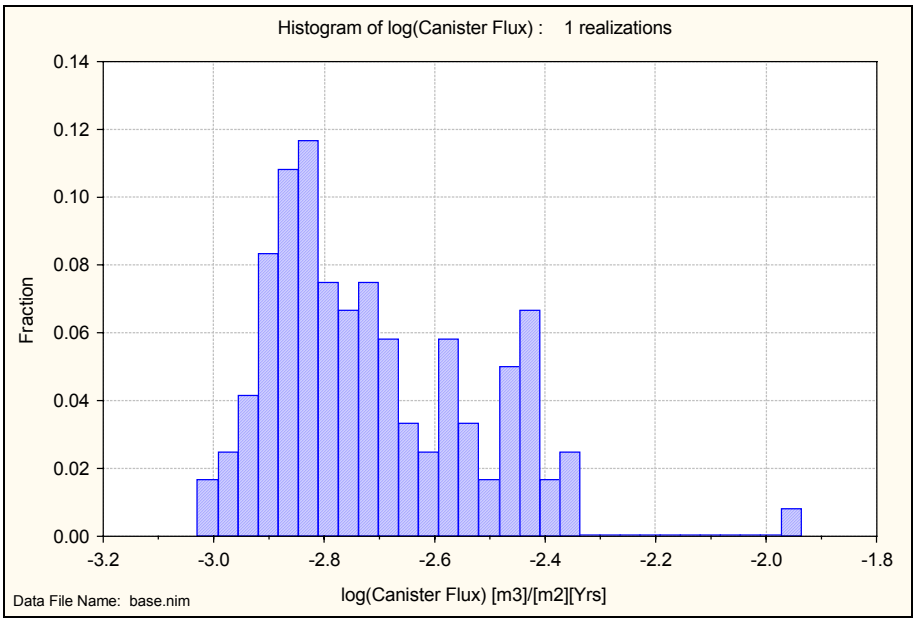

Figure 4-14 *Relative frequency histogram of log_{10} canister flux for the Base Case. The histogram is normalised with respect to the total number of starting positions. Results for 120 starting positions.*

Figure 4-15 presents the floating histogram of log_{10} canister flux for 120 starting positions. The histogram is normalised with respect to the total number of starting positions.

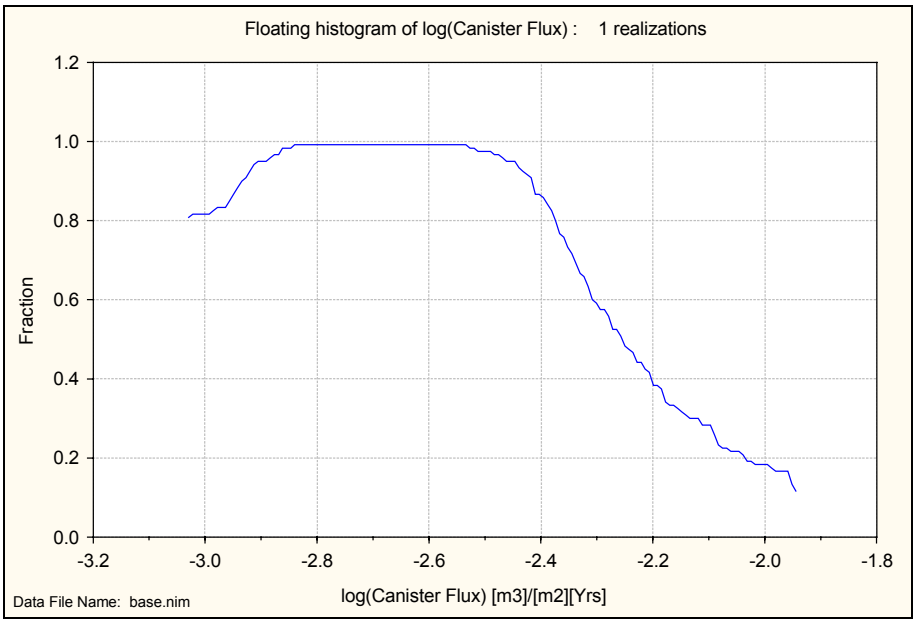

Figure 4-15 *Floating histogram of log_{10} canister flux for the Base Case. The histogram is normalised with respect to the total number of starting positions. Results for 120 starting positions.*

Figure 4-16 presents a box plot of $\log_{10}$ canister flux for the single realisation with 120 starting positions.

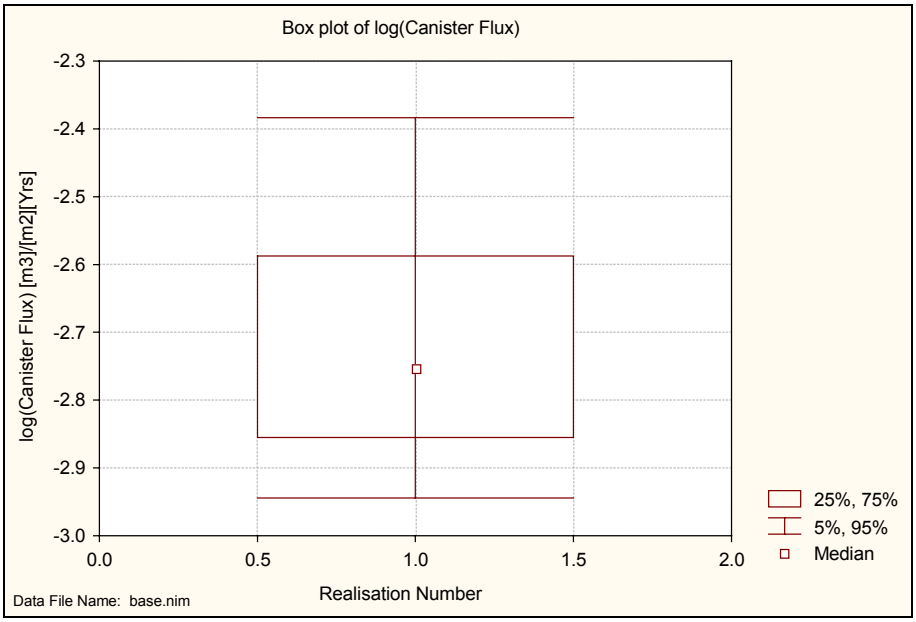

Figure 4-16 *Box plot of $\log_{10}$ canister flux showing the median and the 5th, 25th, 75th and 95th percentiles for the Base Case. Results for 120 starting positions.*

Figure 4-17 presents a scatter plot of $\log_{10}$ travel time versus $\log_{10}$ canister flux. Although only one realisation has been run, it confirms that the $\log_{10}$ travel time is inversely correlated to the $\log_{10}$ canister flux.

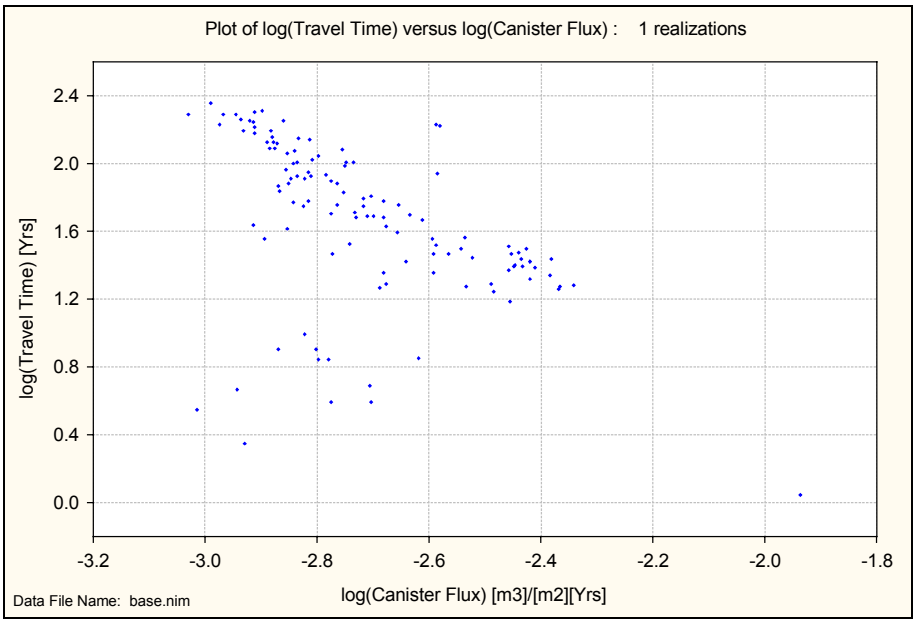

Figure 4-17 Scatter plot of $\log_{10}$ travel time versus $\log_{10}$ canister flux for the Base Case. Results for 120 starting positions.

5 BaseFine Case

The BaseFine Case (and the Base Case) represents the expected site conditions that formed the base for the HYDRASTAR models. The main differences between the Base Case and BaseFine Case is that the latter uses the same discretisation as the HYDRASTAR model which makes it possible to use a more correct permeability representation.

In the nested modelling approach used here with NAMMU the boundary conditions are interpolated from the much larger regional NAMMU model for Beberg. This model was set up by *Hartley et al. [1998]* and is a modification of the case AltK. The model was rerun without salt and the steady state freshwater head values from this simulation were used calculating the boundary conditions for the site scale model.

5.1 Boundary Conditions

Figure 5-1 shows the constant residual pressure (Dirichlet) boundary conditions on each face of the model domain for the BaseFine Case. The red colour indicates higher pressure and the blue colour indicates lower pressure. The pressure values *(Pa)* are given in the legend. The northeast direction of the major hydraulic gradient in the region is apparent. The BaseFine Case uses the same boundary conditions as the Base Case, see sections 3.3 and 4.1 for details and comparison. The finer discretisation in the BaseFine Case compared to the Base Case is apparent when comparing Figure 4-1 and Figure 5-1.

5.2 Permeability Field

Figure 5-2 - Figure 5-4 visualise the $\log_{10}$ of the permeability field (the K_{xx} component of the permeability tensor) used for the BaseFine Case. The red colour indicates higher permeability and the blue colour indicates lower permeability. The highly permeable top layer appears in a lighter colour in all the figures and so do the two repository areas. Another interesting feature is the highly permeable Zone 2 situated directly above the northern repository. The permeability range from $1.3 \cdot 10^{-15}$ m^2 to $1.3 \cdot 10^{-11}$ m^2.

The permeability field used for the BaseFine Case is described in section 3.2.2.

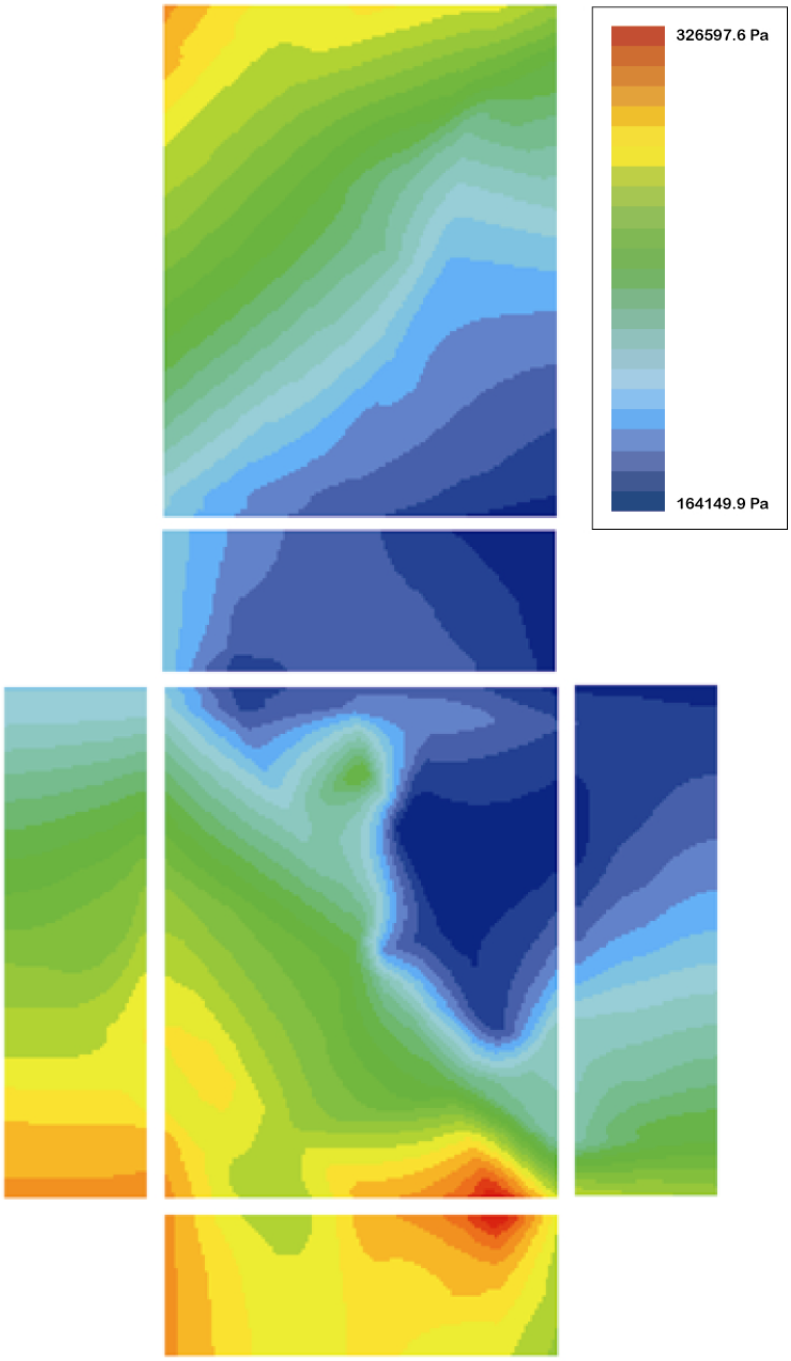

Figure 5-1 *The constant residual pressure (Dirichlet) boundary conditions on each face of the model domain for the BaseFine Case. The red colour indicates higher pressure and the blue colour indicates lower pressure. The pressure values (Pa) are given in the legend.*

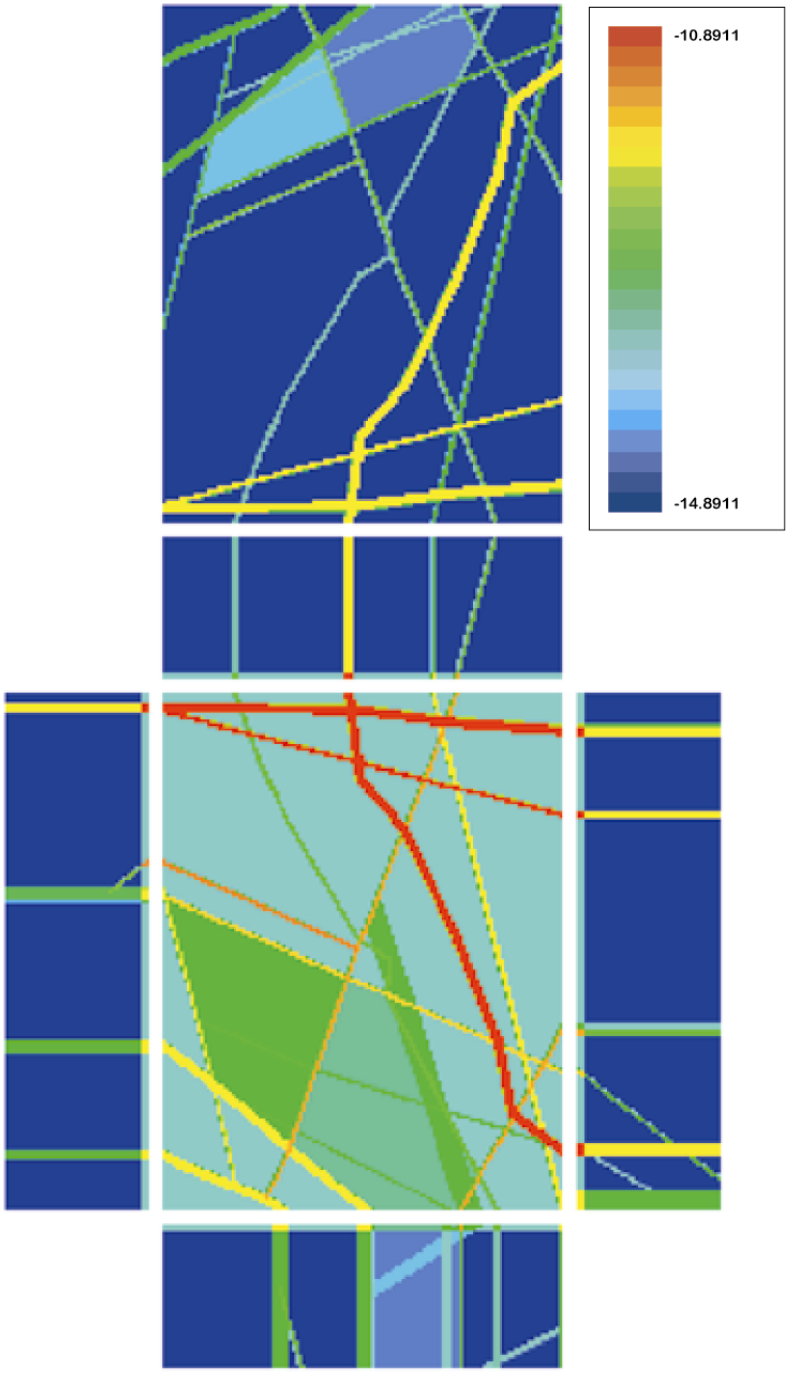

Figure 5-2 *The $\log_{10}$ of the permeability field (the K_{xx} component of the permeability tensor) on each face of the model domain for the BaseFine Case. The red colour indicates higher permeability and the blue colour indicates lower permeability. The $\log_{10}$ of the permeability values are given in the legend.*

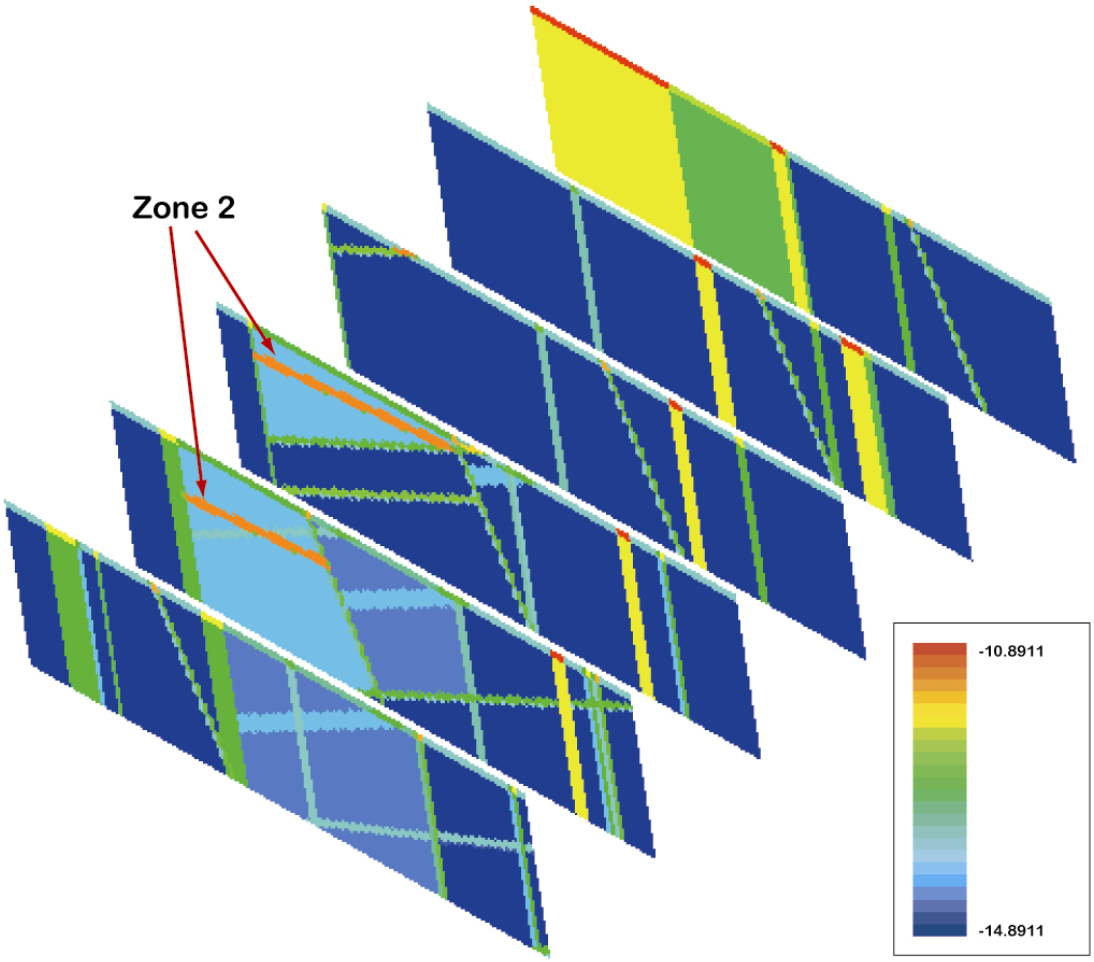

Figure 5-3 *The $\log_{10}$ of the permeability field (the K_{xx} component of the permeability tensor) distribution shown on six slices cutting through the model domain in the west-east direction for the BaseFine Case. The red colour indicates higher permeability and the blue colour indicates lower permeability. The $\log_{10}$ of the permeability values are given in the legend. View from the southeast.*

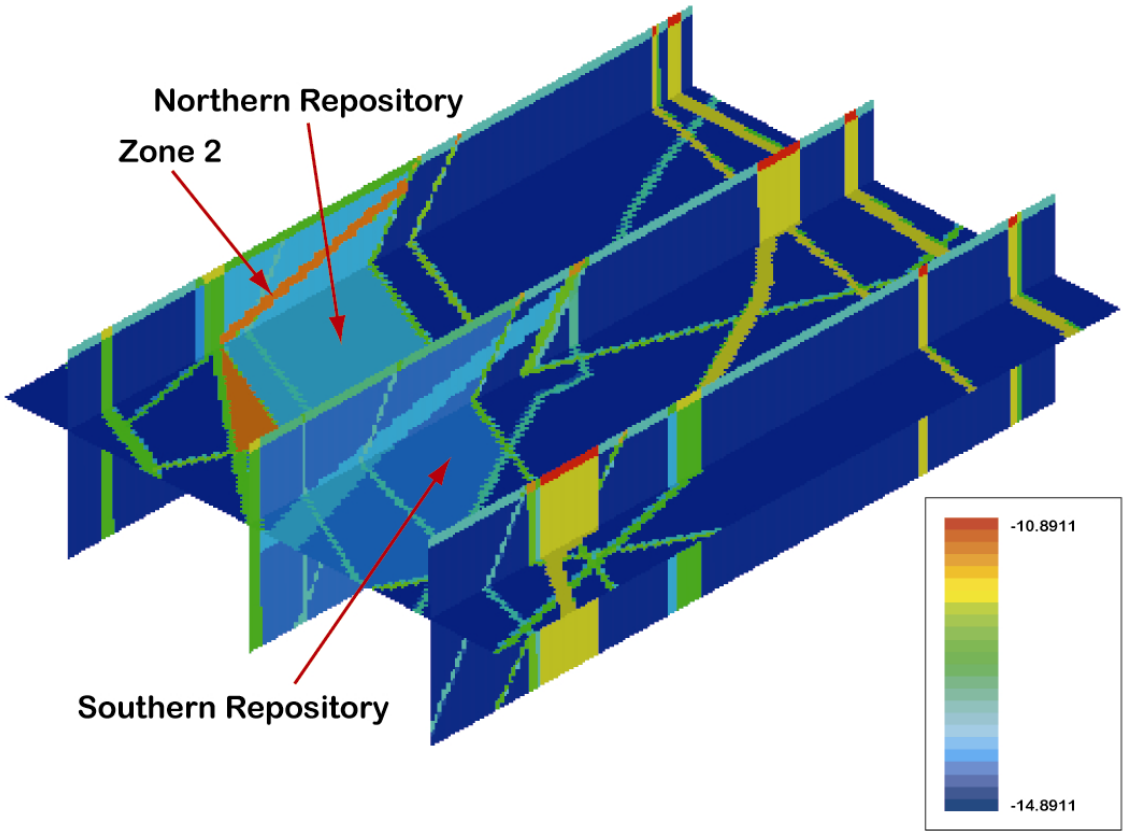

Figure 5-4 *The log_{10} of the permeability field (the K_{xx} component of the permeability tensor) shown on four slices cutting through the model domain in the south-north direction for the BaseFine Case. The horizontal plane is placed at a depth of z = -604.5 m. The red colour indicates higher permeability and the blue colour indicates lower permeability. The log_{10} of the permeability values are given in the legend. View from the southeast.*

5.3 Results

Figure 5-5 and Figure 5-6 show the calculated residual pressure distribution on slices cutting through the model domain for the BaseFine Case. The view of the model is taken from the southeast for both figures. The hydraulic head range from 16.8 m to 33.3 m. The residual pressure can be thought of as a driving pressure in the model, see section 3.5.1 for the definition. The red colour indicates higher pressure and the blue colour indicates lower pressure. The northeast direction of the major hydraulic gradient in the region is apparent. Around the northern repository some impact of the fracture zones on the pressure distribution can be seen as a decreased residual pressure caused by the conductive Zone 2, see Figure 5-5.

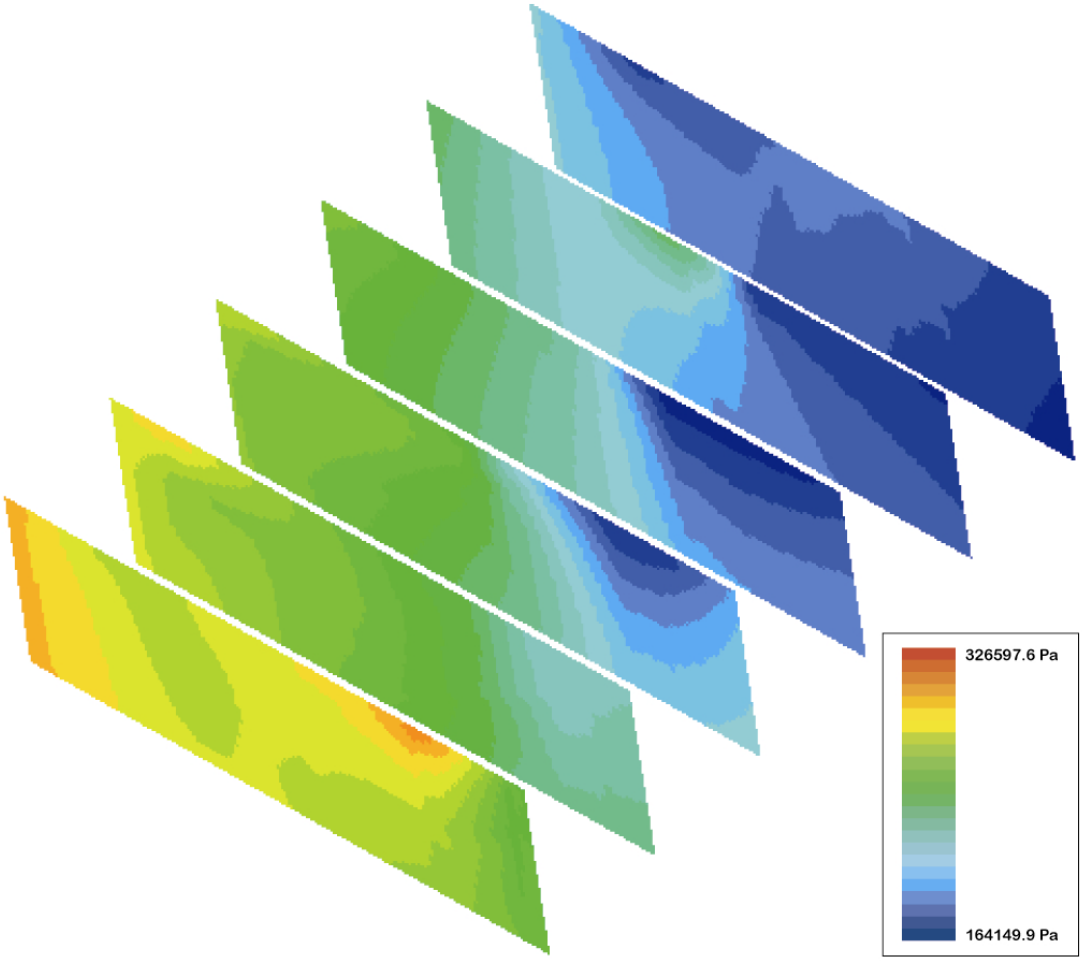

Figure 5-5 *The residual pressure distribution shown on six slices cutting through the model domain in the west-east direction for the BaseFine Case. The red colour indicates higher pressure and the blue colour indicates lower pressure. The pressure values (Pa) are given in the legend. View from the southeast.*

In Figure 5-6 the effects of the Imundbo Zone appears in the residual pressure distribution where the pressure contours are aligned with the zone. Apart from the discussed effects the impact of the fracture zones on the pressure distribution is difficult to see.

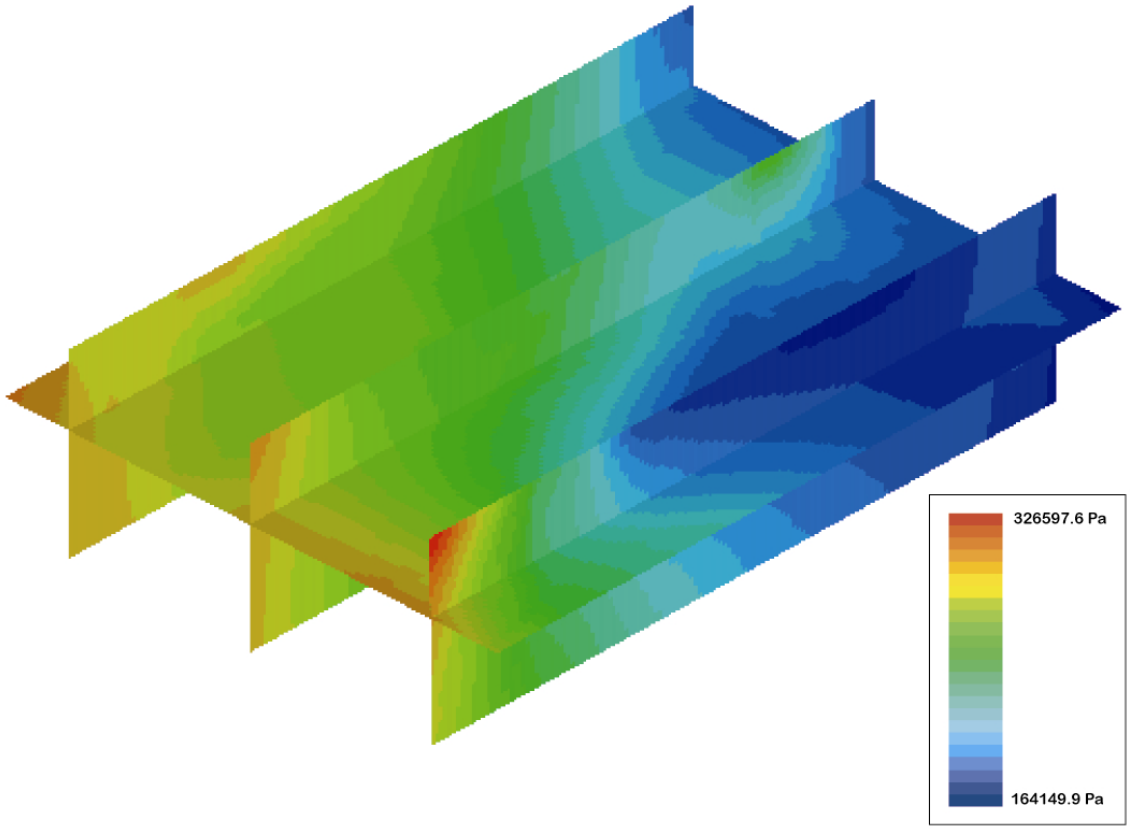

Figure 5-6 *The residual pressure distribution shown on four slices cutting through the model domain in the south-north direction for the BaseFine Case. The horizontal plane is placed at a depth of z = -604.5 m. The red colour indicates higher pressure and the blue colour indicates lower pressure. The pressure values (Pa) are given in the legend. View from the southeast.*

5.3.1 Exit Locations

A set of 120 particles were released at a depth of z = -604.5 m from the northern and southern blocks (the area of the repository), 109 from the northern block and 11 from the southern block. Figure 5-7 shows the pathlines in three views calculated with NAMMU. The pathlines are coloured with respect to travel time. The exit locations, shown in Figure 5-8, are defined as the points where the released particles reach the boundary in the model domain.

The pathlines are predominantly directed to the northeast through the rock mass away from the repository. This is also corresponding to the regional flow pattern. The discharge areas are found around the regional fracture zones situated northeast of the repository. The major part of the released particles exits within the Imundbo Zone. This is also where we find the pathlines with the longest travel times. A couple of these paths tend to follow Zone 1 until they reach the intersection with the Imundbo Zone where they discharge. The pattern of the pathlines for the BaseFine Case differs from the Base Case in a couple of ways. First, the pattern for the BaseFine Case is tighter. In the Base Case a lot of the pathlines went through the rock mass far north in the model. In the BaseFine Case the pathlines are more affected by Zone 5 and the Imundbo Zone and never reach as far north as in the Base Case. This gives a more concentrated pathline field. Another difference between the variants is that the pathlines are more horizontal in the BaseFine Case while the pathlines go deeper in the Base Case and even exit through the bottom of the model a couple of times which never happens in the BaseFine Case. The reason why the pathlines are more horizontal and not so deep in the BaseFine Case compared to the Base Case is probably the different representation of the permeability field. The methods used calculating the permeability field for the Base Case overestimates the vertical permeability, which results in deeper pathlines. The pathline pattern for the BaseFine Case is in better agreement with the results from HYDRASTAR compared to the Base Case.

The permeable Zone 2 is an important feature in both the Base Case and the BaseFine Case. A group of particles follows Zone 2 upward in a northeast direction until they reach the discharge areas in Zones 1, 3 and 4. These particles are the ones with the shortest travel times in this variant. All the particles released from the southern repository follow the same path as they did in the Base Case, at the beginning horizontally through the rock mass until they reach the Imundbo Zone where they exit vertically. These pathlines clearly demonstrate the influence of the fracture zones. A few particles are stuck between the second and the third element from the top of the model. This is probably caused by the numerical problems arising from counteracting pressure gradients near the model top surface.

The exit locations and travel times are roughly comparable to those of the regional steady state freshwater model used to determine the boundary conditions for this study.

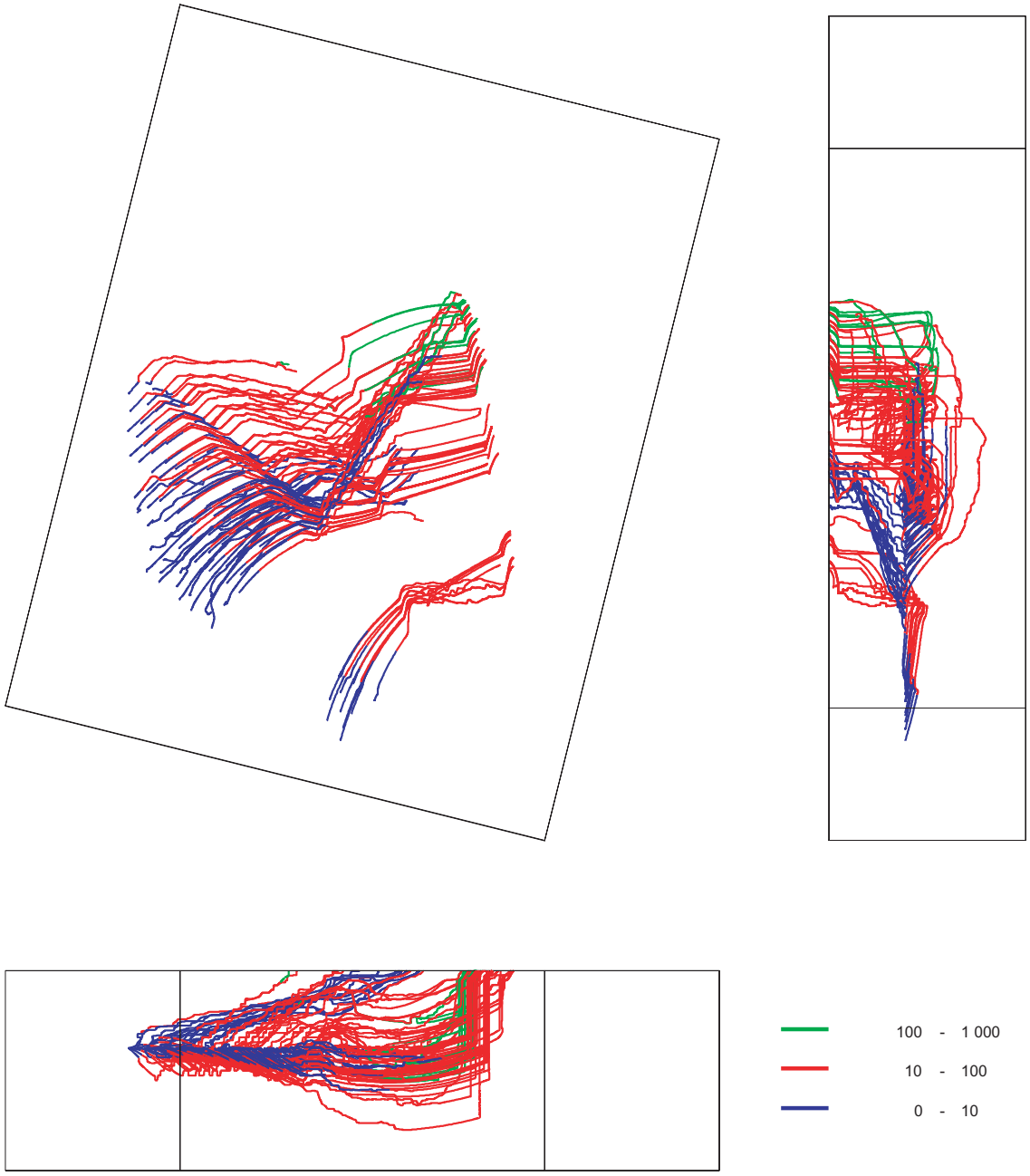

Figure 5-7 *Forward pathlines for the BaseFine Case. A set of 120 particles are released at a depth of z = -604.5 m, 109 from the northern block and 11 from the southern block. The pathlines are coloured with respect to travel time given in years. Upper left: Plan view of the model from above. Upper right: Elevation view from the east. Lower left: Elevation view from the south.*

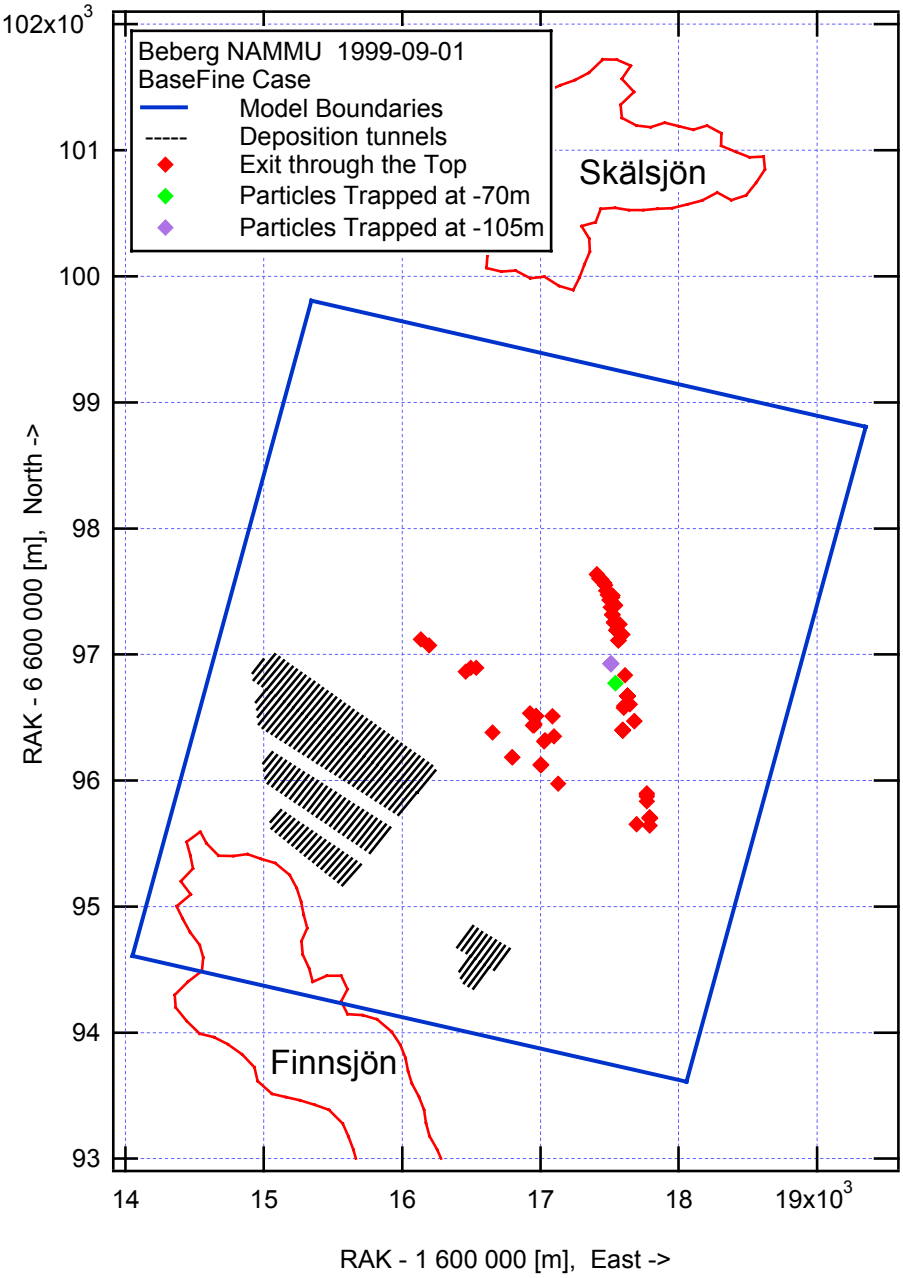

Figure 5-8 *Exit locations for the released particles in the BaseFine Case. The red markers show particles exiting the top of the model. The green and the purple markers show particles that are stuck in the model at a level of -70 m and -105 m respectively and not reaching any of the model boundaries. View from the top of the model.*

5.3.2 Boundary Flow

Figure 5-9 shows the boundary flows for the BaseFine Case. The direction of the arrows denotes the direction of the net flow over the model surface. The size of the arrows has been altered to symbolise the magnitude of the flow. The actual size should only be regarded as an illustration and not as an exact measure. The pattern resembles the one in the Base Case and the direction of the boundary flows is in agreement with the regional flow pattern.

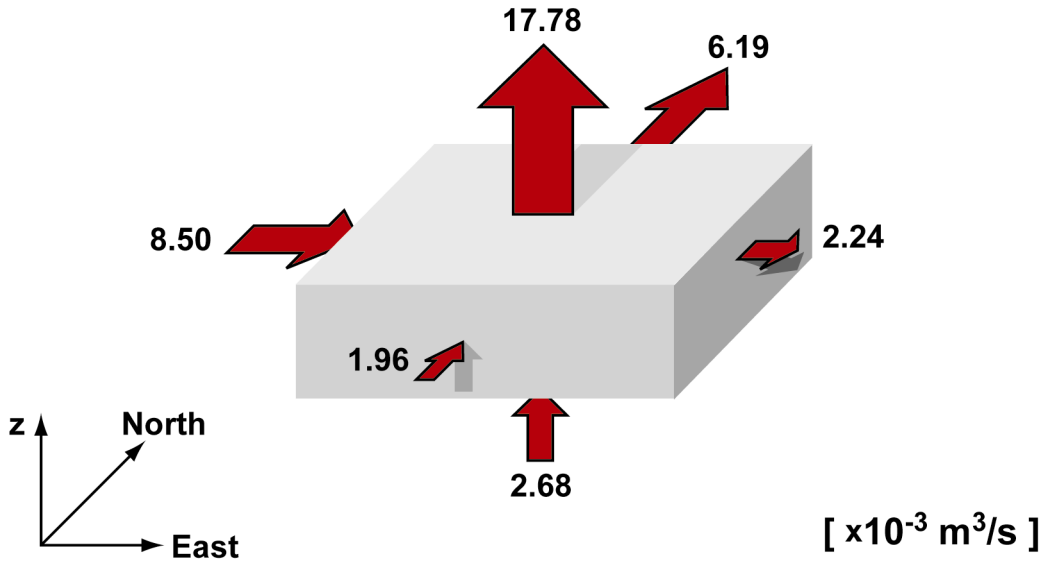

Figure 5-9 *Boundary flows for the BaseFine Case. Arrows show the direction of the calculated net flow through each of the boundary surfaces.*

Table 5-1 summarises the calculated groundwater boundary flows for the BaseFine Case. A positive boundary flow is directed out from the model domain. Although the directions of the flow coincide with the regional flow pattern, i.e. in the northeast direction, the calculated mass balance shows a large discrepancy. Looking at the net flows, the outflow from the model is about a factor two larger than the inflow to the model. Studying the gross flows for each surface of the model gives us an explanation to the discrepancy in the mass balance. In fact, the total residual from the mass balance is only about 15 % of the gross flows through the top boundary surface, which is also the predominating outflow area.

Table 5-1 **Groundwater flow through the model boundaries for the BaseFine Case. Positive flow is directed out from the model.**

Site Model Surface	Gross Inflow [$\cdot 10^{-3}$ m^3/s]	Gross Outflow [$\cdot 10^{-3}$ m^3/s]	Net Flow through Surface [$\cdot 10^{-3}$ m^3/s]
Top	-81.73	99.51	17.78
Bottom	-6.20	3.51	-2.68
South	-2.04	0.08	-1.96
North	-0.01	6.20	6.19
West	-8.79	0.30	-8.50
East	-3.01	5.25	2.24
Total Inflow	-101.78	-	-13.14
Total Outflow	-	114.85	26.21
Mass balance			***13.07***

5.4 Statistics

Table 5-2 shows the statistical summary of the 120 canister positions in the BaseFine Case. The calculated performance measures are travel time (TT) and canister flux (CF). The travel time is the time used by the particles released in the model to be transported by advection from the starting position to any boundary of the model domain. The canister flux is the Darcy groundwater velocity calculated by NAMMU as the resultant of the three velocity components (u_x, u_y and u_z) at each of the 120 particle starting positions.

All particles are released at a depth of -604.5 m. For the statistical calculations the particles were also grouped with respect to what boundary they exited through.

Table 5-2 Statistical summary for the BaseFine Case.

Statistics	$Log_{10}(TT_{tot})$	$Log_{10}(TT_{top})$	$Log_{10}(CF)$
Mean	1.688	1.666	-2.619
Median	1.846	1.828	-2.706
5th Percentile	0.741	0.730	-2.897
25th Percentile	1.570	1.510	-2.837
75th Percentile	1.963	1.958	-2.503
95th Percentile	2.131	2.131	-2.272
St Deviation	0.442	0.454	0.368
Variance	0.195	0.206	0.136
Min Value	0.004	0.004	-2.914
Max Value	2.177	2.177	-0.609
Fraction	1.000	0.917	1.000

5.4.1 Travel Time

Table 5-2 summarises the result for the travel time and indicates a median travel time of 67 years, with an interquartile range from 32 years to 91 years for the particles exiting through the top of the model. The variance of the $\log_{10}$(TT) for the particles exiting through the top is 0.206. The 5^{th} percentile is approximately 5 years which tells us that a few particles reach the top boundary very quickly. These particles are all released from within the northern repository and most of them follow Zone 2 up to the top. 91.7 % of the released particles are exiting through the top of the model. The rest of the particles are stuck in the model due to numerical difficulties. No particles exit through the bottom of the model. Figure 5-10 presents the relative frequency histogram of $\log_{10}$ travel time for 120 starting positions. The histogram is normalised with respect to the total number of starting positions. The lower tail in the histogram (<10 years) represents the fast particles released from within the northern repository following Zone 2 up to the top of the model.

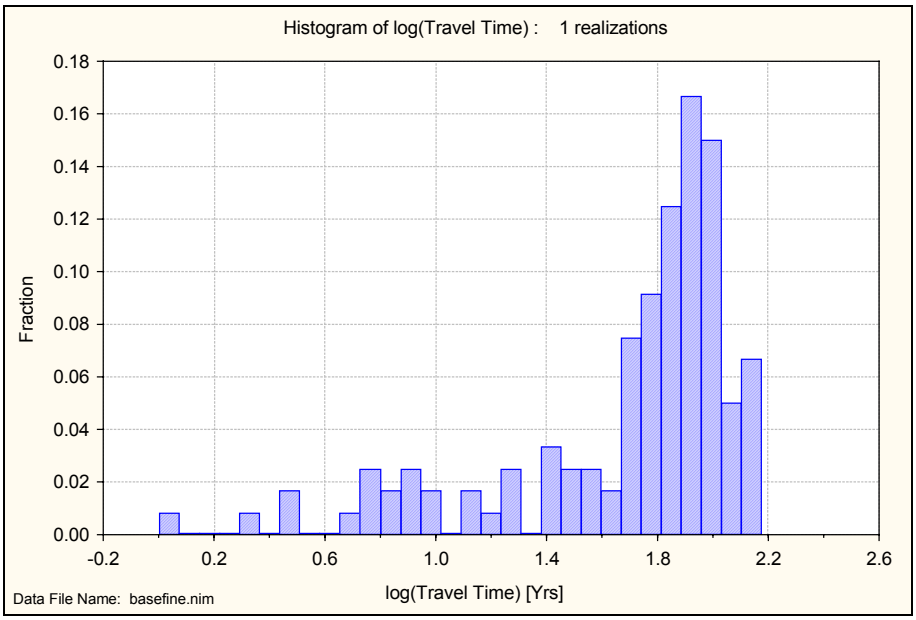

Figure 5-10 *Relative frequency histogram of $\log_{10}$ travel time for the BaseFine Case. The histogram is normalised with respect to the total number of starting positions. Results for 120 starting positions.*

Figure 5-11 presents the floating histogram of $\log_{10}$ travel time for 120 starting positions. The histogram is normalised with respect to the total number of starting positions and it is slightly skewed with a larger lower tail.

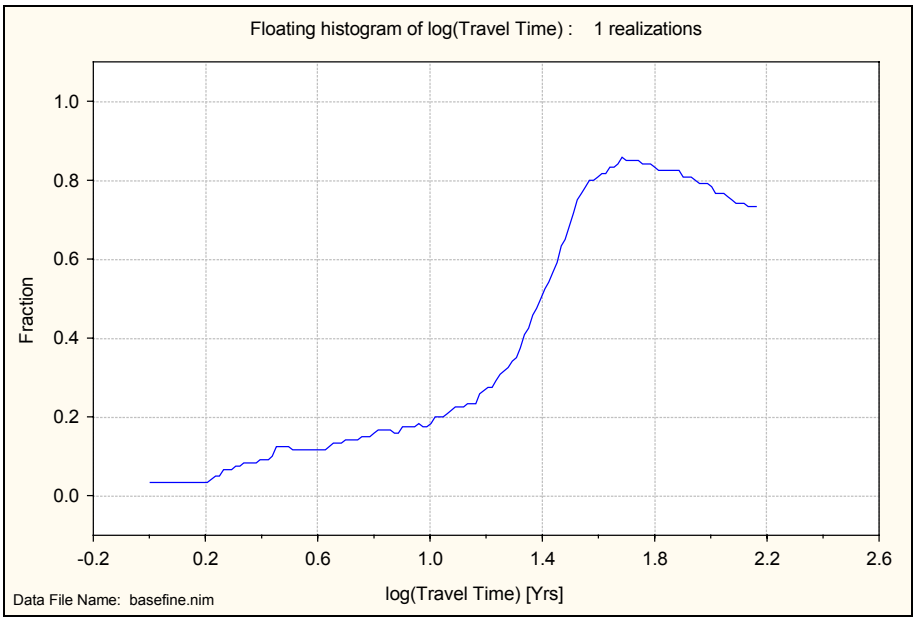

Figure 5-11 *Floating histogram of $\log_{10}$ travel time for the BaseFine Case. The histogram is normalised with respect to the total number of starting positions. Results for 120 starting positions.*

Figure 5-12 presents a box plot of $\log_{10}$ travel time for 120 starting positions.

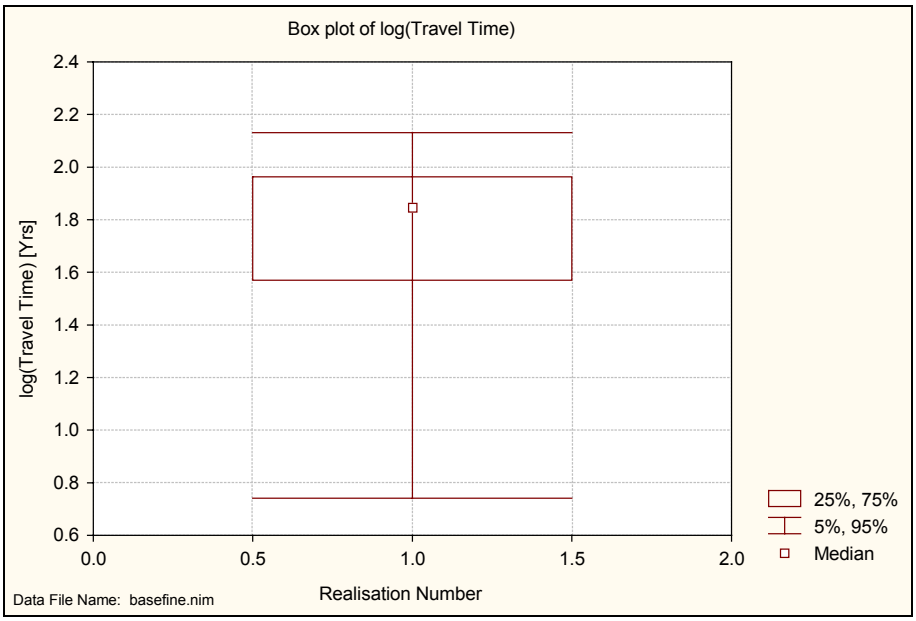

Figure 5-12 *Box plot of $\log_{10}$ travel time showing the median and the 5th, 25th, 75th and 95th percentiles for the BaseFine Case. Results for 120 starting positions.*

5.4.2 Canister Flux

Table 5-2 summarises the result for the canister flux and indicates a median canister flux of $2.0 \cdot 10^{-3}$ m/year, with an interquartile range from $1.5 \cdot 10^{-3}$ m/year to $3.1 \cdot 10^{-3}$ m/year. When calculating the canister flux the particles are not divided into subgroups since the canister flux is measured at the starting position and therefore independent of exit location. The variance of the $\log_{10}$(CF) for all particles is 0.136. Figure 5-13 presents the relative frequency histogram of $\log_{10}$ canister flux for 120 starting positions. The histogram is normalised with respect to the total number of starting positions and is slightly skewed with a larger upper tail, this can also been seen in Figure 5-14.

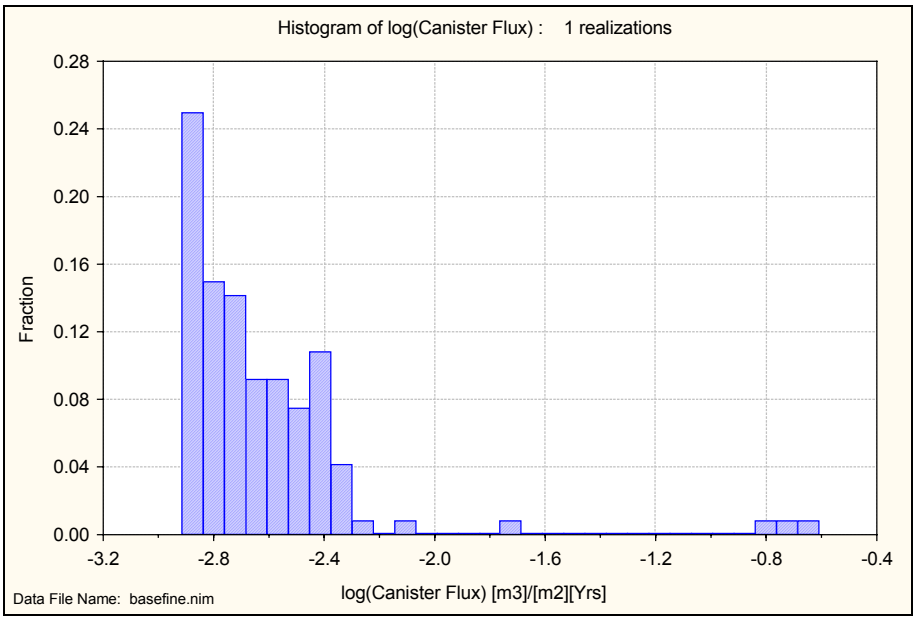

Figure 5-13 *Relative frequency histogram of log_{10} canister flux for the BaseFine Case. The histogram is normalised with respect to the total number of starting positions. Results for 120 starting positions.*

Figure 5-14 presents the floating histogram of log_{10} canister flux for 120 starting positions. The histogram is normalised with respect to the total number of starting positions.

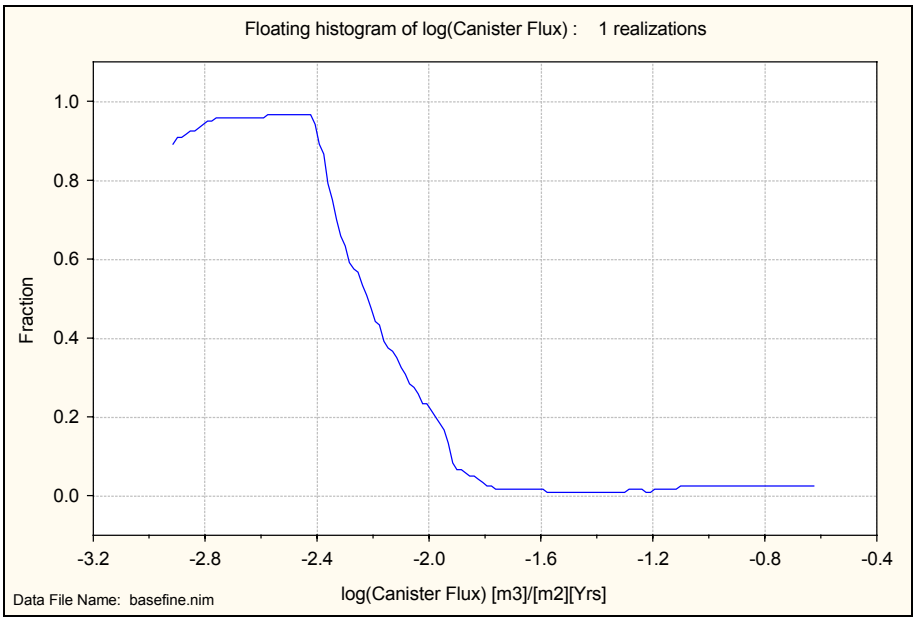

Figure 5-14 *Floating histogram of log_{10} canister flux for the BaseFine Case. The histogram is normalised with respect to the total number of starting positions. Results for 120 starting positions.*

Figure 5-15 presents a box plot of $\log_{10}$ canister flux for the single realisation with 120 starting positions.

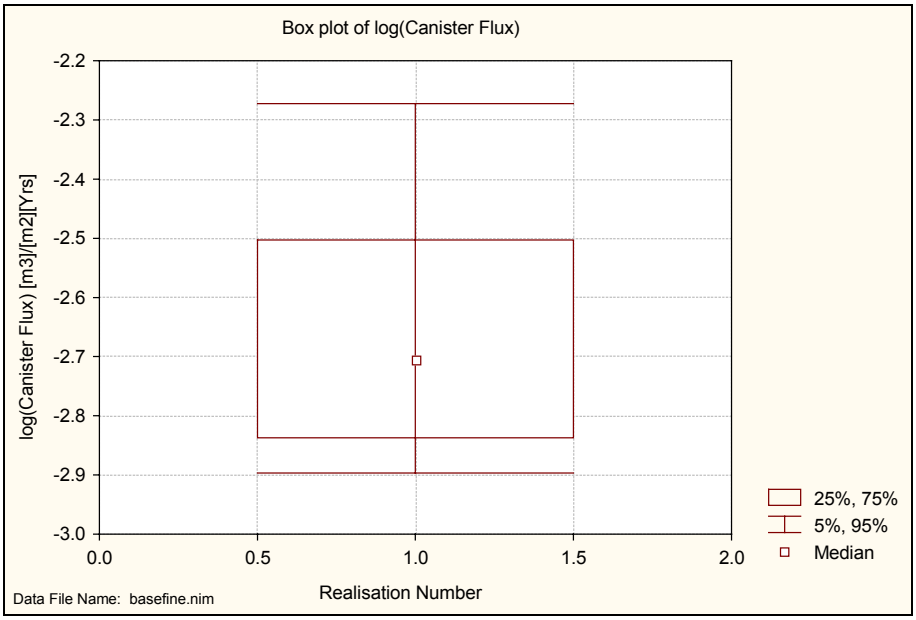

Figure 5-15 *Box plot of $\log_{10}$ canister flux showing the median and the 5^{th}, 25^{th}, 75^{th} and 95^{th} percentiles for the BaseFine Case. Results for 120 starting positions.*

Figure 5-16 presents a scatter plot of $\log_{10}$ travel time versus $\log_{10}$ canister flux and traces of the inverse correlation between the two parameters can be observed in the figure.

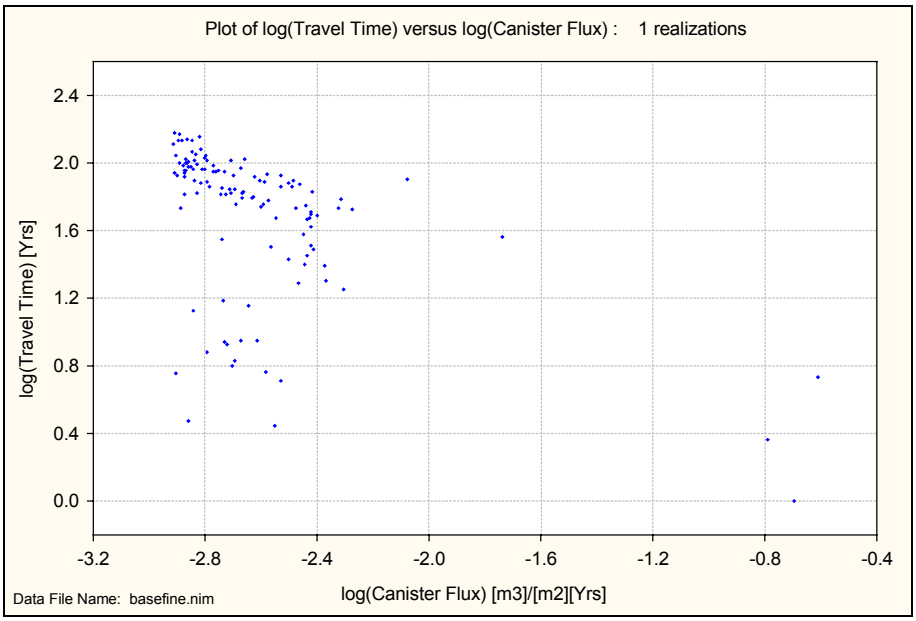

Figure 5-16 Scatter plot of $\log_{10}$ travel time versus $\log_{10}$ canister flux for the BaseFine Case. Results for 120 starting positions.

6 Anisotropic Case

This variant was set up to study the effects of anisotropy in the rock mass. The properties of the used anisotropy are in agreement with the values used within the large scale regional modelling of Beberg *[Hartley et al., 1998]*.

The constant residual pressure (Dirichlet) boundary conditions used in the Anisotropic Case are the same as for the Base Case presented earlier in the report. The boundary conditions are visualised in Figure 4-1. It is important to note that the major axis of the permeability is orthogonal to the general regional hydraulic gradient.

6.1 Permeability Field

Figure 6-1 - Figure 6-4 visualise the $\log_{10}$ of the horizontal and the vertical permeability field used for the Anisotropic Case. In this variant, the permeability field used for the Base Case was adjusted for the effects of hydraulic anisotropy in the region and used here. The direction of the major axis was set to N 45 W. The degree of anisotropy in the horizontal permeability is 10:1:1 (horizontal major:horizontal minor:vertical). See section 3.2.3 for details regarding the permeability field. The red colour indicates higher permeability and the blue colour indicates lower permeability.

Studying the definitions of the anisotropic permeability tensor in section 3.2.3 indicates that the horizontal permeability should be a factor 5.5 larger than the vertical permeability. However, comparing Figure 6-1 with Figure 6-2 it appears like there are no differences between the horizontal and the vertical permeability fields. The explanation is that AVIZIER scales the range of each data set to the defined colour range. In reality, the horizontal permeability is a factor 5.5 larger than the vertical permeability but this information is lost in the visualisation. The horizontal permeability range from $3.3 \cdot 10^{-15}$ m^2 to $3.3 \cdot 10^{-11}$ m^2 and the vertical permeability range from $6.0 \cdot 10^{-16}$ m^2 to $6.0 \cdot 10^{-12}$ m^2.

The highly permeable top layer appears in a lighter colour in Figure 6-1 - Figure 6-4 and so do the two repository areas. Another interesting feature is the highly permeable Zone 2 situated directly above the northern repository.

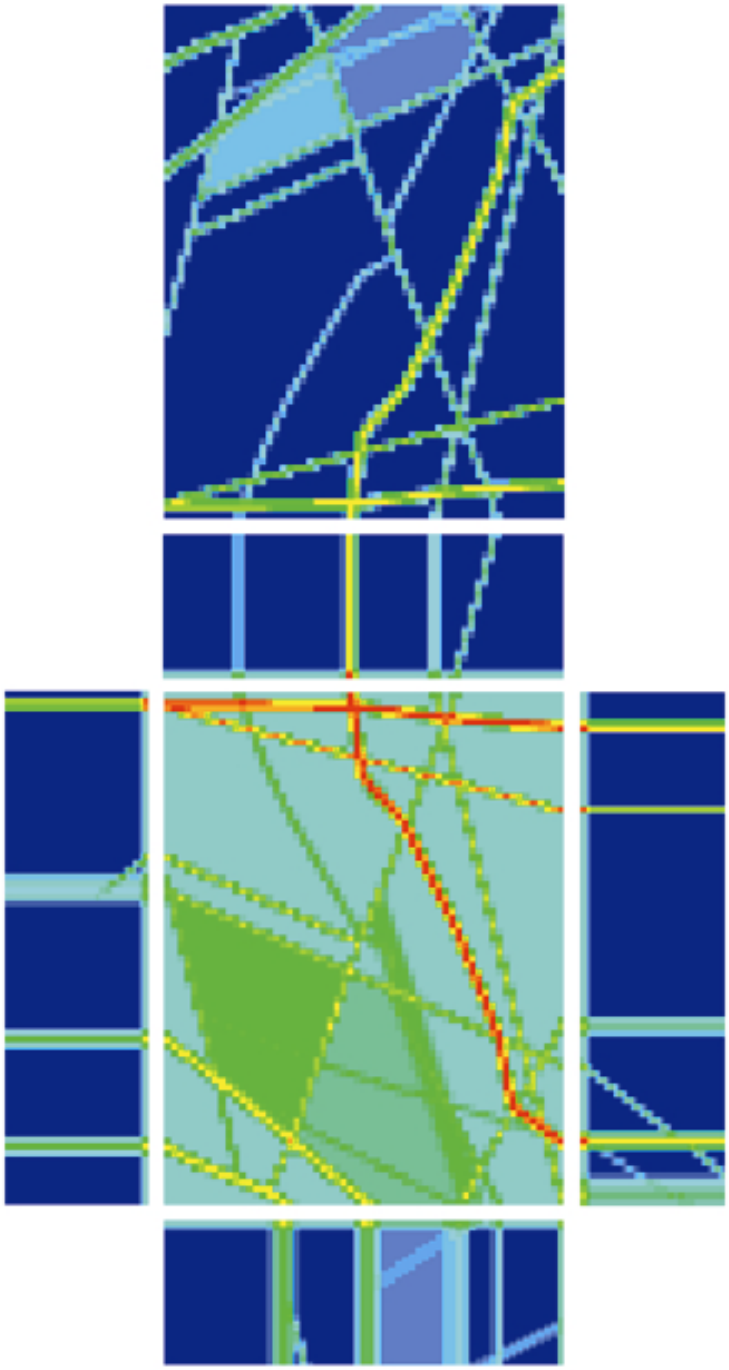

Figure 6-1 *The $\log_{10}$ of the horizontal permeability field on each face of the model domain for the Anisotropic Case. The red colour indicates higher permeability and the blue colour indicates lower permeability.*

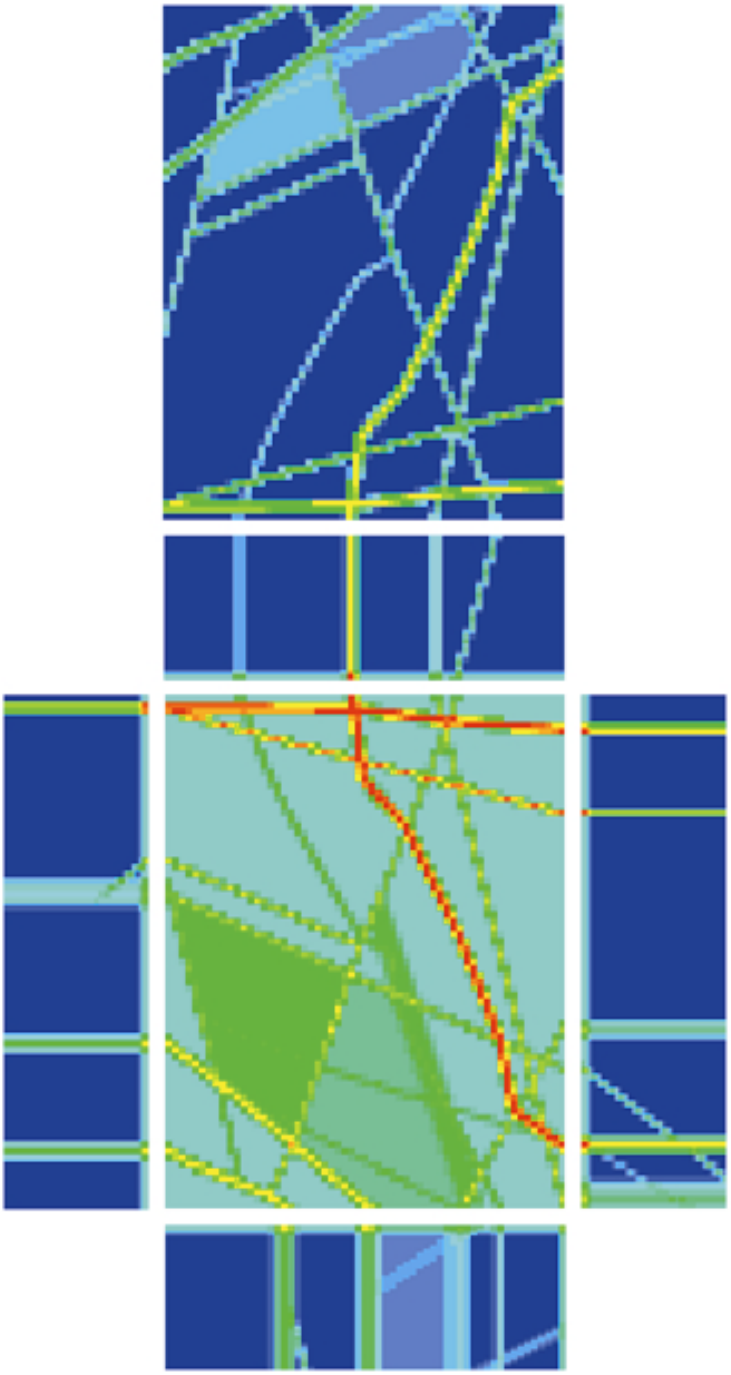

Figure 6-2 *The $\log_{10}$ of the vertical permeability field on each face of the model domain for the Anisotropic Case. The red colour indicates higher permeability and the blue colour indicates lower permeability.*

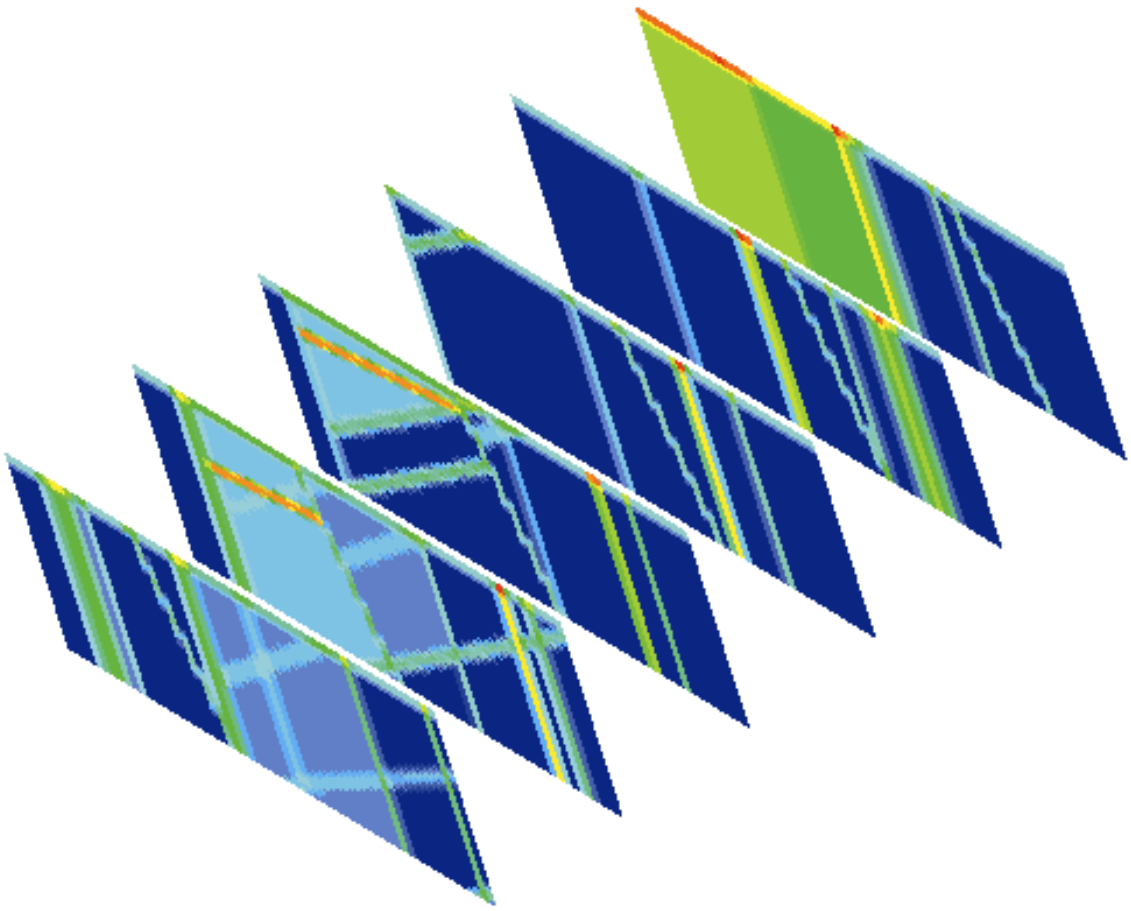

Figure 6-3 *The $\log_{10}$ of the horizontal permeability field distribution shown on six slices cutting through the model domain in the west-east direction for the Anisotropic Case. The red colour indicates higher permeability and the blue colour indicates lower permeability. View from the southeast.*

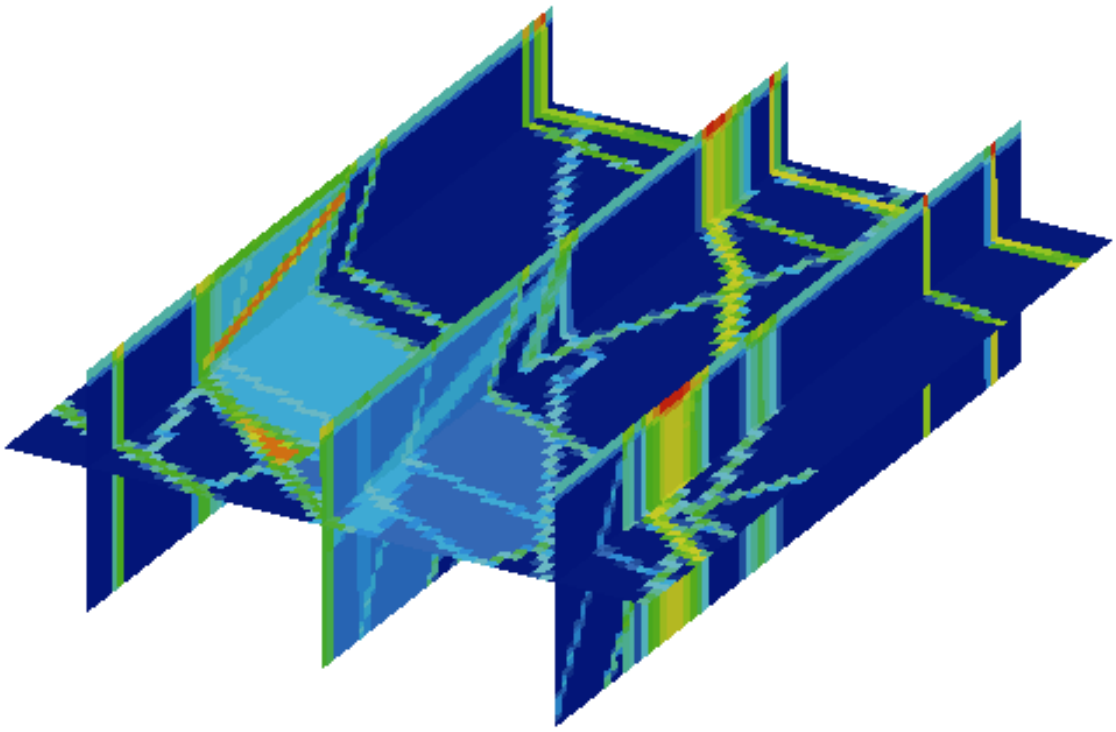

Figure 6-4 *The $\log_{10}$ of the horizontal permeability field shown on four slices cutting through the model domain in the south-north direction for the Anisotropic Case. The horizontal plane is placed at a depth of z = -604.5 m. The red colour indicates higher permeability and the blue colour indicates lower permeability. View from the southeast.*

6.2 Results

Figure 6-5 and Figure 6-6 show the calculated residual pressure distribution on slices cutting through the model domain for the Anisotropic Case. The view of the model is taken from the southeast for both figures. The hydraulic head range from 16.6 m to 33.4 m. The residual pressure can be thought of as a driving pressure in the model, see section 3.5.1 for the definition. The red colour indicates higher pressure and the blue colour indicates lower pressure. The northeast direction of the major hydraulic gradient in the region is apparent. Some impact on the pressure distribution around the northern repository can be seen as a decreased residual pressure caused by the conductive Zone 2, see Figure 6-5.

In Figure 6-6 the effects of the Imundbo Zone appears in the residual pressure distribution where the pressure contours are aligned with the zone. Apart from the discussed effects the impact of the fracture zones on the pressure distribution is difficult to see.

The effect of hydraulic anisotropy in the region appears clearly in Figure 6-5 and Figure 6-6 compared to the results from the Base Case. The direction of the minor horizontal axis is roughly the same as the direction of the major hydraulic gradient, i.e. to the northeast. The hydraulic head loss is higher in this direction compared to the direction of the major horizontal axis. This result corresponds to the degree of anisotropy in the horizontal hydraulic permeability of 10:1:1 *(horizontal major:horizontal minor:vertical* direction respectively) which gives a lower permeability in the minor horizontal direction compared to the major direction. A lower permeability will result in a higher head loss.

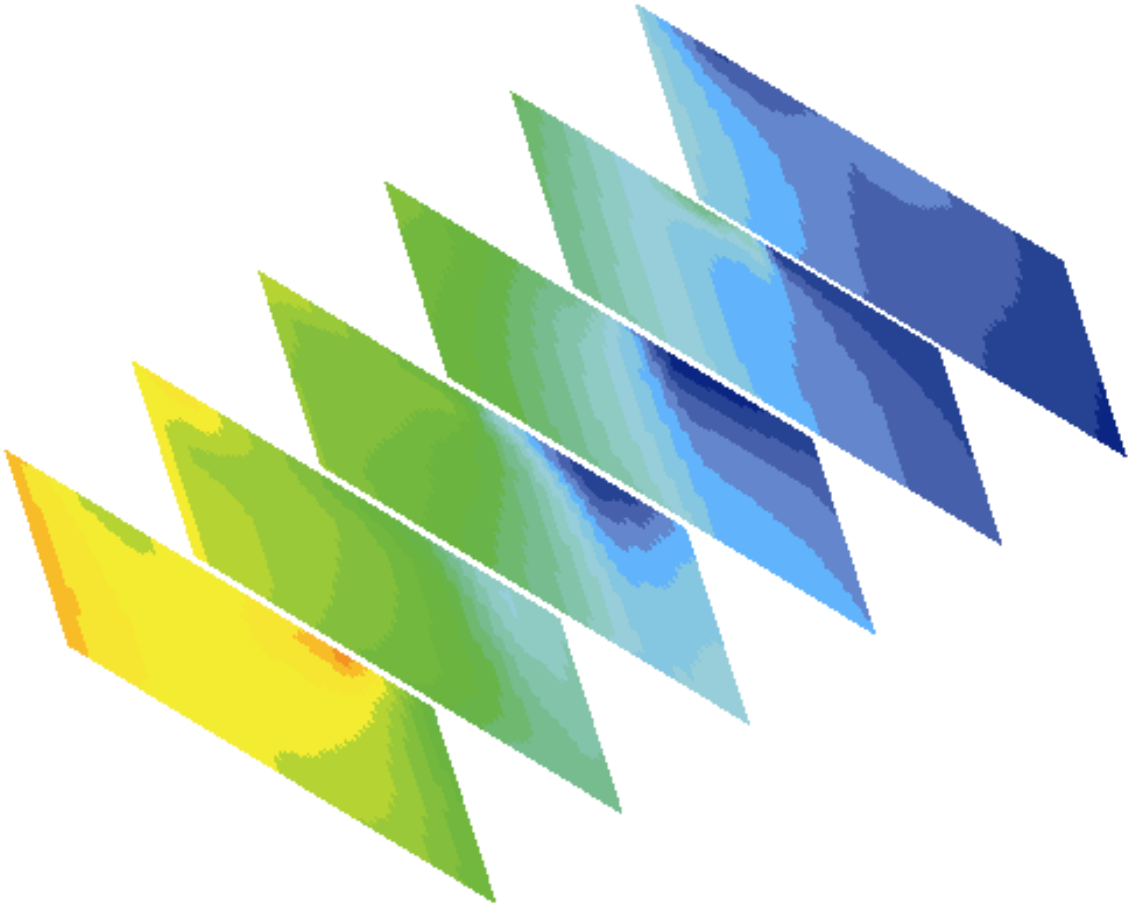

Figure 6-5 *The residual pressure distribution shown on six slices cutting through the model domain in the west-east direction for the Anisotropic Case. The red colour indicates higher pressure and the blue colour indicates lower pressure. View from the southeast.*

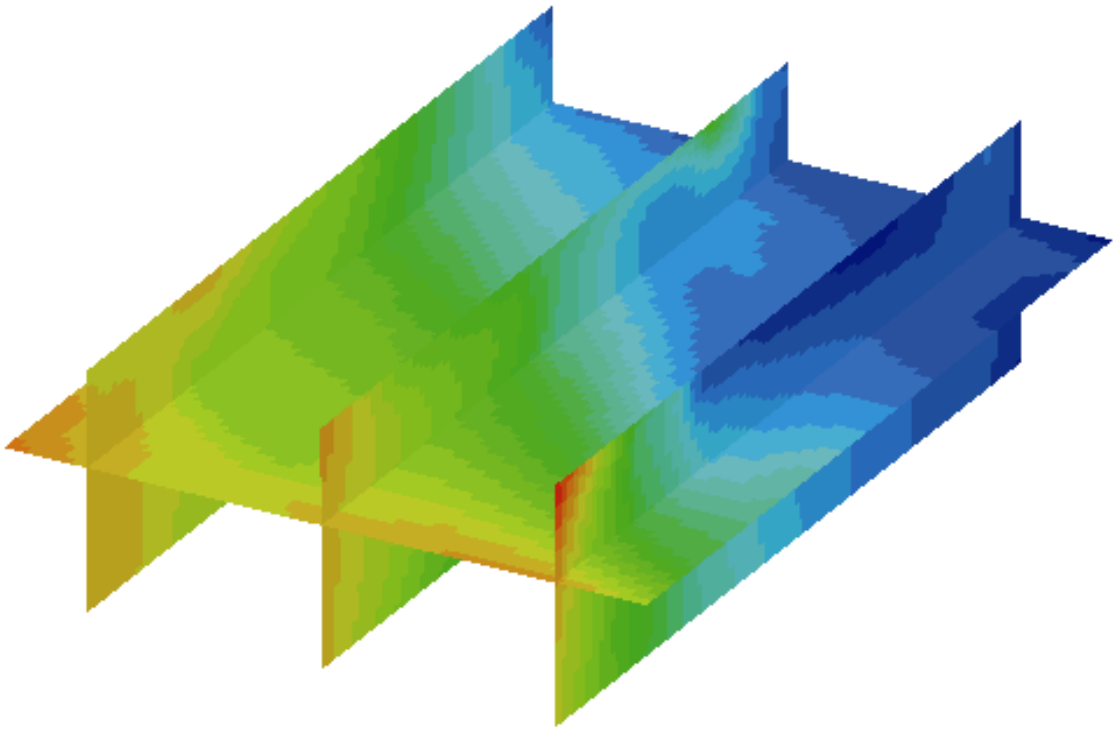

Figure 6-6 *The residual pressure distribution shown on four slices cutting through the model domain in the south-north direction for the Anisotropic Case. The horizontal plane is placed at a depth of z = -604.5 m. The red colour indicates higher pressure and the blue colour indicates lower pressure. View from the southeast.*

6.2.1 Exit Locations

A set of 120 particles were released at a depth of z = -604.5 m from the northern and southern blocks (the area of the repository), 109 from the northern block and 11 from the southern block. Figure 6-7 shows the pathlines in three views calculated with NAMMU. The pathlines are coloured with respect to travel time. The exit locations, shown in Figure 6-8, are defined as the points where the released particles reach the boundary in the model domain.

Compared to the Base Case the pathlines in the Anisotropic Case are clearly affected by the anisotropy. The direction of the particles is mainly horizontal with the exception of a group released from the northern repository that follows the permeable Zone 2 upwards. The particles following Zone 2 have the shortest travel times (less than 10 years up to the top of the model) among the released particles. The particles released from the northern repository travel almost north through the rock mass until they reach Zone 5 and Zone 4. Here the effect of the anisotropy is striking, the particles turn 90° clockwise and follow the zones southeast until they reach the intersection between Zone 1 and Zone 5. Here a couple of particles turn north and follow Zone 1 for a while and then cross the rock mass over to the Imundbo Zone where they exit through the top of the model. Among the particles with horizontal pathlines exiting in the Imundbo Zone we find those with the longest travel times. Some of the particles leaving Zone 4 and Zone 5 go straight to the Imundbo Zone where they exit through the top of the model.

Initially all the particles released in the southern repository roughly follow the same way through the rock mass. In the beginning, they travel horizontally through the rock mass in the northwest direction. A few particles then enter Zone 1 and follow it north until they finally discharge in the Imundbo Zone. The other group of particles released in the southern repository never reaches Zone 1 but cross the rock mass and enter Zone 5, which they follow to the exit location in the Imundbo Zone.

A few particles exit through the top of the model in Zone 3 but the Imundbo Zone is the predominating exit area in the Anisotropic Case. No particles exit through the bottom of the model, as was the case in the Base Case. The pathlines do not reach quite as far north in the Imundbo Zone as they did in the Base Case.

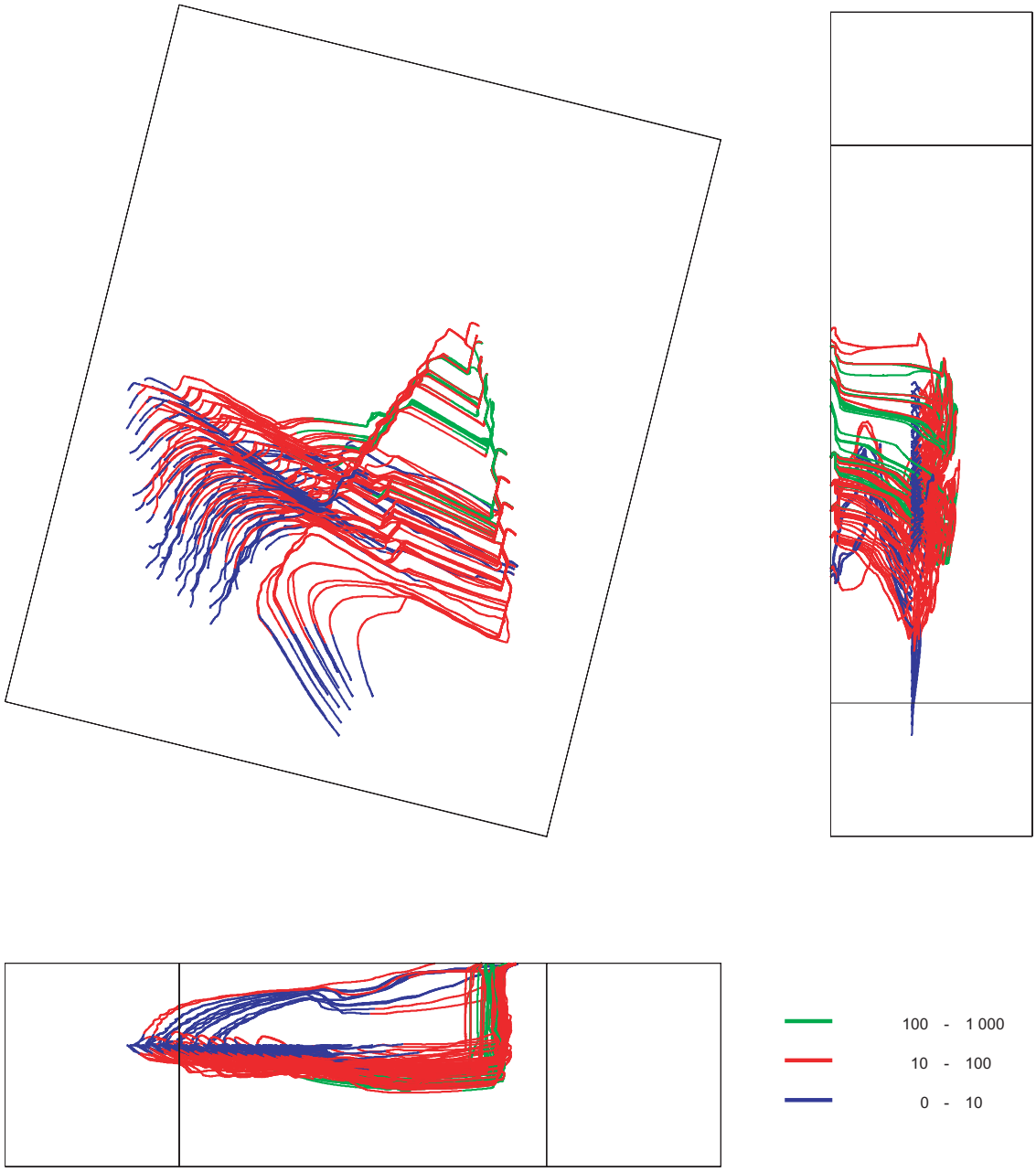

Figure 6-7 *Forward pathlines for the Anisotropic Case. A set of 120 particles are released at a depth of z = -604.5 m, 109 from the northern block and 11 from the southern block. The pathlines are coloured with respect to travel time given in years. Upper left: Plan view of the model from above. Upper right: Elevation view from the east. Lower left: Elevation view from the south.*

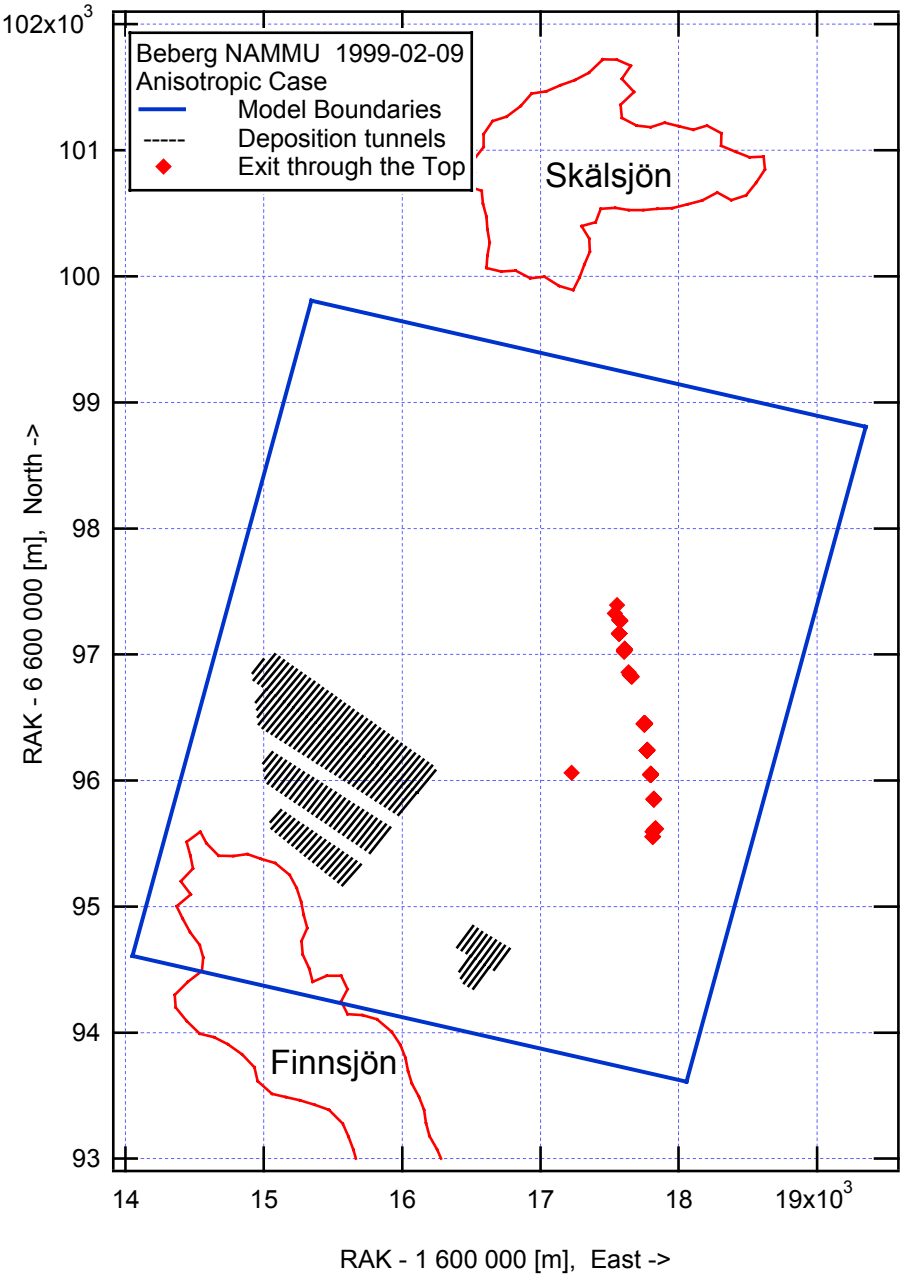

Figure 6-8 *Exit locations for the released particles in the Anisotropic Case. The red markers show particles exiting the top of the model. View from the top of the model.*

6.2.2 Boundary Flow

Figure 6-9 shows the boundary flows for the Anisotropic Case. The direction of the arrows denotes the direction of the net flow over the model surface. The size of the arrows has been altered to symbolise the magnitude of the flow. The actual size should only be regarded as an illustration and not as an exact measure. The direction of the boundary flows is basically in agreement with the regional flow pattern.

Apart from the size of the flow through the different boundary surfaces, there are a couple of other changes in the flow pattern compared to the Base Case. The flow through the eastern boundary is directed in to the model domain and the flow through the bottom boundary is directed out from the model in the Anisotropic Case.

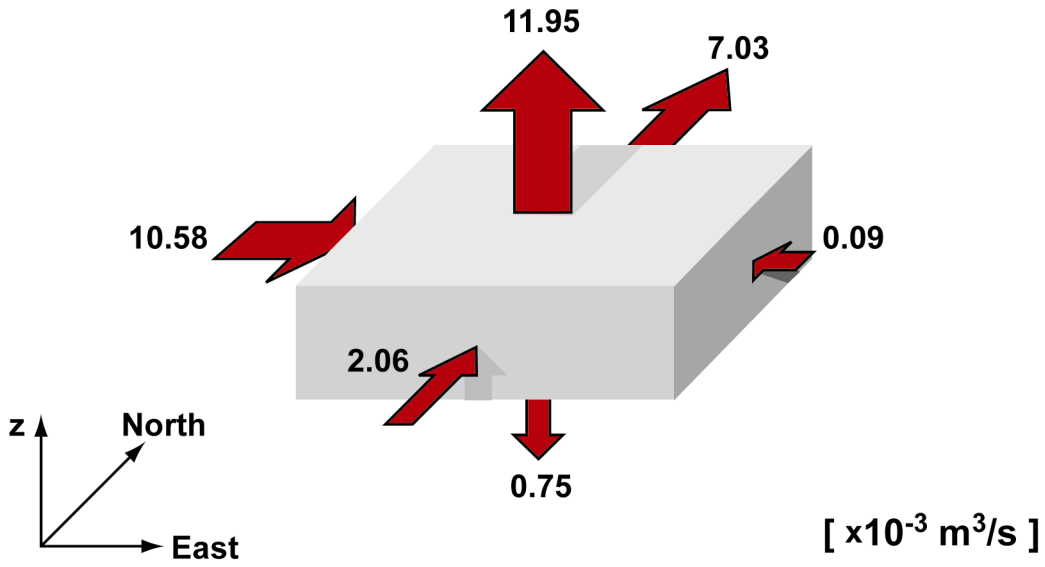

Figure 6-9 *Boundary flows for the Anisotropic Case. Arrows show the direction of the calculated net flow through each of the boundary surfaces.*

Table 6-1 summarises the calculated groundwater boundary flows for the Anisotropic Case. A positive boundary flow is directed out from the model domain. Although the directions of the flow coincide with the regional flow pattern, i.e. in the northeast direction, the calculated mass balance shows some discrepancy. Looking at the net flows, the outflow from the model is about a factor 1.5 larger than the inflow to the model. Studying the gross flows for each surface of the model gives us an explanation to the discrepancy in the mass balance. In fact, the total residual from the mass balance is only about 10 % of the gross flows through the top boundary surface, which is also the predominating outflow area.

Table 6-1 Groundwater flow through the model boundaries for the Anisotropic Case. Positive flow is directed out from the model.

Site Model Surface	Gross Inflow [$\cdot 10^{-3}$ m^3/s]	Gross Outflow [$\cdot 10^{-3}$ m^3/s]	Net Flow through Surface [$\cdot 10^{-3}$ m^3/s]
Top	-60.86	72.82	11.95
Bottom	-0.97	1.72	0.75
South	-2.45	0.39	-2.06
North	-0.04	7.07	7.03
West	-10.81	0.22	-10.58
East	-4.96	4.88	-0.09
Total Inflow	-80.09	-	-12.73
Total Outflow	-	87.09	19.73
Mass balance			***7.00***

6.3 Statistics

Table 6-2 shows the statistical summary of the 120 canister positions in the Anisotropic Case. The calculated performance measures are the travel time (TT) and the canister flux (CF). The travel time is the time used by the particles released in the model to be transported by advection from the starting position to any boundary of the model domain. The canister flux is the Darcy groundwater velocity calculated by NAMMU as the resultant of the three velocity components (u_x, u_y and u_z) at each of the 120 stream tube starting positions.

All particles are released at a depth of -604.5 m. For the statistical calculations the particles were also grouped with respect to what boundary they exited through. In the Anisotropic Case all released particles exited through the top of the model so the values for both the total and the top group are the same.

Table 6-2 Statistical summary for the Anisotropic Case.

Statistics	$Log_{10}(TT_{tot})$	$Log_{10}(TT_{top})$	$Log_{10}(CF)$
Mean	1.850	1.850	-2.706
Median	1.930	1.930	-2.795
5th Percentile	0.923	0.923	-2.946
25th Percentile	1.821	1.821	-2.895
75th Percentile	2.099	2.099	-2.624
95th Percentile	2.200	2.200	-2.167
St Deviation	0.369	0.369	0.255
Variance	0.136	0.136	0.065
Min Value	0.447	0.447	-3.062
Max Value	2.240	2.240	-1.922
Fraction	1.000	1.000	1.000

6.3.1 Travel Time

Table 6-2 summarises the result for the travel time and indicates a median travel time of 85 years, with an interquartile range from 66 years to 125 years. The variance of the $\log_{10}$(TT) is 0.136. The 5^{th} percentile is 8 years which indicates that a few particles reach the top boundary very quickly. No particles were stuck in the model for the Anisotropic Case. Figure 6-10 presents the relative frequency histogram of $\log_{10}$ travel time for 120 starting positions. The histogram is normalised with respect to the total number of starting positions and is clearly skewed with a larger lower tail, this can also be seen in Figure 6-11. The lower tail (<10 years) represents the fast particles released from within the northern repository following Zone 2 up to the top of the model.

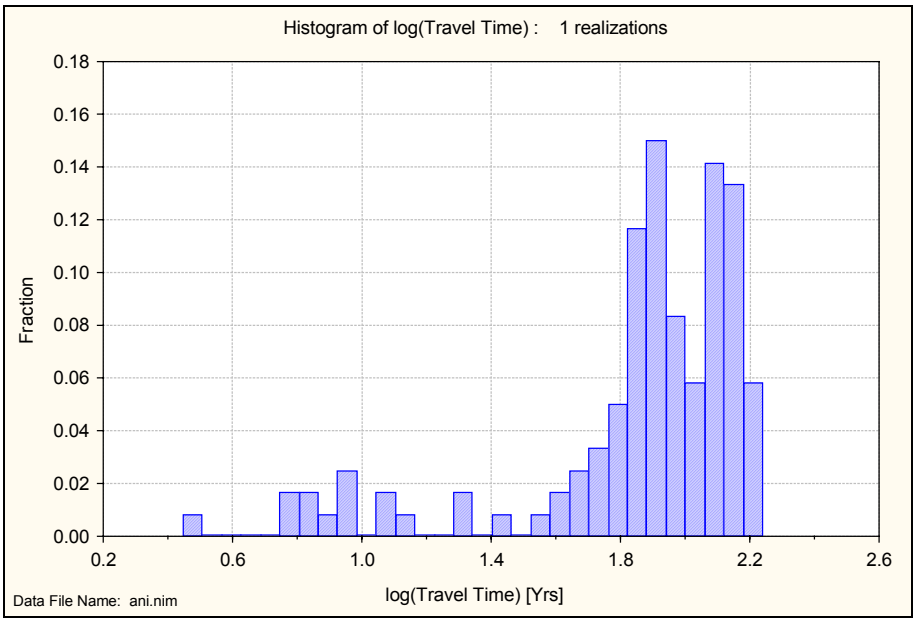

Figure 6-10 *Relative frequency histogram of log_{10} travel time for the Anisotropic Case. The histogram is normalised with respect to the total number of starting positions. Results for 120 starting positions.*

Figure 6-11 presents the floating histogram of log_{10} travel time for 120 starting positions. The histogram is normalised with respect to the total number of starting positions.

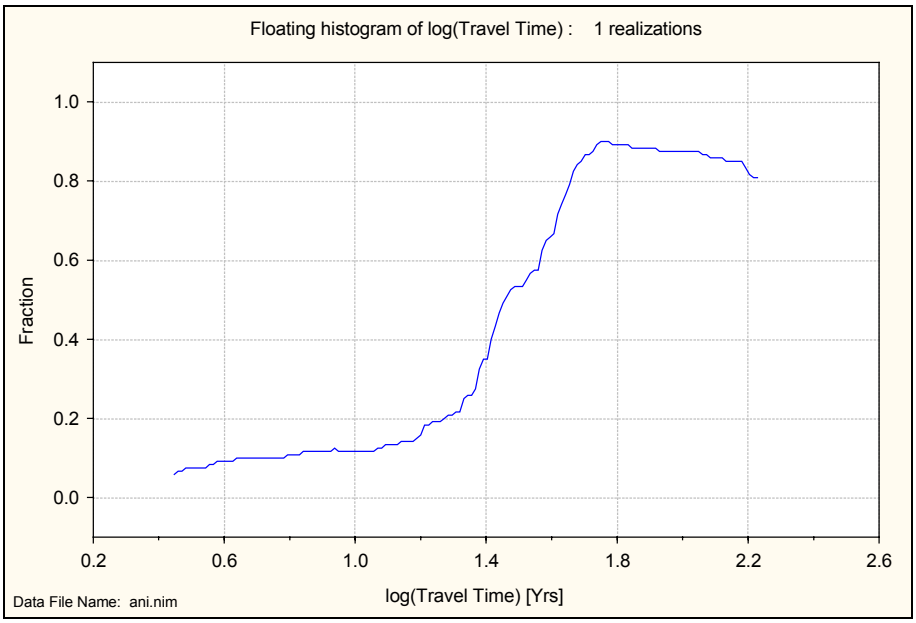

Figure 6-11 *Floating histogram of log_{10} travel time for the Anisotropic Case. The histogram is normalised with respect to the total number of starting positions. Results for 120 starting positions.*

Figure 6-12 presents a box plot of $\log_{10}$ travel time for 120 starting positions.

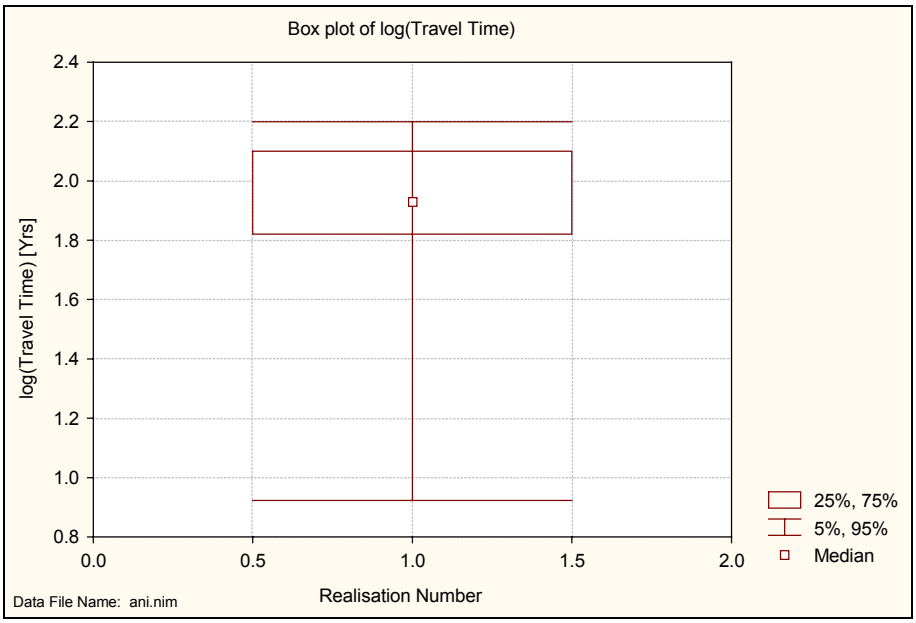

Figure 6-12 *Box plot of $\log_{10}$ travel time showing the median and the 5th, 25th, 75th and 95th percentiles for the Anisotropic Case. Results for 120 starting positions.*

6.3.2 Canister Flux

Table 6-2 summarises the result for the canister flux and indicates a median canister flux of $1.6 \cdot 10^{-3}$ m/year, with an interquartile range from $1.3 \cdot 10^{-3}$ m/year to $2.4 \cdot 10^{-3}$ m/year. When calculating the canister flux the particles are not divided into subgroups since the canister flux is measured at the starting position and therefore independent of exit location. The variance of the $\log_{10}$(CF) for all particles is 0.065. Figure 6-13 presents the relative frequency histogram of $\log_{10}$ canister flux for 120 starting positions. The histogram is normalised with respect to the total number of starting positions and is clearly skewed with a larger upper tail.

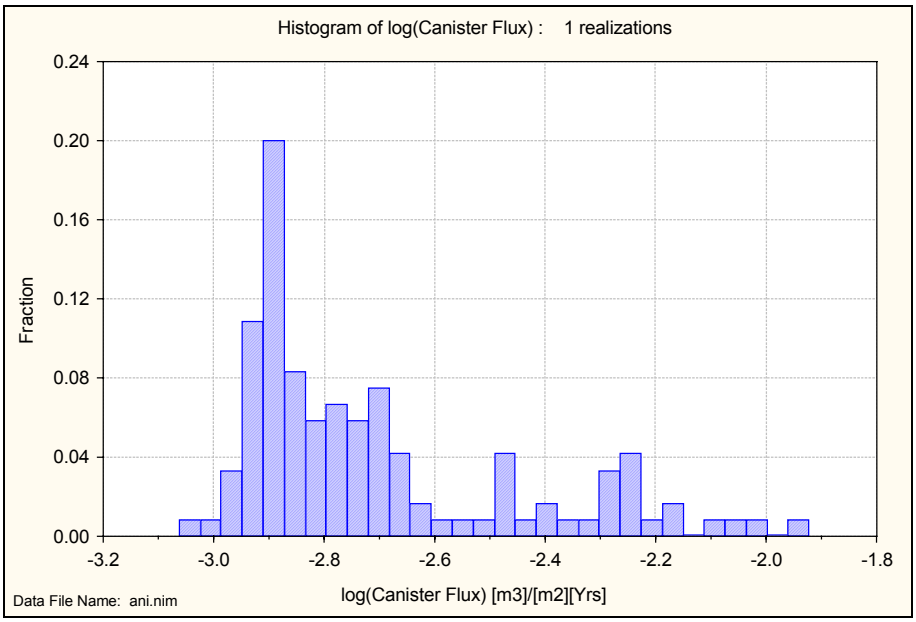

Figure 6-13 *Relative frequency histogram of log_{10} canister flux for the Anisotropic Case. The histogram is normalised with respect to the total number of starting positions. Results for 120 starting positions.*

Figure 6-14 presents the floating histogram of the log_{10} canister flux for 120 starting positions. The histogram is normalised with respect to the total number of starting positions.

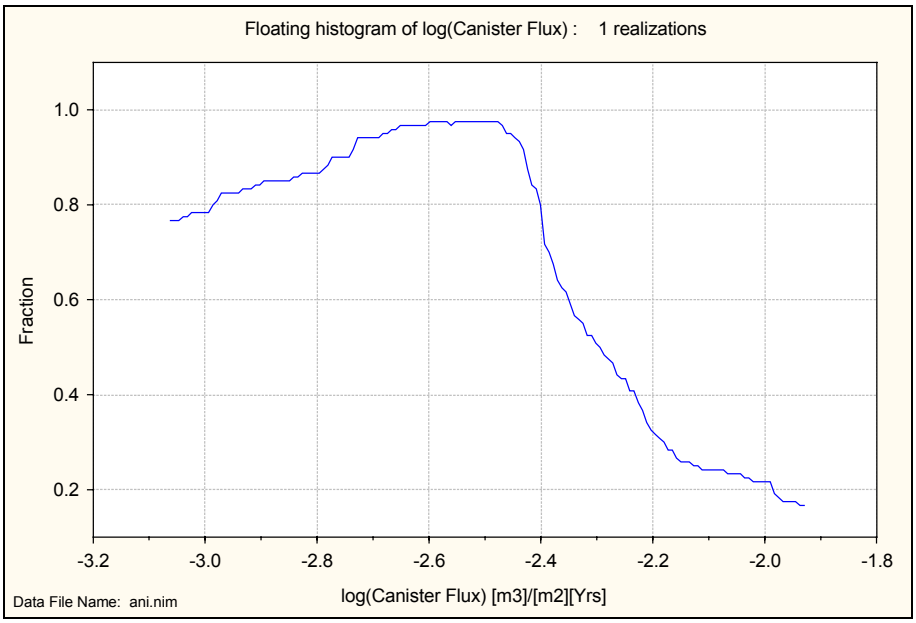

Figure 6-14 *Floating histogram of log_{10} canister flux for the Anisotropic Case. The histogram is normalised with respect to the total number of starting positions. Results for 120 starting positions.*

Figure 6-15 presents a box plot of $\log_{10}$ canister flux for 120 starting positions.

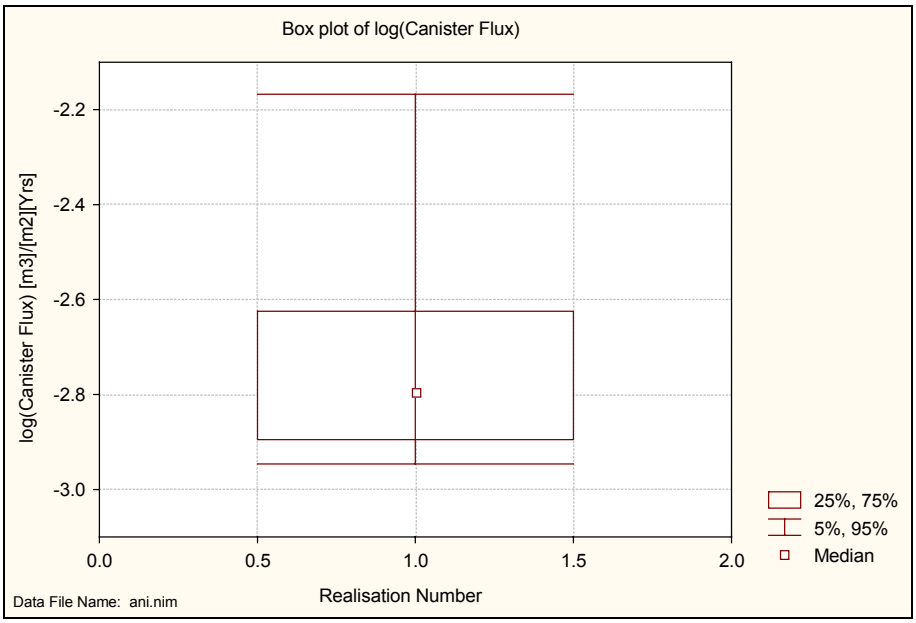

Figure 6-15 *Box plot of $\log_{10}$ canister flux showing the median and the 5th, 25th, 75th and 95th percentiles for the Anisotropic Case. Results for 120 starting positions.*

Figure 6-16 presents a scatter plot of $\log_{10}$ travel time versus $\log_{10}$ canister flux. The correlation between the $\log_{10}$ travel time and the $\log_{10}$ canister flux is not as clear here as for the Base Case even if some correlation can be seen.

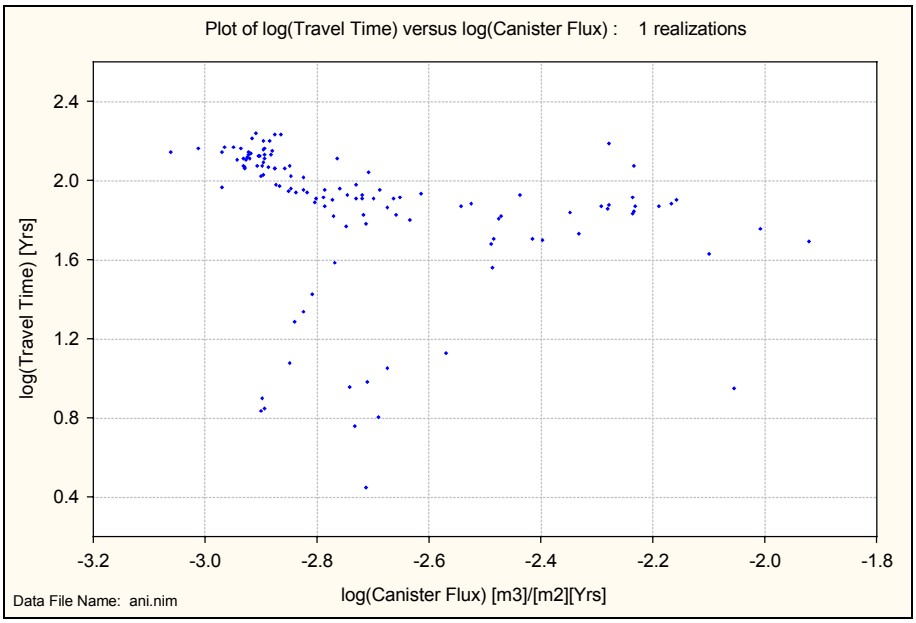

Figure 6-16 Scatter plot of $\log_{10}$ travel time versus $\log_{10}$ canister flux for the Anisotropic Case. Results for 120 starting positions.

7 Saline Case

The Saline Case uses boundary condition data (residual pressure and salt concentration) from the transient regional Beberg model including salt, *'grltrans62a.gfs'*, which takes into account the effects of the presence of salt in the groundwater. Unlike the boundary condition data used for the Base Case and the Anisotropy Case which were generated using a steady state freshwater model, the data for this variant was generated using a variable density field in the regional model. The data imported correspond to the present day situation at the Beberg site. The regional model *'grltrans62a.gfs'* was also used generating the environmental head boundary conditions used in the HYDRASTAR case, Variant 1.

In the Saline Case both the residual pressure and the salt concentration are interpolated to the site scale model from the regional NAMMU model. The pressure boundary conditions and the salt concentration in the entire model domain are held constant throughout the simulation. The variable solved for is the residual pressure, P^R. See section 3.5 for definitions.

The Saline Case uses the same permeability field as the Base Case, see section 3.2.1.

7.1 Boundary Conditions

Figure 7-1 shows the constant residual pressure (Dirichlet) boundary conditions on each face of the model domain for the Saline Case. The red colour indicates higher pressure and the blue colour indicates lower pressure. The northeast direction of the major hydraulic gradient in the region is apparent.

The Saline Case was not solved for the salt concentration but only for the residual pressure. Figure 7-2 shows the constant salt concentration on each face of the model domain for the Saline Case. The red colour indicates higher salt concentration and the blue colour indicates lower salt concentration. It is clear that the salt concentration is quite constant in the horizontal plane and increases with depth. Some effects of the fracture zones in the regional model can be seen along the boundaries where the salt has been flushed out from the fractures. Due to the lower resolution in the regional model, not all the fractures used in the site scale model of Beberg are represented in the regional model. Because of this, some inconsistencies appear in the salt concentration profile when applied to the site scale model. At places where there are fractures in the site scale model but not in the regional scale model, the salt profile will not have the proper shape. Note that the salt concentration imported from the regional model corresponds to the present day situation, which is the end result of the transient modelling performed. The future scenario in the region is that the salt water is being flushed out of the model due to fresh water infiltration. These effects have not been included in the scope of this report.

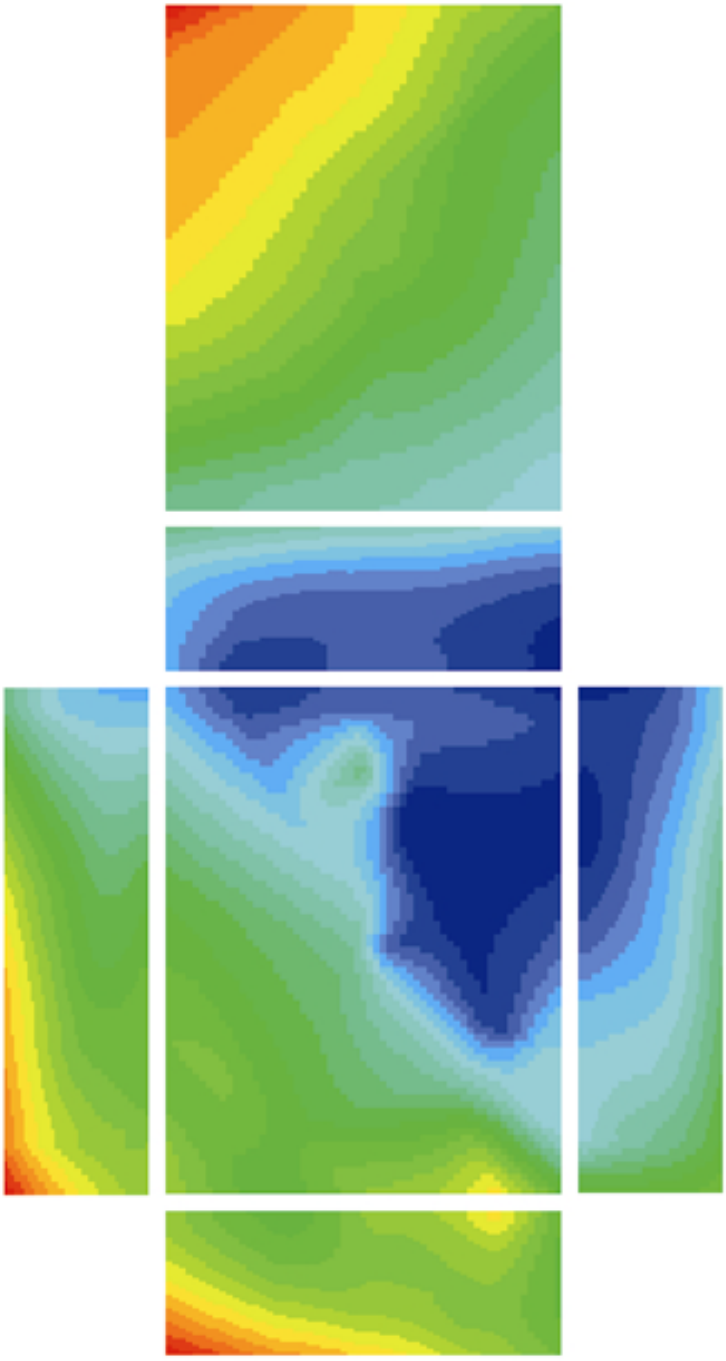

Figure 7-1 *The constant residual pressure (Dirichlet) boundary conditions on each face of the model domain for the Saline Case. The red colour indicates higher pressure and the blue colour indicates lower pressure.*

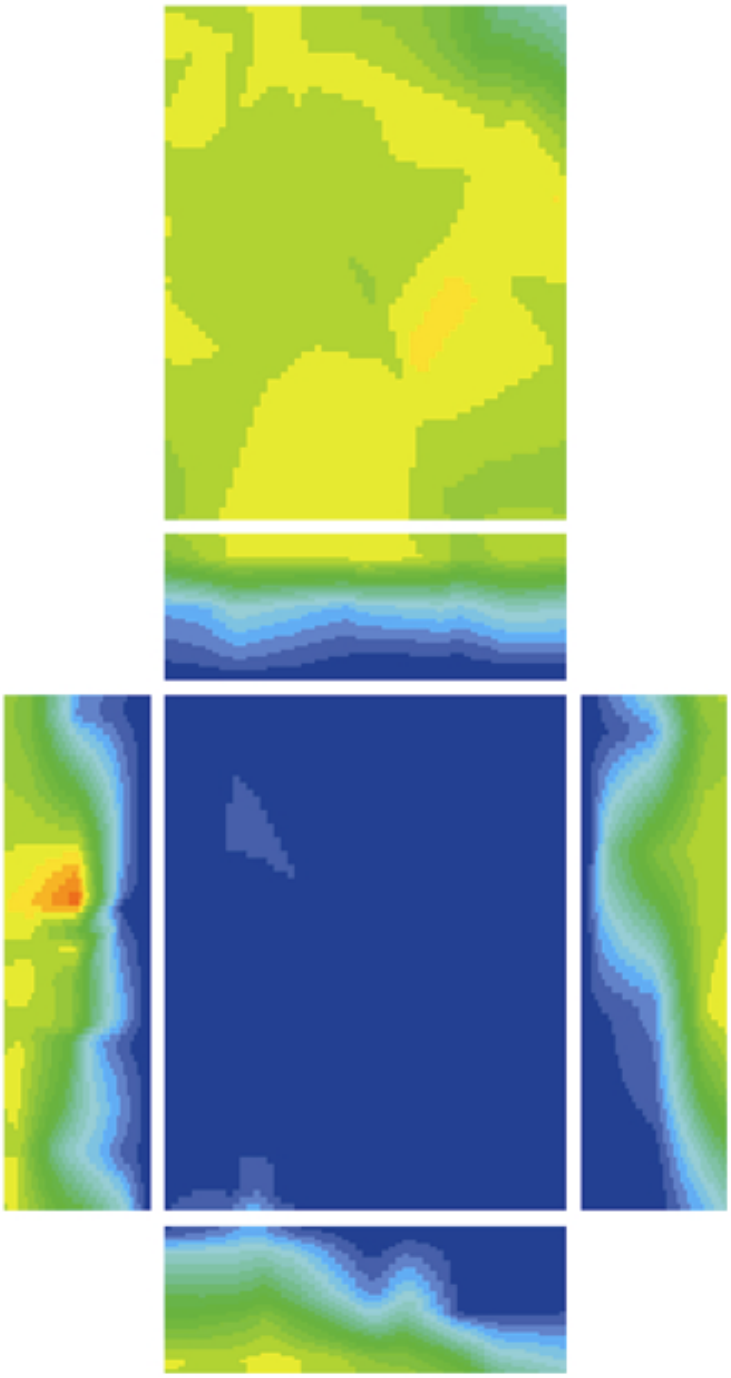

Figure 7-2 *The constant salt concentration on each face of the model domain for the Saline Case. The red colour indicates higher salt concentration and the blue colour indicates lower salt concentration.*

7.2 Results

Figure 7-3 and Figure 7-4 show the calculated residual pressure distribution on slices cutting through the model domain for the Saline Case. The view of the model is taken from the southeast for both figures. The red colour indicates higher pressure and the blue colour indicates lower pressure. The hydraulic head range from 16.6 m to 38.4 m. Due to the presence of salt, the maximum hydraulic head in the Saline Case is 5 m higher compared to the Base Case. Although the gradient of the residual pressure is pointing upwards through the model, the direction of the groundwater flow is downwards, see Figure 7-11. The reason for this can be found in the definitions of the flow equations in section 3.5.1. When there is salt present in the system, the differences in density can cause the direction of the flow to change, i.e. if $\left((\rho - \rho_0)g > \nabla P^R\right)$.

The northeast direction of the major hydraulic gradient in the region is apparent. The effects of permeability on the pressure distribution around the northern repository seen in the Base Case do not appear very clearly in this variant. The higher salt concentration at the bottom of the model changes the residual pressure distribution compared to the Base Case. The contours of the residual pressure are more horizontal in the Saline Case compared to the Base Case, see Figure 7-3.

In Figure 7-4 the effects of the Imundbo Zone appears in the residual pressure distribution where the pressure contours are aligned with the zone. Some minor effects caused by the variants in the salt distribution can also be seen in this figure.

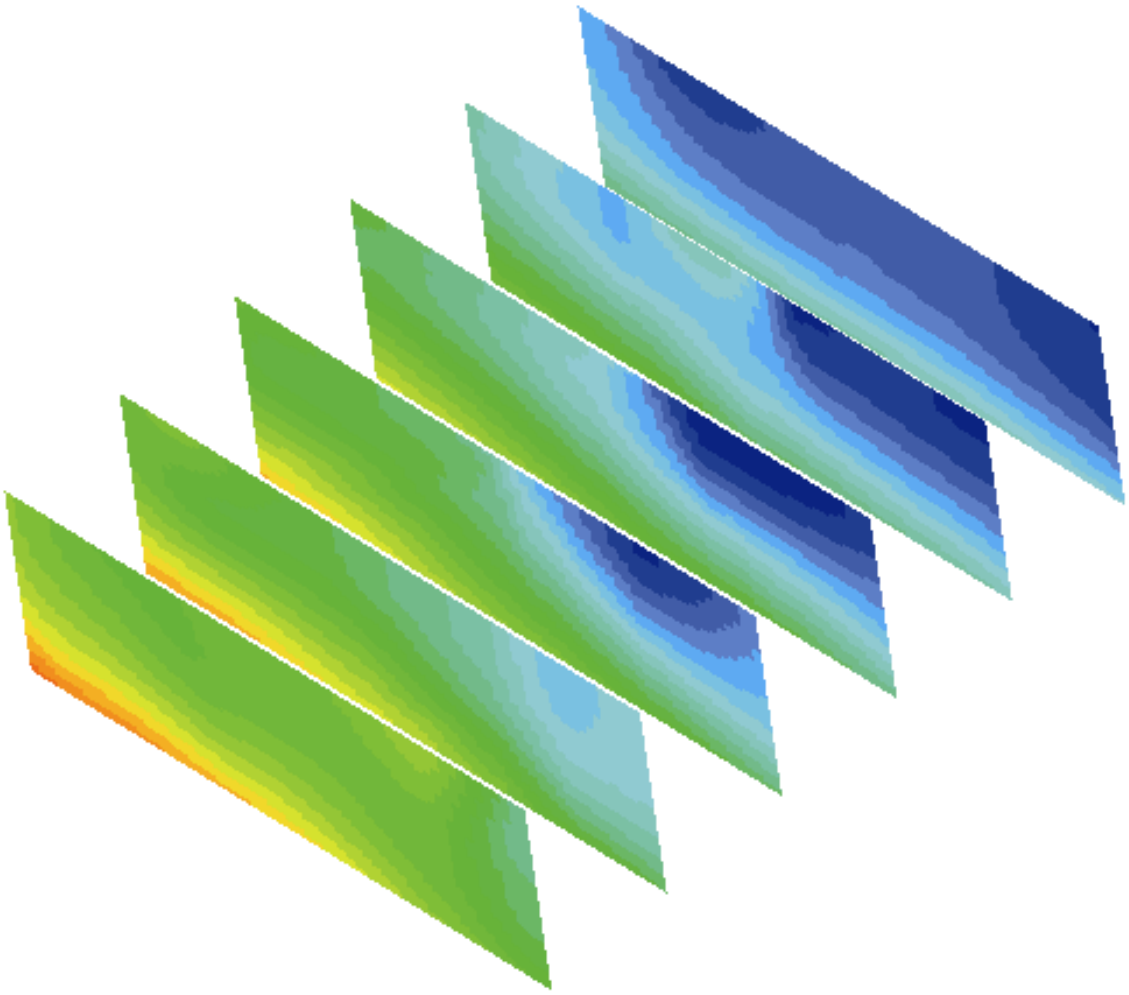

Figure 7-3 *The residual pressure distribution shown on six slices cutting through the model domain in the west-east direction for the Saline Case. The red colour indicates higher pressure and the blue colour indicates lower pressure. View from the southeast.*

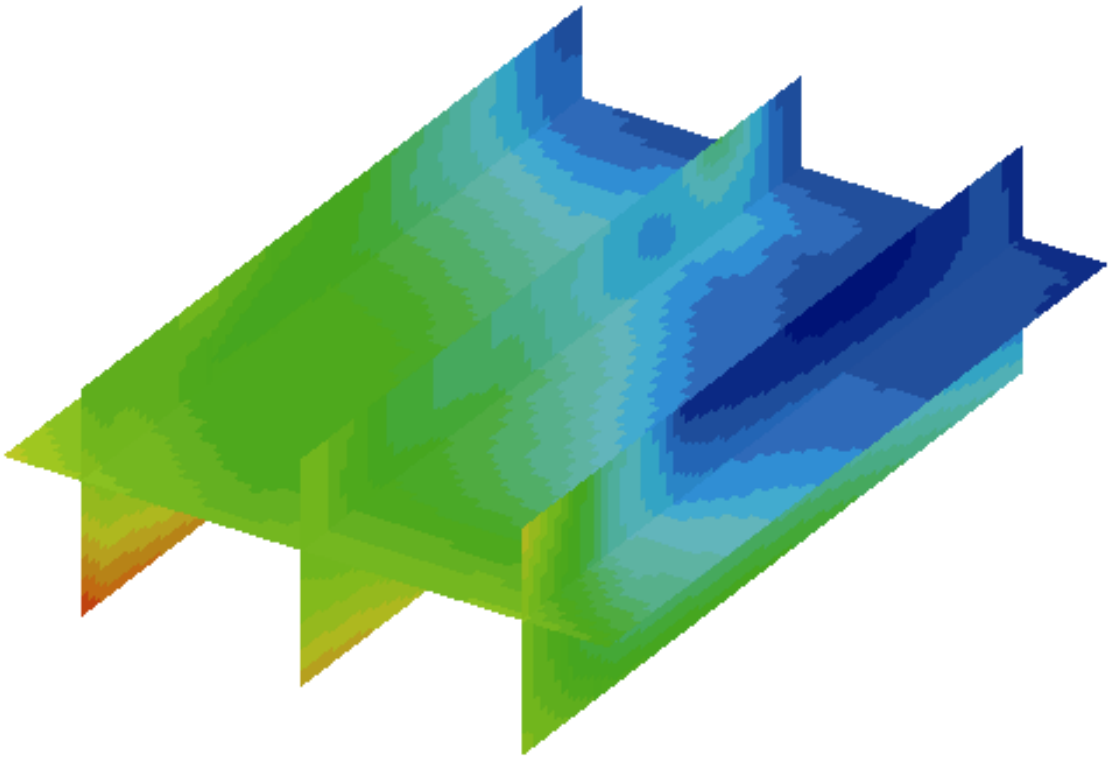

Figure 7-4 *The residual pressure distribution shown on four slices cutting through the model domain in the south-north direction for the Saline Case. The horizontal plane is placed at a depth of z = -604.5 m. The red colour indicates higher pressure and the blue colour indicates lower pressure. View from the southeast.*

Figure 7-5 and Figure 7-6 show the constant salt concentration distribution on slices cutting through the model domain for the Saline Case. The view of the model is taken from the southeast for both figures. Note that the salt distribution was imported from the regional model and not a result of the site scale modelling. The effect that the fractures in the regional model had on the salt distribution is clearly visible. The salt water was flushed out of the fractures by the infiltrating fresh water coming from the top surface.

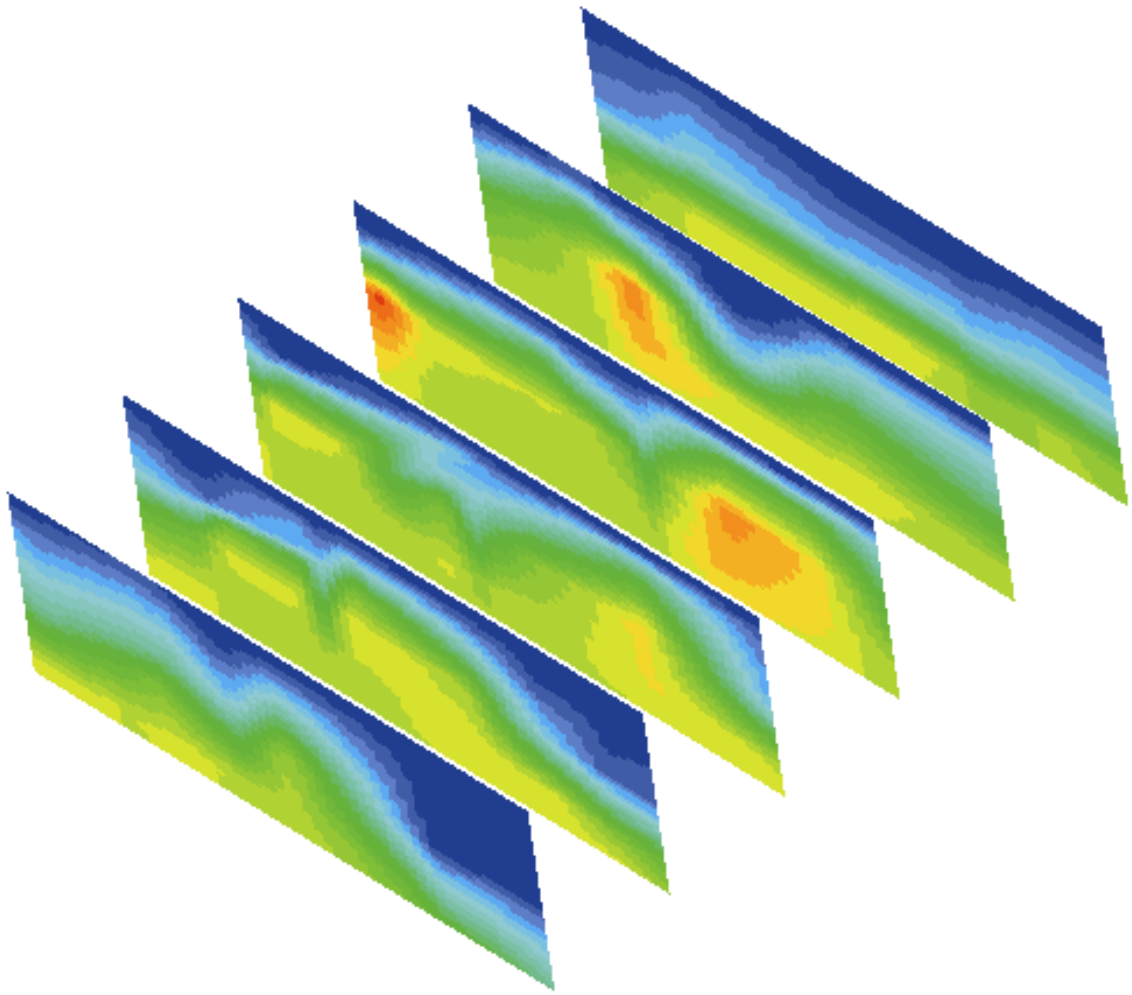

Figure 7-5 *The constant salt concentration distribution shown on six slices cutting through the model domain in the west-east direction for the Saline Case. The red colour indicates higher salt concentration and the blue colour indicates lower salt concentration. View from the southeast.*

In Figure 7-6 the fractures surrounding the northern repository can be seen together with the higher salt concentration underneath Zone 2.

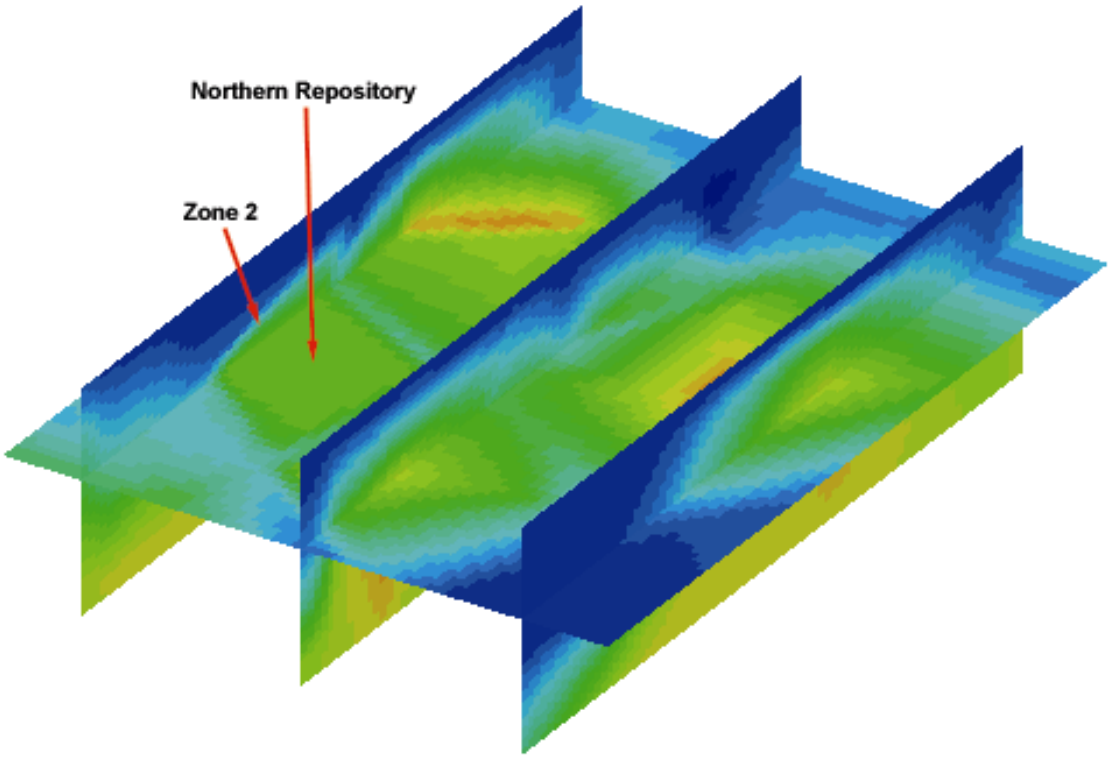

Figure 7-6 *The constant salt concentration distribution shown on four slices cutting through the model domain in the south-north direction for the Saline Case. The horizontal plane is placed at a depth of z = -604.5 m. The red colour indicates higher salt concentration and the blue colour indicates lower salt concentration. View from the southeast.*

Figure 7-7 and Figure 7-8 show the salt concentration profiles as iso surfaces together with permeability slices in the model domain. In this case, the iso surface visualises a constant salt concentration of $C = 0.3$ and $C = 0.8$ respectively. A salt concentration of $C = 1.0$ corresponds to a salinity of 0.8 % or a water density of 1006.29 kg/m^3. These values correspond to the concentrations that have been encountered at the Beberg site, see section 3.5.2 for definitions. The effect of fresh water infiltration displacing the saline groundwater in the fracture zones in the regional model clearly appears as deep valleys on the iso surfaces. The detected increase of salinity in the northern block underneath Zone 2 is also appearing and the surface follows the incline of the zone above. The squared pattern in some areas of the iso surface is a result of the model discretisation with the shape of the finite elements reflected onto the surface.

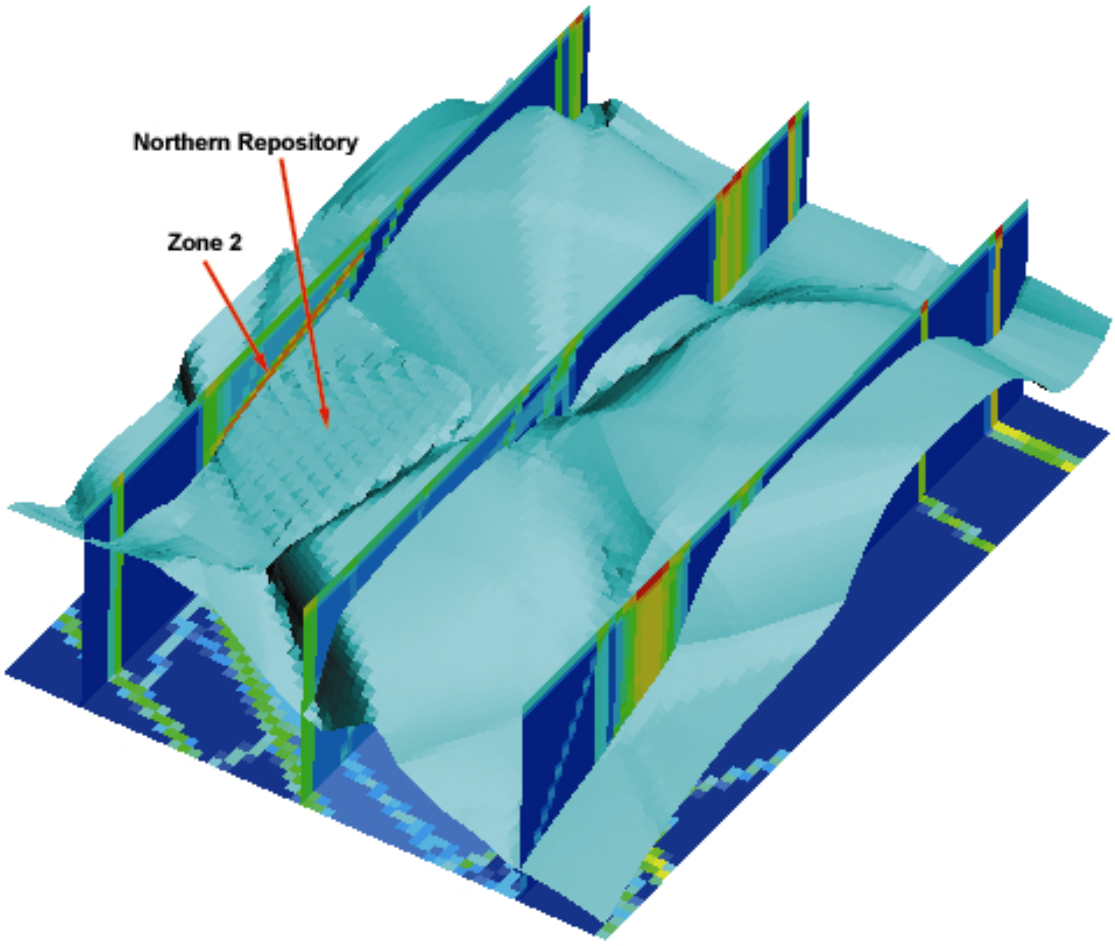

Figure 7-7 *The iso surface of salt concentration at C=0.3 shown together with four slices with the horizontal permeability field slices cutting through the model domain in the south-north direction for the Saline Case. View from the southeast.*

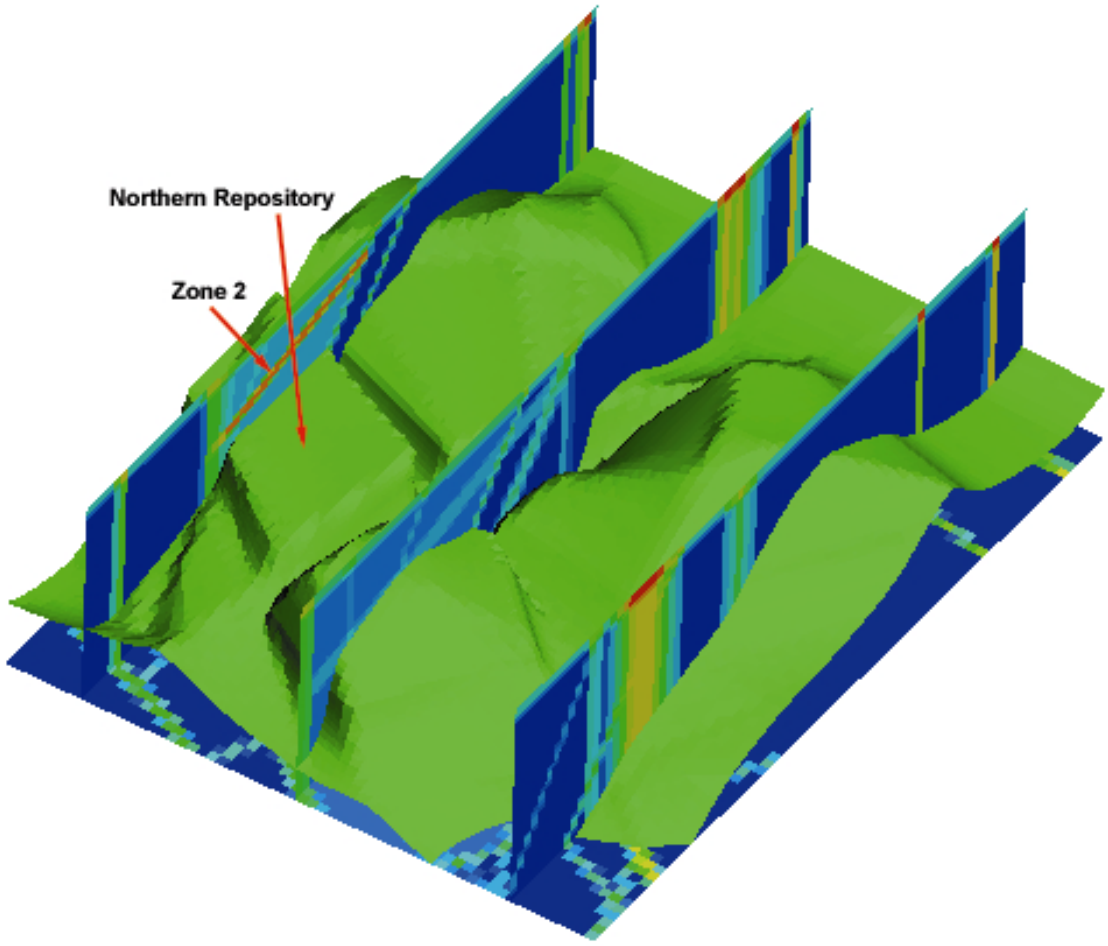

Figure 7-8 *The iso surface of salt concentration at C=0.8 shown together with four slices with the horizontal permeability field slices cutting through the model domain in the south-north direction for the Saline Case. View from the southeast.*

Figure 7-9 and Figure 7-10 show the salt concentration profiles as iso surfaces viewed from above the model domain. These iso surfaces are the same as the ones shown in Figure 7-7 and Figure 7-8.

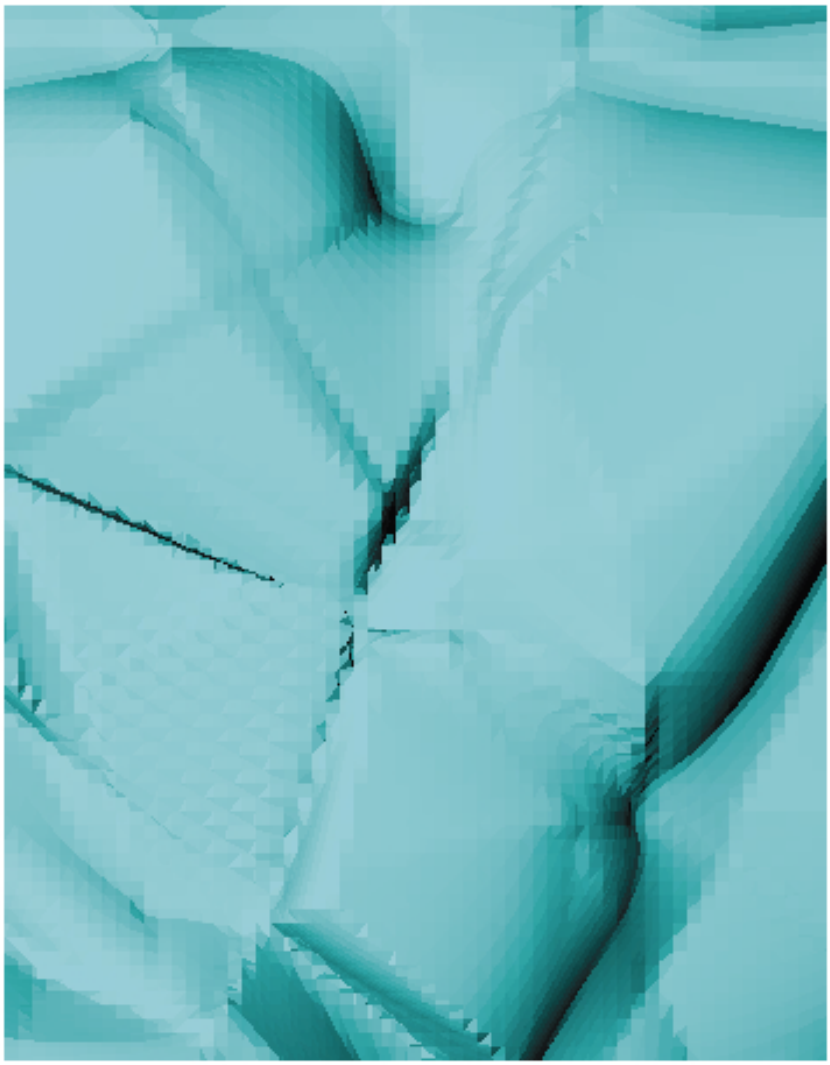

Figure 7-9 *The iso surface of salt concentration at C=0.3 for the Saline Case. View from the top.*

Figure 7-10 *The iso surface of salt concentration at C=0.8 for the Saline Case. View from the top.*

7.2.1 Exit Locations

A set of 120 particles were released at a depth of z = -604.5 m from the northern and the southern blocks (the area of the repository), 109 from the northern block and 11 from the southern block. Figure 7-11 shows the pathlines in three views calculated with NAMMU. The pathlines are coloured with respect to travel time. The exit locations, shown in Figure 7-11, are defined as the points where the released particles reach the boundary in the model domain.

The particles released in the Saline Case show a completely different pattern compared to the ones released in the Base Case and the Anisotropic Case. The presence of the dense saline groundwater is changing the flow field completely and sending the particles straight down through the model domain in an almost vertical direction. Hence, the major part of the particles exits through the bottom of the model. The exit locations are located around the major fracture zones near the northern repository, i.e. Zone 1, Zone 3, Zone 4, Zone 5 and Zone 6. A few pathlines find their way up to the Imundbo Zone where they exit through the bottom of the model domain. A couple of particles released from the northern repository are stuck in the middle of the model and never reach any boundary. The regional hydraulic gradient drives the particles in a northeast direction.

The particles started from the southern repository are initially sent down through the model, just as they were in the northern repository. The difference is that the major part of the particles released from the southern repository never reach the bottom of the model domain. Instead, they change direction dramatically when they reach the Imundbo Zone where they go straight up through the zone and exit through the top surface of the model domain. Just a few of the pathlines from the southern repository exit through the bottom of the model domain.

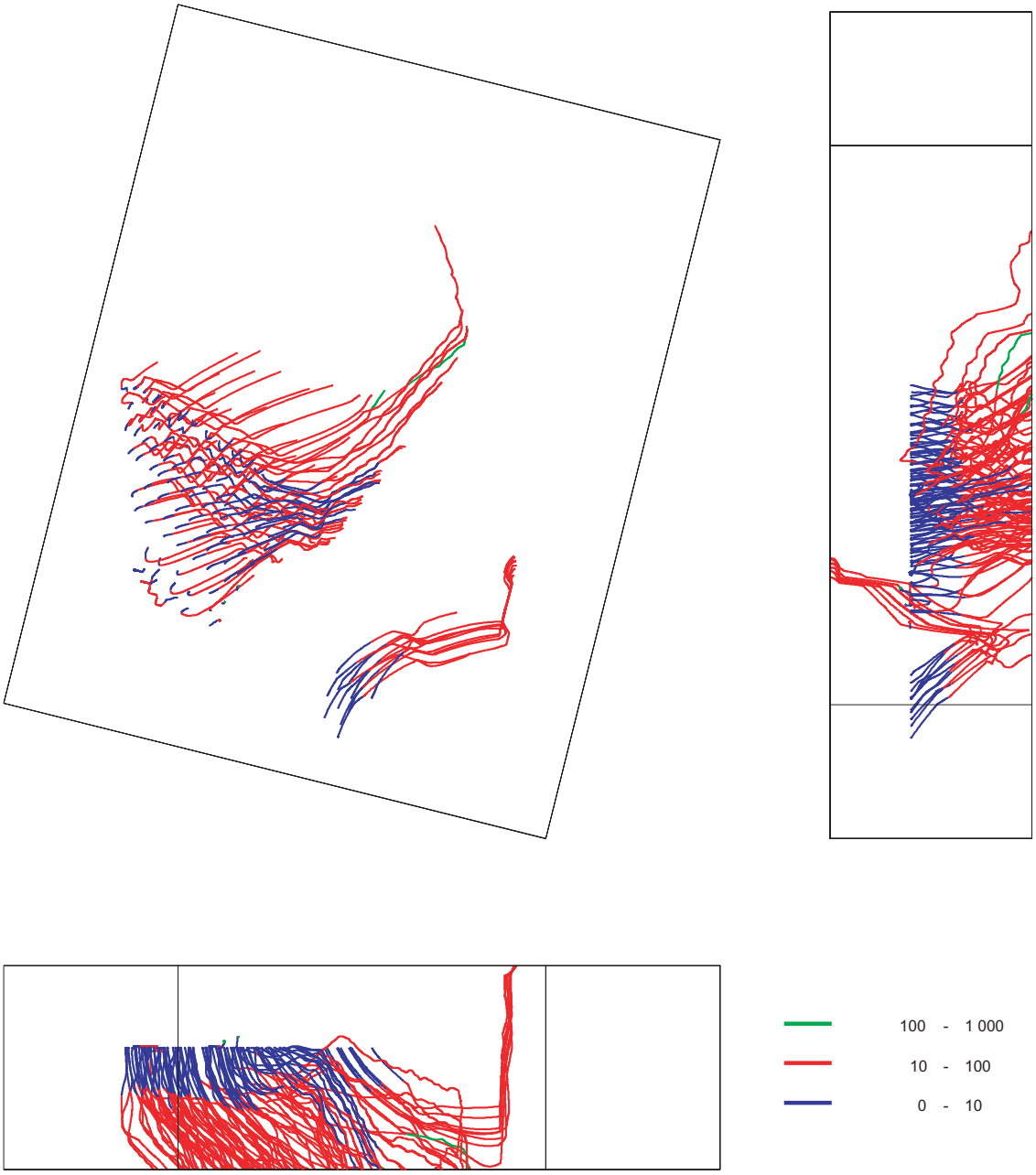

Figure 7-11 *Forward pathlines for the Saline Case. A set of 120 particles are released at a depth of z = -604.5 m, 109 from the northern block and 11 from the southern block. The pathlines are coloured with respect to travel time given in years. Upper left: Plan view of the model from above. Upper right: Elevation view from the east. Lower left: Elevation view from the south.*

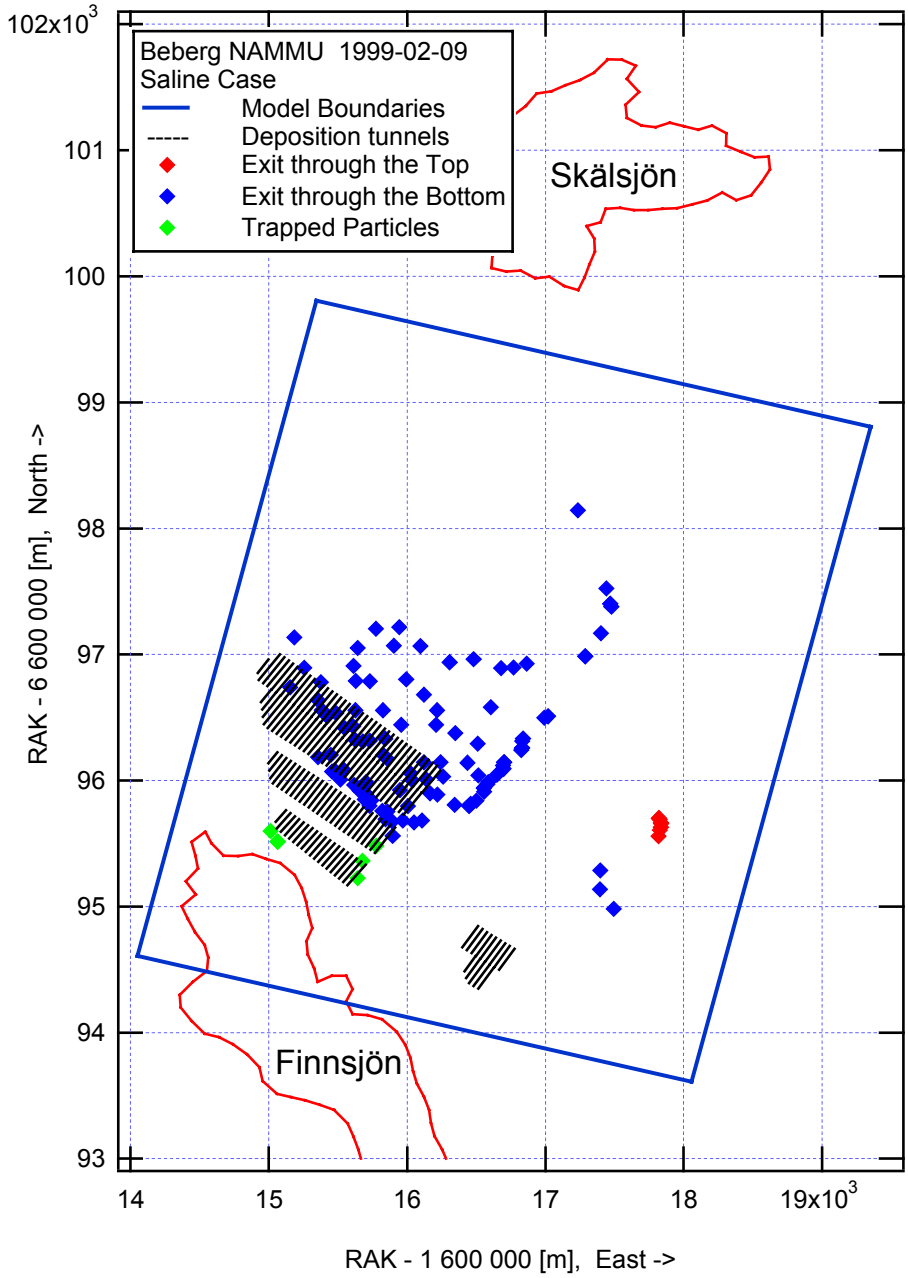

Figure 7-12 *Exit locations for the released particles in the Saline Case. The red markers show particles exiting the top of the model, the blue markers show particles exiting the bottom of the model and the green markers show particles that are stuck in the model and not reaching any of the model boundaries. View from the top of the model.*

7.2.2 Boundary Flow

Figure 7-13 shows the boundary flows for the Saline Case. The direction of the arrows denotes the direction of the net flow over the model surface. The size of the arrows has been altered to symbolise the magnitude of the flow. The actual size should only be regarded as an illustration and not as an exact measure. The direction of the boundary flows is in agreement with the regional flow pattern.

The flow pattern is quite similar to the Base Case except for the direction of the flow through the bottom surface of the model domain. In the Saline Case the flow through the bottom surface is directed out of the model and not into the model as was the situation for the Base Case. The size of the net flows, except for the bottom surface, is very similar to the ones in the Base Case.

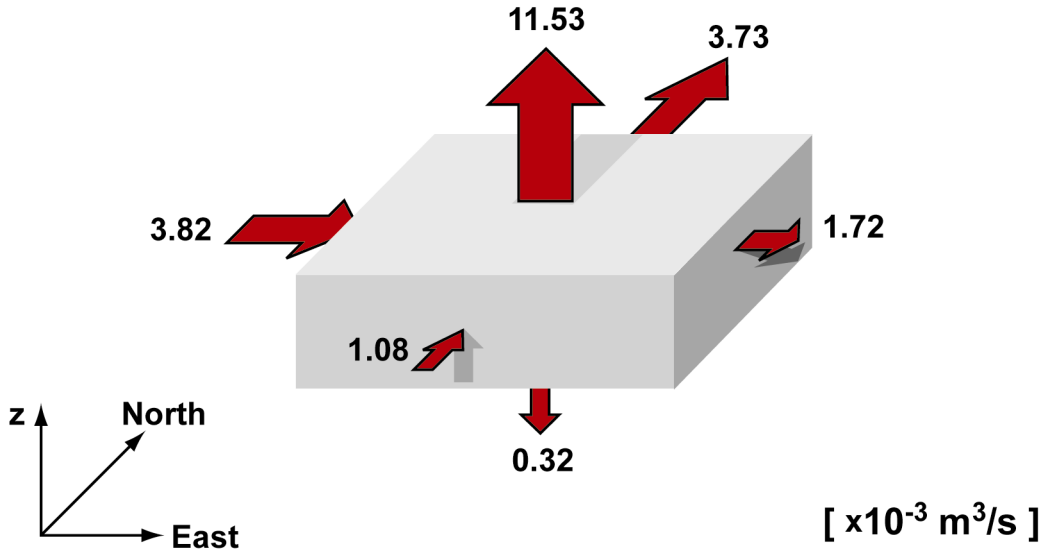

Figure 7-13 *Boundary flows for the Saline Case. Arrows show the direction of the regional flow through each of the boundary surfaces.*

Table 7-1 summarises the calculated groundwater boundary flows for the Saline Case. A positive boundary flow is directed out from the model domain. Although the directions of the flow coincide with the regional flow pattern, i.e. in the northeast direction, the calculated mass balance shows a large discrepancy. Looking at the net flows, the outflow from the model is about a factor 3.5 larger than the inflow to the model. As for the two previous variants, studying the gross flows for each surface of the model gives us an explanation to the discrepancy in the mass balance. In fact, the total residual from the mass balance is only about 15 % of the gross flows through the top boundary surface, which is also the predominating outflow area.

Table 7-1 Groundwater flow through the model boundaries for the Saline Case. Positive flow is directed out from the model.

Site Model Surface	Gross Inflow [$\cdot 10^{-3}$ m^3/s]	Gross Outflow [$\cdot 10^{-3}$ m^3/s]	Net Flow through Surface [$\cdot 10^{-3}$ m^3/s]
Top	-76.05	87.58	11.53
Bottom	-3.36	3.69	0.32
South	-1.14	0.06	-1.08
North	0.00	3.73	3.73
West	-3.91	0.09	-3.82
East	-1.39	3.11	1.72
Total Inflow	-85.85	-	-4.90
Total Outflow	-	98.25	17.30
Mass balance			***12.40***

7.3 Statistics

Table 7-2 shows the statistical summary of the 120 canister positions in the Saline Case. The calculated performance measures are the travel time (TT) and the canister flux (CF). The travel time is the time used by the particles released in the model to be transported by advection from the starting position to any boundary of the model domain. The canister flux is the Darcy groundwater velocity calculated by NAMMU as the resultant of the three velocity components (u_x, u_y and u_z) at each of the 120 stream tube starting positions.

All particles are released at a depth of -604.5 m. For the statistical calculations the particles were also grouped with respect to what boundary they exited through.

Table 7-2 Statistical summary for the Saline Case.

Statistics	$Log_{10}(TT_{tot})$	$Log_{10}(TT_{top})$	$Log_{10}(TT_{bottom})$	$Log_{10}(TT_{stuck})$	$Log_{10}(CF)$
Mean	1.583	1.704	1.573	1.587	-2.437
Median	1.609	1.709	1.562	1.403	-2.424
5th Percentile	1.049	1.601	1.064	0.975	-2.759
25th Percentile	1.424	1.686	1.428	1.190	-2.506
75th Percentile	1.737	1.714	1.734	2.121	-2.346
95th Percentile	1.989	1.812	1.980	2.312	-2.252
St Deviation	0.268	0.059	0.258	0.498	0.168
Variance	0.072	0.003	0.067	0.248	0.028
Min Value	0.933	1.601	0.933	0.975	-3.088
Max Value	2.311	1.812	2.146	2.311	-1.928
Fraction	1.000	0.067	0.875	0.058	1.000

7.3.1 Travel Time

Table 7-2 summarises the result for the travel time and indicates a median travel time of 51 years, with an interquartile range from 49 years to 52 years for the particles exiting the top of the model. The variance of the $\log_{10}$(TT) for the particles exiting through the top is 0.003 and the 5th percentile is 40 years. Only 6.7 % of the released particles are exiting through the top of the model, the major part of the particles, 87.5 %, exit through the bottom of model and 5.8 % of the particles are stuck in the model. Since only a small fraction of the released particles reach the top boundary of the model the statistical summary for the Saline Case should be read with caution. The median travel time for the particles exiting through the bottom is 36 years, with an interquartile range from 27 years to 54 years. The variance of the $\log_{10}$(TT) for the particles exiting through the bottom of the model is 0.067 and the 5th percentile is 12 years. Figure 7-14 presents the relative frequency histogram of $\log_{10}$ travel time for 120 starting positions. The histogram is normalised with respect to the total number of starting positions and is

quite uniformly distributed around the median travel time, this is also shown in Figure 7-15.

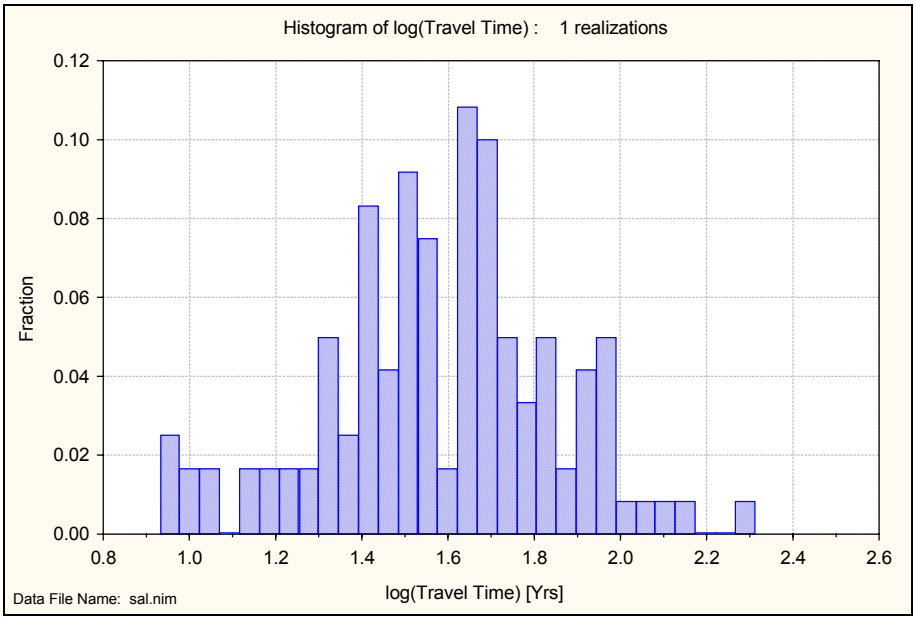

Figure 7-14 *Relative frequency histogram of $\log_{10}$ travel time for the Saline Case. The histogram is normalised with respect to the total number of starting positions. Results for 120 starting positions.*

Figure 7-15 presents the floating histogram of $\log_{10}$ travel time for 120 starting positions. The histogram is normalised with respect to the total number of starting positions.

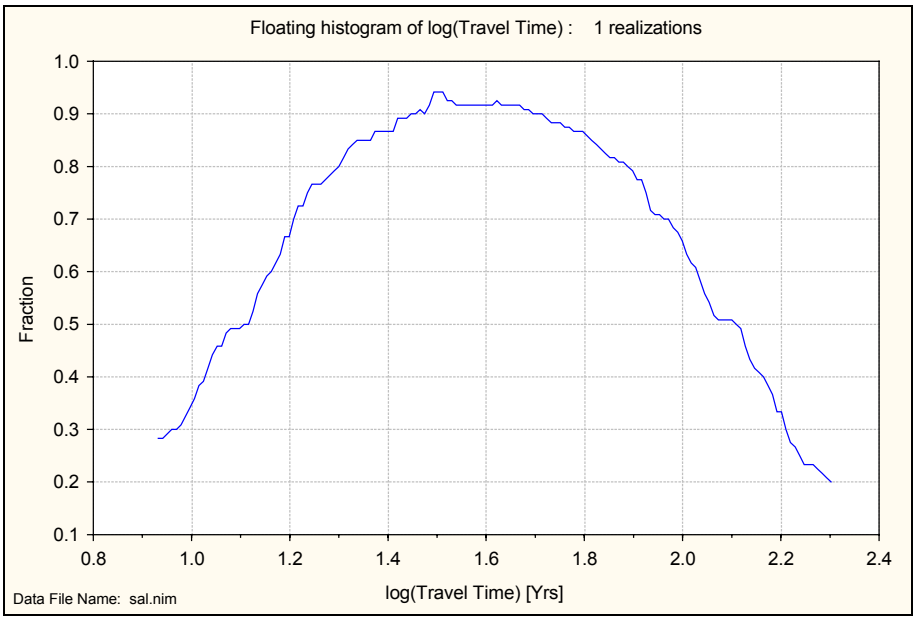

Figure 7-15 *Floating histogram of log_{10} travel time for the Saline Case. The histogram is normalised with respect to the total number of starting positions. Results for 120 starting positions.*

Figure 7-16 presents a box plot of log_{10} travel time for 120 starting positions.

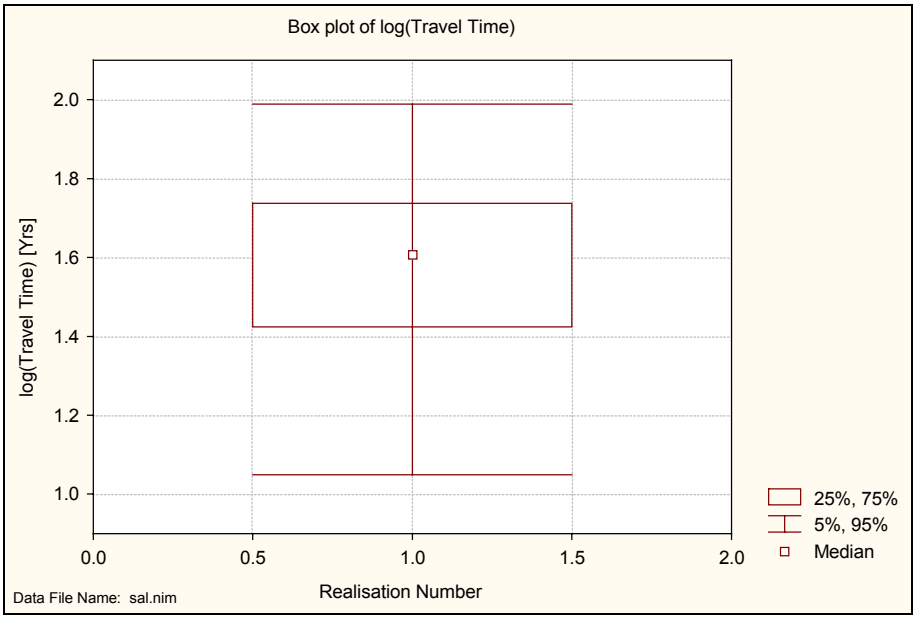

Figure 7-16 *Box plot of log_{10} travel time showing the median and the 5^{th}, 25^{th}, 75^{th} and 95^{th} percentiles for the Saline Case. Results for 120 starting positions.*

7.3.2 Canister Flux

Table 7-2 summarises the result for the canister flux and indicates a median canister flux of $3.8 \cdot 10^{-3}$ m/year, with an interquartile range from $3.1 \cdot 10^{-3}$ m/year to $4.5 \cdot 10^{-3}$ m/year. When calculating the canister flux the particles are not divided into subgroups since the canister flux is measured at the starting position and therefore independent of exit location. The variance of the $\log_{10}$(CF) for all particles is 0.028. Figure 7-17 presents the relative frequency histogram of $\log_{10}$ canister flux for 120 starting positions. The histogram is normalised with respect to the total number of starting positions and is slightly skewed with a larger lower tail.

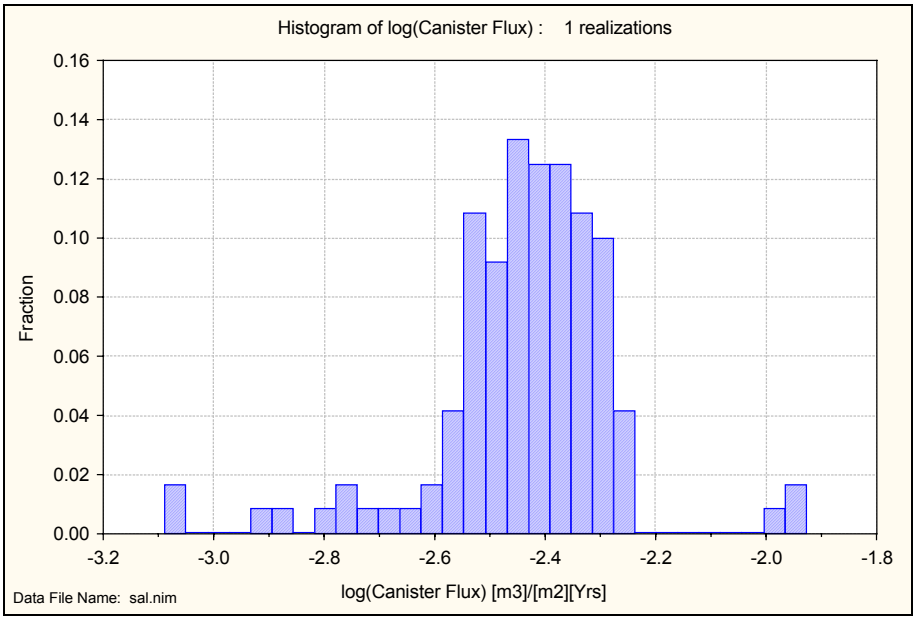

Figure 7-17 *Relative frequency histogram of $\log_{10}$ canister flux for the Saline Case. The histogram is normalised with respect to the total number of starting positions. Results for 120 starting positions.*

Figure 7-18 presents the floating histogram of $\log_{10}$ canister flux for 120 starting positions. The histogram is normalised with respect to the total number of starting positions.

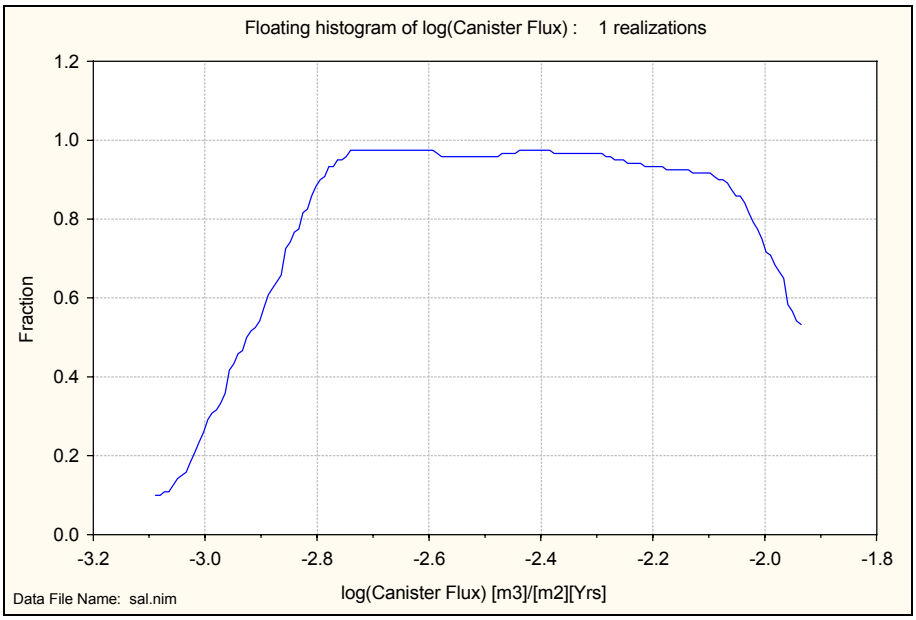

Figure 7-18 *Floating histogram of log_{10} canister flux for the Saline Case. The histogram is normalised with respect to the total number of starting positions. Results for 120 starting positions.*

Figure 7-19 presents a box plot of log_{10} canister flux for 120 starting positions.

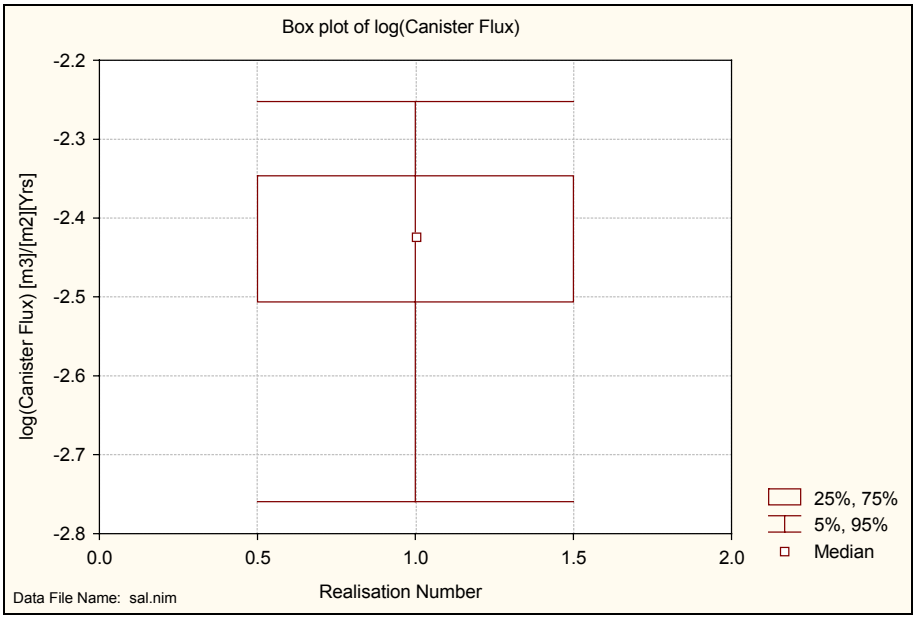

Figure 7-19 *Box plot of log_{10} canister flux showing the median and the 5^{th}, 25^{th}, 75^{th} and 95^{th} percentiles for the Saline Case. Results for 120 starting positions.*

Figure 7-20 presents a scatter plot of $\log_{10}$ travel time versus $\log_{10}$ canister flux. No correlation between the $\log_{10}$ travel time and the $\log_{10}$ canister flux can be seen for the Saline Case.

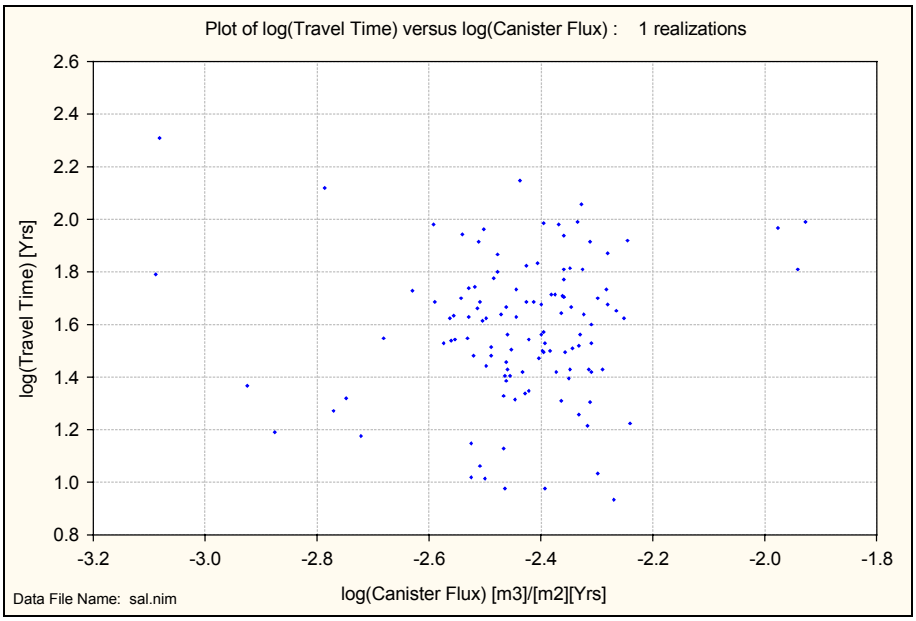

Figure 7-20 Scatter plot of $\log_{10}$ travel time versus $\log_{10}$ canister flux for the Saline Case. Results for 120 starting positions.

8 Discussion

The main objectives of this study have been to:

1. Perform a comparison between the results from NAMMU and HYDRASTAR for a deterministic case without any effects from anisotropy or salt. These variants are called the Base Case and the BaseFine Case respectively.

2. Study the effect of anisotropy on the groundwater flow pattern in the model set up for the Base Case. This variant is called the Anisotropic Case.

3. Study the effect of the presence of a variable density field pattern in the model set up for the Base Case. This variant is called the Saline Case.

In addition to this, the tools used for modelling and visualisation were evaluated.

The Base Case, the BaseFine Case and the Saline Case have corresponding HYDRASTAR models with which they will be compared in the discussion. The Anisotropic Case on the other hand does not have a corresponding HYDRASTAR model to be compared with and will therefore only be discussed together with the two NAMMU models.

8.1 Comparison between the Variants

8.1.1 The Base Case and the BaseFine Case

There are two major differences in the definitions of the Base Case and the BaseFine Case:

First, the BaseFine Case uses the same discretisation as the HYDRASTAR model while the discretisation in the Base Case was reduced a factor two in the x and y directions. This means that the permeability values had to be averaged when calculating the permeability field for the Base Case in order to translate the permeability values exported from HYDRASTAR, see section 3.2.1. Second, the BaseFine Case uses the same permeability values that were used by the HYDRASTAR model while the Base Case (as well as the remaining variants) uses the values that were generated for visualisation in AVS.

The residual pressure boundary conditions are the same for the Base Case and the BaseFine Case. The results for the two variants are quite similar, the pathlines are predominantly directed to the northeast through the rock mass away from the repository. However, the pattern of the pathlines for the BaseFine Case differs from the Base Case in a couple of ways. First, the pattern for the BaseFine Case is tighter. In the Base Case a lot of the pathlines went through the rock mass far north in the model. In the BaseFine Case the pathlines are more affected by Zone 5 and the Imundbo Zone and never reach as far north as in the Base Case. This gives a more concentrated pathline field. The variance of the $\log_{10}$(TT) for the BaseFine Case is 0.206 compared to 0.227 for the Base Case which reflects the different patterns. Another difference between the variants is that the pathlines are more horizontal in the BaseFine Case while the

pathlines go deeper in the Base Case and even exit through the bottom of the model a couple of times which never happens in the BaseFine Case. The reason why the pathlines are more horizontal and not so deep in the BaseFine Case compared to the Base Case is probably the different representation of the permeability field. The methods used calculating the permeability field for the Base Case overestimates the vertical permeability, which results in deeper pathlines. Compared to the Base Case, the pathline pattern for the BaseFine Case is in better agreement with the results from HYDRASTAR. In both variants the major part of the released particles exits within the Imundbo Zone and a smaller group exits in Zone 1. The permeable Zone 2 is an important feature in both variants. In both variants, a group of particles follows Zone 2 upward in a northeast direction until they reach the discharge areas in Zones 1, 3 and 4. These particles are the ones with the shortest travel times in these variants. The median travel time was 56 years for the Base Case and 67 years for the BaseFine Case, see Table 8-1. The median canister flux was $1.8 \cdot 10^{-3}$ m/year for the Base Case and $2.0 \cdot 10^{-3}$ m/year for the BaseFine Case, see Table 8-2.

8.1.2 The Anisotropic Case and the Saline Case

The effect of anisotropy and saline groundwater is found considerable on the pathlines. The presence of anisotropic hydraulic permeability drives the pathlines in the direction of the major axis of the anisotropy, which was set to N 45 W. The effect of the fracture zones is hereby enhanced in those cases the fractures are aligned parallel to the major axis of anisotropy. The predominating direction of flow is to the northeast for both variants. This is also the direction of the major regional hydraulic gradient. The pathlines in the Anisotropic Case do not go as deep down into the model as in the Base Case. This is probably a result of the properties of the anisotropy applied to the permeability field. A degree of anisotropy in the horizontal permeability of 10:1:1 was used which should give an enhanced groundwater flow horizontally in the northwest direction while the vertical flow should be relatively decreased at the same time. This influence on the groundwater flow pattern clearly appears in Figure 6-7 where the pathlines are located to the larger fracture zones aligned with the major anisotropic axis. Like for the Base Case, the predominating discharge area for the Anisotropic Case is through the Imundbo Zone. The travel times are somewhat longer in the Anisotropic Case, 85 years for the median travel time, compared to 56 years for the Base Case. The pathlines for the Anisotropic Case also show a smaller variance and a greater recovery fraction than for the Base Case.

In the Saline Case the flow pattern changes even more dramatically. The presence of salt in the groundwater is driving the flow downward, forcing the major part of the particles to exit through the bottom of the model domain. It is therefore not possible to predict the discharge areas in the Saline Case. Only a very small fraction of the released particles exits through the top surface of the model. Consequently, the basis for the statistical analysis is significantly reduced and a lot of caution should be taken comparing the statistical summary for the Saline Case to the other variants. The median travel time for the particles exiting through the top of the model in the Saline Case is 51 years. This is roughly the same as for the Base Case but one should bear in mind that the groundwater flow shows an entirely different pattern in the two variants so the calculated travel time is not reflecting the actual situation in the Saline Case.

The median travel time used by the particles to reach the bottom surface of the model is 36 years for the Saline Case. It is not possible to estimate the time these perticles exiting through the bottom of the model need to finally reach the top surface. Even so, it is evident that the presence of salt is contributing to the safety of the repository by considerably prolonging the pathways and the travel times. This was also showed in the regional modelling of the Beberg site *[Hartley et al., 1998]*.

Table 8-1 and Table 8-2 show the statistical summaries of the 120 canister positions for all variants. The calculated performance measures are travel time and canister flux. The travel time is the time used by the particles released in the model to be transported by advection from the starting position to any boundary of the model domain. All particles are released at a depth of -604.5 m. The canister flux is the magnitude of Darcy groundwater velocity. In NAMMU the resultant of the three velocity components (u_x, u_y and u_z) is calculated at each of the 120 stream tube starting positions.

Table 8-1 Statistical summary of the $\log_{10}$(Travel Time) for the pathlines exiting through the top of the model domain for all variants.

Statistics	Base Case	BaseFine Case	Anisotropic Case	Saline Case
Median	1.751	1.828	1.930	1.709
25th Percentile	1.396	1.510	1.821	1.686
75th Percentile	2.009	1.958	2.099	1.714
Variance	0.227	0.206	0.136	0.003
Fraction	0.858	0.917	1.000	0.067

Table 8-2 Statistical summary of the $\log_{10}$(Canister Flux) for all variants.

Statistics	Base Case	BaseFine Case	Anisotropic Case	Saline Case
Median	-2.754	-2.706	-2.795	-2.424
25th Percentile	-2.855	-2.837	-2.895	-2.506
75th Percentile	-2.587	-2.503	-2.624	-2.346
Variance	0.036	0.136	0.065	0.028
Fraction	1.000	1.000	1.000	1.000

Table 8-3 summarises the calculated net boundary groundwater flows for all variants. The four variants all show a large discrepancy in the calculated mass balance. This is ascribed the inaccurate method used for calculating the boundary fluxes, see section 3.5.3.

Another result worth noting is the large net outflow through the top surfaces for all four variants. This also is an effect of the integration routine used. However, compared to the gross flows over the boundary surfaces these net flows are rather small, in the order of 10-15 %. This indicates that the boundary flows, in particular those through the top surface of the model, in reality show a complicated pattern with both large inflows and

outflows. There are both recharge areas (in the southeast and in the southwest of the model domain) and discharge areas (in the northeast of the model domain) at the top surface of the model. This means that the calculated net flow is not a good measure to describe the flow pattern at the surfaces of the model domain.

A look at Table 8-3 reveals that the major direction of groundwater flow for all variants is to the northeast. The south and the west boundaries are net inflow surfaces in all variants while the north boundary is a net outflow surface in all variants. However, the results also show that there are differences between the variants. The bottom surface has a net inflow for the Base Case and the BaseFine Case while the Anisotropic Case and the Saline Case have a net outflow through the same surface. In the Saline Case this is expected since the major part of the released particles exit through the bottom as a result of the dense saline water. A look at Table 6-1 and Table 7-1 shows that even if the net outflow through the bottom surface in the Anisotropic Case is somewhat larger than for the Saline Case, the gross outflow in the Saline Case is more than twice the size of the gross outflow in the Anisotropic Case. This better corresponds with the pathline pattern where there was a striking difference between the two variants.

Table 8-3 **Summary of groundwater net flow through the model boundaries for all variants. Positive flow is directed out from the model.**

	Net Flow through Surface [$\cdot 10^{-3}$ m^3/s]			
Site Model Surface	**Base Case**	**BaseFine Case**	**Anisotropic Case**	**Saline Case**
Top	15.50	17.78	11.95	11.53
Bottom	-3.33	-2.68	0.75	0.32
South	-1.20	-1.96	-2.06	-1.08
North	3.72	6.19	7.03	3.73
West	-4.04	-8.50	-10.58	-3.82
East	1.07	2.24	-0.09	1.72
Total Inflow	-8.57	-13.14	-12.73	-4.90
Total Outflow	20.29	26.21	19.73	17.30
Mass balance	***11.72***	***13.07***	***7.00***	***12.40***

8.2 Comparison with HYDRASTAR

8.2.1 Comparison between the BaseFine Case and Variant 4 in HYDRASTAR

The BaseFine Case in this study corresponds to Variant 4 in the HYDRASTAR site scale model for Beberg. Variant 4 is a single realisation deterministic case that forms the base for the input data used in this study. Unfortunately, there is also a variant called Base Case in the HYDRASTAR model but this is a stochastic model and should not be compared to the Base Case in this study. Therefore when referring to the Base Case in the discussion the NAMMU model is considered.

The results from Variant 4 show great resemblance to the BaseFine Case. The discharge areas are found around the regional fracture zones situated northeast of the repository. The major part of the released particles exit within the Imundbo Zone. This is also where we find the pathlines with the longest travel times. The predominant direction of the pathlines is to the northeast through the rock mass. A major part of these particles tends to follow Zone 1 until they reach the intersection with the Imundbo Zone where they discharge. Compared to the Base Case the pathlines in Variant 4 and the BaseFine Case are grouped closer together on their way to the Imundbo Zone and do not reach as far north as the ones in the Base Case.

The particles released from the southern repository in the BaseFine Case and Variant 4 follow the same way through the rock mass and exit through the top surface in the same place in the Imundbo Zone. In both variants, the pathlines are more horizontal compared to the Base Case, where the pathlines go deeper into the model.

Table 8-4 shows the statistical summary for the BaseFine Case and Variant 4. The median travel time is 27 years in Variant 4 and 67 years in the BaseFine Case, i.e. a factor 2.5 longer travel times in the BaseFine Case. Comparing the canister flux for the two variants, we see that the difference is negligible. The median canister flux is $1.9 \cdot 10^{-3}$ - $2.0 \cdot 10^{-3}$ m^3/m^2,year. The variance for the $\log_{10}(TT)$ is twice as high for the BaseFine Case compared to Variant 4, while the variance of the $\log_{10}(CF)$ is somewhat closer, see Table 8-4.

Table 8-4 Statistical summary for the BaseFine Case and Variant 4.

	BaseFine Case		Variant 4	
Statistics	**$Log_{10}(TT_{top})$**	**$Log_{10}(CF)$**	**$Log_{10}(TT_{top})$**	**$Log_{10}(CF)$**
Median	1.828	-2.706	1.433	-2.732
25th Percentile	1.510	-2.837	1.230	-2.817
75th Percentile	1.958	-2.503	1.631	-2.529
Variance	0.206	0.136	0.108	0.162
Fraction	0.917	1.000	1.000	1.000

The discrepancies between the NAMMU results (BaseFine Case) and the HYDRASTAR (Variant 4) simulations can be ascribed to the different numerical discretisation (the different representation of the permeability, see Figure A - 1), and the different pathline algorithms used in the two models. For the median canister flux, the difference between the models is much smaller than the variance of the canister flux. For the median travel time, the difference between the models is quite big. This is expected though, since the calculation of pathlines is more sensitive to the variations in a heterogeneous permeability field. Comparing the two models, it should be noted that the pathway patterns are identical. See section A 1 for a short numerical analysis of the discrepancies between the models.

Table 8-5 summarises the net flows through the model boundaries for the BaseFine Case, the regional model and Variant 4. The regional model is the AltK case, here with freshwater, that was used for generating the boundary conditions for the site scale models in NAMMU and HYDRASTAR. The two NAMMU models, the BaseFine Case and the regional model, both show a discrepancy in the calculated mass balance. As explained above, this is caused by the inaccurate integrating method used. In reality, the mass balance over the model is within the range of the numerical errors, i.e. approximately 10^{-8}. HYDRASTAR on the other hand uses a proper algorithm and the calculated mass balance shows just a minor residual.

As can be seen in Table 8-5 considering the calculated flows, the BaseFine Case shows greater resemblance to Variant 4 than to the regional model. This is not surprising since the regional model has a totally different structure regarding both elements and fractures. This of course has great impact on the flows, in particular on the top boundary. Comparing the BaseFine Case to Variant 4 tells us that the direction of the net flow is the same for all boundaries although the sizes of the flows differ.

Table 8-5 Summary of groundwater net flow through the model boundaries for the BaseFine Case, the Regional Model and Variant 4. Positive flow is directed out from the model.

	Net Flow through Surface [$\cdot 10^{-3}$ m^3/s]		
Site Model Surface	**BaseFine Case**	**Regional Model**	**Variant 4**
Top	17.78	-1.86	13.66
Bottom	-2.68	-0.14	-7.65
South	-1.96	-2.41	-2.27
North	6.19	3.83	5.30
West	-8.50	-6.95	-9.93
East	2.24	4.05	0.92
Total Inflow	-13.14	-11.36	-19.85
Total Outflow	26.21	7.88	19.88
Mass balance	***13.07***	***-3.48***	***0.03***

8.2.2 Comparison between the Saline Case and Variant 1 in HYDRASTAR

The Saline Case in this study corresponds to Variant 1 in the HYDRASTAR local scale model for Beberg. Variant 1 is a stochastic simulation with 100 realisations using the environmental head as boundary conditions calculated from the regional AltK case with saline groundwater. The environmental head is used as an attempt to invoke some of the effects salinity has on the groundwater flow pattern. Since HYDRASTAR does not have the facility to model density dependent groundwater flow, this is one way of considering the effects of salt. Because of the fact that Variant 1 is a stochastic simulation we do not expect the results to be in perfect agreement.

The results from Variant 1 show great resemblance to the Saline Case and the pathline pattern is completely different compared to the Base Case and Variant 4. The use of environmental head in the boundary conditions for Variant 1 changes the flow pattern and sends the particles straight down through the model domain in an almost vertical direction. Like in the Saline Case, the major part of the particles exits through the bottom of the model. The exit locations are located around the major fracture zones near the northern repository. A few particles find their way up to the Imundbo Zone where they exit through the bottom of the model domain. The regional hydraulic gradient drives the particles in a northeast direction. A few particles started from the southern repository exit through the top of the model in a similar way to the pathlines in the Saline Case.

Table 8-6 shows the statistical summary for the particles exiting through the top of the model for the Saline Case and Variant 1. Since the major part of the released particles exit through the bottom of the model domain, the statistical analysis does not provide us with very useful data regarding the travel times. Comparing the canister flux for the two variants is still meaningful though and we see that the difference is small. The median canister flux for Variant 1 is $2.6 \cdot 10^{-3}$ m^3/m^2,year and for the Saline Case $3.8 \cdot 10^{-3}$ m^3/m^2,year. Note that the variance of $\log_{10}(CF)$ is much higher for Variant 1 compared to the Saline Case. The explanation to this might be that Variant 1 is a stochastic simulation while the Saline Case is a single realisation simulation.

Table 8-6 Statistical summary for the Saline Case and Variant 1.

	Saline Case			Variant 1		
Statistics	**$Log_{10}(TT_{top})$**	**$Log_{10}(TT_{bottom})$**	**$Log_{10}(CF)$**	**$Log_{10}(TT_{top})$**	**$Log_{10}(TT_{bottom})$**	**$Log_{10}(CF)$**
Median	1.709	1.562	-2.424	1.544	1.569	-2.588
25th Percentile	1.686	1.428	-2.506	1.279	1.260	-2.963
75th Percentile	1.714	1.734	-2.346	1.794	1.860	-2.198
Variance	0.003	0.067	0.028	0.259	0.191	0.474
Fraction	0.067	0.875	1.000	0.074	0.922	1.000

Table 8-7 summarises the net flow through the model boundaries for the Saline Case, the regional model and Variant 1. The regional model is the AltK case with saline water that was used generating the boundary conditions for the saline site scale models in NAMMU and HYDRASTAR (HYDRASTAR used the environmental head for the boundary conditions). The values for Variant 1 are presented as the arithmetic mean of five realisations. The two NAMMU models, the Saline case and the regional model, both show a discrepancy in the calculated mass balance. The explanation to this discrepancy was given above.

As can be seen in Table 8-7 considering the calculated flows the Saline Case shows quite good resemblance to Variant 1. Except for the bottom surface, the direction of the net flow is the same for all boundaries although the sizes of the flows differ. The only discrepancy is the flow through the bottom surface where the Saline Case shows an outflow while Variant 1 shows an inflow to the model. Considering the pathline pattern it is somewhat surprising to see an inflow through the bottom in Variant 1. The values for Variant 1 are generally larger than for the two NAMMU models. Comparing the flow through the top surface for the Saline Case to the regional model again we see the effect of different discretisation and fracture zone representation.

Table 8-7 Summary of groundwater net flow through the model boundaries for the Saline Case, the Regional Model and Variant 1. Positive flow is directed out from the model.

	Net Flow through Surface [$\cdot 10^{-3}$ m^3/s]		
Site Model Surface	**Saline Case**	**Regional Model**	**Variant 1**
Top	11.53	-2.32	6.73
Bottom	0.32	0.17	-3.09
South	-1.08	-2.31	-2.93
North	3.73	3.61	5.28
West	-3.82	-6.87	-9.39
East	1.72	4.13	3.36
Total Inflow	-4.90	-11.50	-15.40
Total Outflow	17.30	7.91	15.37
Mass balance	***12.40***	***-3.59***	***-0.03***

8.3 Future Work

Some possible tasks of great interest to study in the future are:

- Develop methods for modelling continuum site-scale hydrogeological models nested within continuum far-field models.
- Perform stochastic modelling with NAMMU (Monte Carlo, Turning Bands and conditioning).
- Study alternatives to stochastic flow simulations (Random Walk).
- Simulate coupled groundwater flow and salt transport (steady state and transient) for nested continuum models.
- Represent the uncertainty and variability in the hydrogeological properties to ensure that the results are not dependent on the discretisation. Nested models have to be discretised on a variety of scales to represent the physical processes. Hence, the geological information has to be upscaled in a consistent way.

The motivation for these developments is to extend the flexibility available to the modeller in representing physical processes and hydrogeological features, and hence improve the realism and accuracy of model predictions. In addition, approaches that may improve the efficiency of performing calculations could be evaluated.

9 References

Carlsson L., Winberg A., Arnefors J., 1986*, Hydraulic modelling of the final repository for reactor waste (SFR). Compilation and conceptualization of available geological and hydrogeological data.* **SKB Progress Report SFR 86-03**.

Cliffe K. A., Jackson C. P., Morris S. T., 1995*, Assessment Model Validity Document; NAMMU: A program for calculating groundwater flow and transport through porous media.* **SKB AR 95-11**.

Cliffe K. A., Morris S. T., Porter J. D., 1998*, Assessment Model Validity Document; NAMMU: A program for calculating groundwater flow and transport through porous media.* **SKB R-99-51**.

De Marsily G., 1981, *Quantitative Hydrogeology.* Academic press, Inc. pp. 80-82.

Gylling B., Walker D., Hartley L., 1999, *Site-scale groundwater flow modelling of Beberg.* **SKB TR-99-18**.

Hartley L., Boghammar A., Grundfelt B., 1998*, Investigation of the large scale regional hydrogeological situation at Beberg***. SKB TR-98-24**.

Hultman S., 1997, *Visualisation of HYDRASTAR simulation data in the AVS 5 system*. **SKB U-97-01**.

La Pointe P. R., Wallman P., Follin S., 1995, *Estimation of effective block conductivities based on discrete network analyses using data from the Äspö site*. **SKB TR 95-15**.

Lovius L., 1998, *Calculation of flux through boundaries in HYDRASTAR*. **SKB U-98-08**.

Marsic N., 1998*, Using Statistica and Matlab when evaluating results from HYDRASTAR 1.5+*. **SKB TS-99-04**.

Morris S. T., 1998, *NAMMU (Release 6.4) Technical Overview*, AEA Technology Report AEAT-2987.

Walker D., Rhen I., Gurban I., 1997*, Summary of hydrogeologic conditions at Aberg, Beberg and Ceberg.* **SKB TR 97-23**.

A 1 Analysing the Discrepancies

In order to estimate the variation in canister flux (Darcy velocity) in adjacent grid cells we can calculate the equivalent variation in the HYDRASTAR permeability field. We define the average variation as the sum of the permeability contrast between two adjacent grid cells divided by the mean of the two values taken over the entire grid, see below. For the permeability in the x-direction, the variation, V_k, is calculated as,

$$V_k = \frac{\sum_{K=1}^{N}\sum_{J=1}^{M}\sum_{I=1}^{L}\left(\frac{\left|k_X(I+1,J,K)-k_X(I,J,K)\right|}{0.5\cdot(k_X(I+1,J,K)+k_X(I,J,K))}\right)}{L\cdot M\cdot N}$$

where L, M and N are the number of elements in the three directions respectively. This can then be compared with the difference of the calculated parameters, the canister flux and the travel time, in the BaseFine Case (NAMMU) and Variant 4 (HYDRASTAR). We do this by comparing the values in the two models for one parameter at the time (the canister flux and the travel time respectively) as,

$$D_{CF,TT} = \frac{\sum_{n=1}^{N}\left(\frac{\left|P_n^{NAMMU}-P_n^{HS}\right|}{0.5\cdot(P_n^{NAMMU}+P_n^{HS})}\right)}{N}$$

where N is the number of particles released (120) and P is the parameter measured (the canister flux (CF) or the travel time (TT)) in each of the two models (NAMMU and HYDRASTAR). The absolute value of the numerator in the sum was taken. The results of the calculations are presented in Table A - 1.

Table A - 1 Summary of the calculated variations and differences in the logarithmic and the linear scale.

	Logarithmic [%]	Linear [%]
V_{kX}	2.8	19
V_{kY}	2.9	19
V_{kZ}	3.2	24
D_{CF} *(Canister flux)*	4.8	21
D_{TT} *(Travel time)*	39	103

The calculated variation of the permeability values gives us an estimate of the effect of moving the point used for calculating the canister flux by half a grid cell in each coordinate direction. This can symbolise the difficulties when translating a HYDRASTAR permeability field to NAMMU. In other words, if we moved the point where we calculate the velocity by half a grid cell, we would change the velocity proportionally to the change in permeability. The calculated variations in the permeability values (k_X, k_Y and k_Z) are very similar to the calculated difference in the canister flux (Darcy velocity). This suggests that the discrepancy is most probably due to the different representation of the permeability in the two models. Likewise, the calculation of velocities at an arbitrary point is also affected by the numerical scheme used (finite difference in HYDRASTAR, finite element in NAMMU), see Figure A - 1.

Ideally, one would like to derive the permeability as a continuous field and then interpolate the field onto a particular discretisation as required. This may reduce the differences between different solution methods. However, there will inevitably be difference of the order of the variation in permeability on the scale of mesh spacing, because of the discrete representation of the permeability field. In this case, these variations are of the order of 20% in the absolute value, or 3% in the logarithm.

The variations of the travel times are much higher (a factor 5-10) than for the canister fluxes (Darcy velocities). This is expected though, since the calculation of pathlines is more sensitive to the variations in a heterogeneous permeability field. The calculation of pathlines is also affected by the discretisation and algorithm used to compute them.

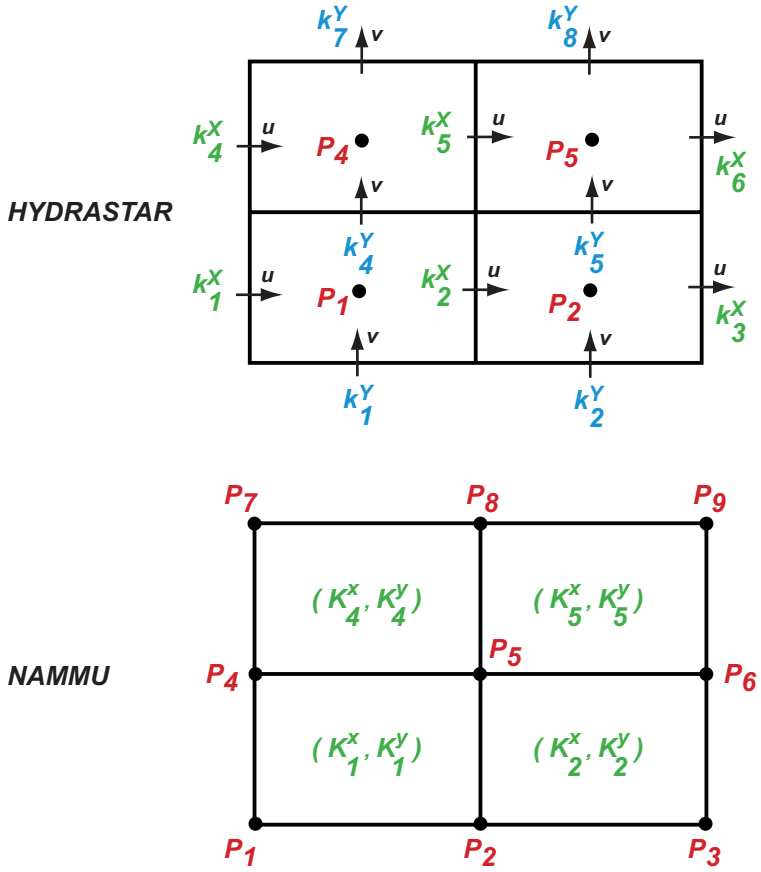

Figure A - 1 *A 2D illustration of the different numerical schemes used by HYDRASTAR and NAMMU. HYDRASTAR defines the hydraulic conductivity on the element sides while NAMMU defines the permeability on the element volume. The pressure and thus the velocity are also calculated in different places comparing the two codes. This is the reason for the discrepancy in the calculated Darcy velocities and travel times. [La Pointe et al., 1995] [Morris, 1998] [Lovius, 1998]*

A 2 Inclusion of an Iterative Solver in NAMMU

L.J. Hartley and M.J. Poole, AEA Technology, Harwell, U.K.

A 2.1 Introduction

The site-scale modelling performed in this study used finely discretised 3D grids with approximately ¾ million degrees of freedom. The computational size of these meshes created difficulties for the NAMMU code. The standard solver in NAMMU is a direct frontal method. This is robust and accurate for a wide range of physics, high permeability contrasts and non-linear problems, such as coupled flow and salt transport. However, it scales poorly in terms of memory and CPU times for very large problems.

Typically, for a mesh with N^3 nodes, i.e. N nodes in each direction, the cost of a calculation is about N^7 with the frontal method, and hence the cost of running large grids becomes prohibitive. In practical terms, it is difficult to run models with more than about 0.5 million degrees of freedom using the frontal method.

The cost of iterative methods generally increases less rapidly for large meshes, N^3 to N^4, but they can be less robust and the accuracy has to be checked. Under this task, an iterative method based on Pre-Conditioned Conjugate Gradients (PCCG) was incorporated in NAMMU to test its performance. The Generalised Minimum Residual (GMRES) conjugate gradient scheme was used with an Incomplete LU factorisation (ILU) preconditioner. Three models were used to compare accuracy, robustness and performance of the solver methods. These models were: the Beberg regional model (TR 98-24); the Ceberg small regional scale model (TR 97-21); and the Beberg site scale model (used in this report). Results, in terms of freedom values, were compared between the PCCG and frontal methods to check accuracy. The CPU times, as well as memory and disk requirements, were noted to measure the benefit of using the PCCG method. It should be noted that these times are only indicative, since PCCG methods tend to perform less well when the permeability contrasts are increased or the matrices become poorly condition, e.g. due to non-linearities.

A 2.2 PCCG Solver Performance

The PCCG solver had already been tested for steady-state problems using a prototype version that was quite memory intensive. The main objectives of this task were to reduce the memory required for the solver, to calculate automatically the amount of memory required and to implement the solver for all subcommands of >> SOLVER DATA (e.g transients and salt transport). In addition, it was found necessary to add a node renumbering option for irregular grids (see conclusions below). The solver was tested on a number of models – aspects of its performance are given in the tables below.

A 2.2.1 Beberg regional model

Table A - 2 Performance Beberg regional model.

Physics and Solver method	Elements	CPU	Memory (total for run)	Disk (for solver alone)
Hydrostatic pressure variable PCCG solver	3278 CBQL	*** UNSOLVABLE *** (Hydrostatic pressure equation unsuitable for solution with PCCG solver)		
Steady-state solve for Pressure Frontal method	3278 CBQL	Assembly 29 s Solver 317 s Total 345 s	Integer 8 Mb Real 16 Mb	320 Mb
Steady-state solve for Pressure PCCG solver	3278 CBQL	Assembly 35 s Solver 149 s Total 184 s	Integer 24 Mb Real 48 Mb	0 Mb
Transient solve for Pressure and Salt (1 N-R iteration) Frontal method	3278 CBQL	Assembly 60 s Solver 559 s Total 619 s	Integer 12 Mb Real 24 Mb	60 Mb
Transient solve for Pressure and Salt (1 N-R iteration) PCCG solver	3278 CBQL	Assembly 76 s Solver 329 s Total* 406 s	Integer 36 Mb Real 104 Mb	0 Mb

**Typical value – actually the time taken varies for different Newton-Raphson iterations.*

For small problems like this, the improvement in CPU is only about a factor of two, and the memory requirement is actually greater for PCCG. Hence, the benefits are limited for this model because:

1. it is not a large model in terms of the number of elements.

2. it uses quadratic elements which increases both the number of equations (by about a factor 2 for groundwater flow) and the number of non-zeros per equation (by about a factor 4 for groundwater flow).

This example shows that the PCCG method can be employed for both salt transport and transient models.

A 2.2.2 Ceberg regional model

Table A - 3 Performance Ceberg regional model.

Solver method	Elements	CPU	Memory (total for run)	Disk (for solver alone)
Frontal method	38870 CB08	Assembly 44 s Solver 1361 s Total 1405 s	Integer 20 Mb Real 16 Mb	432 Mb
PCCG solver	38870 CB08	Assembly 37 s Solver 16 s Total 53 s	Integer 20 Mb Real 24 Mb	0 Mb

For this case, the improvement is more dramatic. The Solver time is reduced by a factor of 100. In fact, the total solver time is now dominated by assembling the finite-element equations.

A 2.2.3 Beberg site-scale model

Table A - 4 Performance Beberg site-scale model.

Model and solver method	Elements	CPU	Memory (total for run)	Disk (for solver alone)
Small model Frontal method with domain decomposition	192812 CB08	Total 7557 s	Integer 112 Mb Real 176 Mb	3488 Mb
Small model PCCG solver	192812 CB08	Assembly 282 s Solver 251 s Total 533 s	Integer 136 Mb Real 128 Mb	0 Mb
Large model Frontal method	746928 CB08	*** UNSOLVABLE *** (due to LU decomposition filling disk)		
Large model PCCG solver	746928 CB08	Assembly 1002 s Solver 1513 s Total 2515 s	Integer 300 Mb Real 448 Mb	0 Mb
Large model Old memory-intensive version of PCCG solver	746928 CB08	Assembly 1051 s Solver 1525 s Total 2575 s	Integer 496 Mb Real 824 Mb	0 Mb

Again, the PCCG method demonstrates an improvement of a factor 30 for the small model, and allows the large model to be solved where it was impossible for the frontal method. The memory requirements for both methods are similar, though slightly less for the PCCG. The PCCG memory requirements are mainly in storing the matrix. The memory requirements have been significantly reduced from the prototype version.

A 2.3 Conclusions

- All solutions obtained with the PCCG method were consistent with those from the frontal method.

- The solver performs well for groundwater flow problems (Ceberg and Beberg site-scale). The new memory allocation method saves a significant amount of memory. The reduction in CPU times is very significant even for problems with heterogeneity, e.g. there are about four orders of magnitude contrast in permeability for the Beberg site-scale model. In removing the need to store large temporary files on the harddisk, solving large models is far less prohibitive.

- For highly irregular grids, some renumbering of the nodes was found necessary. This is because NAMMU renumbers elements, not nodes. A simple node renumbering algorithm has been implemented which assumes that the elements have already been renumbered using Sloan algorithm. This was found to improve performance considerably on the Beberg regional model. However, for a very regular grid such as the Beberg site-scale model, performance was reduced. Hence, the renumbering has been left as an option for the user. It is recommended that further attention be given to the issue of node renumbering.

- For salt transport (and other 'difficult' calculations) it was found that a large number of Krylov basis vectors was required to achieve good convergence. Having noted this, the transient salt transport for the Beberg regional model was solved with the Newton-Raphson iterator without any problems. For groundwater flow, the default value of 10 was adequate. Note that a large number of Krylov basis vectors can require a large amount of memory. This may become an issue for large salt transport calculations with highly saline groundwater.

- For difficult non-linear calculations it may be necessary to use more sophisticated preconditioners. A natural choice would be a pivoting ILU method. The current method does not use any fill-in.

- The improvement in performance over the frontal method is very significant, two orders of magnitude for large meshes. This improvement is not as marked when quadratic elements are used (e.g. in the Beberg regional model). Better performance may be gained using a more refined grid of linear elements (e.g. CB08 elements), although for salt transport this may mean that the salt variable is over determined. Experimentation with different element types for coupled salt transport and flow would help clarify this point.

- A significant component of the CPU and disk requirements is now related to the assembly of the finite-element equations. This could be improved by some

restructuring of the code. For steady-state calculations, this may at most yield a factor of two in total CPU. However, for transient calculations the assembly time may dominate since the matrix may have to be reassembled each time-step (e.g. for non-linear problems), while the solver only takes a few iterations to step from one time to the next.

- The PCCG solver will not solve the hydrostatic pressure equation used in the Beberg regional model. An alternative method for setting a hydrostatic boundary condition for variable density flows should be sought, e.g. using NAMMU's 'nodal law' type boundary condition.

A 3 Tools Used

One of the objectives in this study was to evaluate the latest NAMMU version, NAMMU 7.0, that includes a completely new graphical user interface (GUI). Furthermore, the latest version of the visualisation software AVIZIER was used for the major part of the post processing of the simulation results. The experiences from the work with AVIZIER will also be discussed.

A 3.1 NAMMU

The technical capabilities of the latest version of NAMMU are extensive and will only be listed here very briefly. Further reading can be found in the Technical Overview that can be provided by AEA Technology *[Morris, 1998]*.

Here follows a short list of the capabilities of NAMMU Release 6.4, which has the same functionality as Release 7.0 except that the latter has the newly developed GUI included. NAMMU 7.0 is currently supported on Windows NT, Silicon Graphics, Sun and IBM RS/6000 *[Hartley et al., 1998]*.

NAMMU can be used to calculate:

- *Groundwater flow*
- *Coupled groundwater flow and heat transport*
- *Unsaturated groundwater flow*
- *Coupled groundwater flow and solute transport with the fluid density strongly dependent upon concentration*
- *Coupled groundwater flow, heat transport and solute transport with the fluid density dependent upon concentration and temperature*
- *Radionuclide transport (which may take place in the groundwater flow field of any of the above except coupled groundwater flow, heat transport and solute transport with the fluid density dependent upon concentration and temperature)*
- *The stream function in two dimensions*
- *Adjoint sensitivity analysis*

The conceptual models underlying all of these processes are flow and transport in a porous medium, modelled by Darcy's law and its extensions. The radionuclide transport model includes a linear equilibrium sorption model, and chains of up to six radionuclides can be considered. A detailed presentation of the mathematical models used is given in the NAMMU Technical Overview *[Morris, 1998]*.

NAMMU uses the finite-element method, which enables complicated geometries with many different rock types to be readily modelled in a straightforward fashion. Options for transient calculations include Crank-Nicholson and Gear's method. Non-linear cases

can be tackled using Newton-Raphson linearisation, supplemented with parameter stepping. The algebraic equations resulting from linearisation in space (and time, if necessary) are solved using a very fast direct linear solver from the Harwell Subroutine Library *[Hartley et al., 1998]*.

Recently a new iterative solver was implemented into NAMMU. This solver together with pre conditioner, called GMRES/ILU, proved to be much faster (a factor 300 in some cases!) than the direct solver used earlier. Another benefit is a more economical use of primary and secondary memory. This solver was used in the BaseFine Case and enabled full discretisation in the model compared to the Base Case where the discretisation was reduced a factor two in the x and y directions in order to reduce the number of elements and speed up the simulation times. A parallel project is currently running where the solver is fully implemented, tested and evaluated in NAMMU.

The newly developed GUI, included in NAMMU Release 7.0, is an attempt to change the way of work with "command line" groundwater modelling codes by shifting from program-centric input files (based on how program works) to user-centric method (based on tasks user wants to perform). The GUI uses an object approach with high-level objects and actions, not step-by-step instructions. The users work with projects, not individual input files. The GUI has backward compatibility in the sense that it can still use input files. A great deal of QA is embedded thanks to automatic file handling that keep track of all files used and generated so that files can not be erased by mistake if they are used by other files. When working with the GUI, available choices are presented clearly to the user and ensures that the user supplies all relevant input related to the task. The GUI is written in Java and is therefore platform independent with a consistent interface across different platforms.

Other features included are:

- *Automatic error checking*
- *Support of advanced features - user Fortran etc.*
- *Can run without a compiler (if no user Fortran)*
- *Automatic monitoring of jobs*
- *Every parameter is given a default*

The limitations can be summarised as:

- *Beta version only - some advanced features are missing and there are still bugs in the code that has not yet been thoroughly tested*
- *No graphical grid generator*
- *No automatic boundary condition generator*
- *GUI supports documented functionality of NAMMU, if the user relies on some trick the GUI may not be able to reproduce this*

- *Can not use scripts to generate input files*
- *Needs more memory*
- *The GUI and the source code have to be on the same platform due to different file systems on different platforms*

One big disadvantage with NAMMU at the moment is that the code uses an extreme amount of disk space during the calculations. These intermediate files are later erased but need several gigabytes (up to 25 GB for a model with 800 000 elements) during the calculations. AEA Technology has plans on cleaning up the code in order to fix this problem. Some of these problems have been reduced implementing the new iterative solver.

The benefits of the GUI are, hopefully, more productive users who can focus on groundwater modelling instead of details of how the program works. The introduction and learning phase should be shorter and fewer errors done by the user. Since the GUI is the interface between the user and the code and handles the communication, the reference manual is no longer required.

Because of some problems with the GUI at the start of this project and the tight time schedule, a decision was made not to use the GUI at this point but wait until some testing has been done. This means that the simulations performed within this project was made using the command line version of NAMMU, Release 6.4.

A 3.2 AVIZIER

Output from NAMMU can be visualised with the built-in routines in NAMMU or if preferred, one may use the visualisation software AVIZIER that is more user friendly. NAMMU exports input files for AVIZIER.

The major part of the post-processing has been carried out with a demo license of AVIZIER 2.0 *[http://www.bssi.no/]*. AVIZIER is a software environment for three-dimensional visualisation of geoscience data developed by Bergen Software Services International A/S, BSSI in Bergen, Norway. AVIZIER is built using the software system Iris Explorer from NAG *[http://www.nag.co.uk/]*.

Both the AVIZIER and the Iris Explorer used were beta versions and therefore not entirely functioning. As an example there was no support in IRIS Explorer for creating legends in the figures, which explains why they are missing in this report. This function will be corrected in the final release of the software though.

AVIZIER visualises in three-dimensions the model grid, the rock types, the permeability field and all variables solved for in the NAMMU simulation. Pathlines are calculated using the same routines as in NAMMU. Slices, iso-surfaces and vector plots can be generated. However, there are still a lot to ask for in AVIZIER. One of the major tasks is the extreme memory demand when performing some of the operations listed above. Use of up to 600 MB RAM has been experienced generating some of the figures within this report. In addition, the AVIZIER input files generated in NAMMU grow quite quickly. Files with a size of up to 90 MB were generated for this model. The reason for this is that the files are generated in ascii format. It is not possible to define user functions in AVIZIER if one would like to visualise something special. There is still some work to be done providing the user with the possibilities of automating the work with generation of the figures.

A 4 Quality Assurance

This section contains the file locations for the NAMMU input and output data files. In addition, a list of all the figures used in the report is given. All files have been written to a CD-ROM together with the final report.

A 4.1 File Location

All files are stored on AEA Technology's UNIX file server *abel* (IP 151.182.136.3). Table A - 5 and Table A - 6 list all input and output data files used within NAMMU.

Table A - 5 Summary of files and locations for files used in the simulations.

File Location / *File Name*	*File Size [byte]*	*Date*
/net/abel/vp0/kemakta/beberg/userfiles		
cintby.f	3 029	1999-03-15
conduc_1.dta	16 302 762	1998-11-27
conduc_fine.dta	34 358 688	1999-06-09
grlfresh62a.gfs	530 144	1998-11-30
grlmdls62.mdl	1 919 947	1998-11-30
grltrans62a.gfs	530 144	1998-11-30
perani.f	3 312	1998-11-30
perfine.f	3 744	1999-08-12
perusr.f	3 086	1998-11-30
sclusr.f	1 873	1999-03-05
/net/abel/vp0/kemakta/beberg/domaincode		
bdpcon.f	12 176	1998-11-26
libfeature.6.4.domain.sg-r8000.a	720 084	1998-12-08
monster.o	549 504	1998-12-03
/users/kemakta/beberg/base_new/source/		
crankc.f	18 767	1999-08-11
dslugm.f	252 567	1999-08-11
nlus.f	9 103	1999-08-11
nlusby.f	9 148	1999-08-11
phs2by.f	12 782	1999-08-11
stedyc.f	14 973	1999-08-11
/net/abel/vp0/kemakta/beberg/tests		
kfield_big.dat	9 999	1998-12-04
kfield_big.ml	22 060 075	1998-12-04
kfield_big.out	31 266	1998-12-04

Table A - 6 Summary of files and locations for the case specific files.

File Location / *File Name*	*File Size*	*Date*
/net/abel/vp0/kemakta/beberg/base		
Base_flux.dat	8 213	1999-03-17
Base_flux.out	19 254	1999-03-17
Base_path.dat	18 243	1999-01-04
Base_path.out.gz	4 257 476	1999-01-04
kfield_sol.avz.gz	18 430 382	1998-12-07
kfield_sol.dat	7 701	1998-12-07
kfield_sol.gf	4 879 144	1998-12-07
kfield_sol.out.gz	6 800	1998-12-07
/net/abel/vp0/kemakta/beberg/base_fine		
flux05.dat	8 174	1999-09-02
flux05.out	19 215	1999-09-02
kfield05a.dat	9 931	1999-08-13
kfield05a.ml	78 743 179	1999-08-13
kfield05a.out	18 509	1999-08-13
kfield05b.dat	4 379	1999-08-13
kfield05b.gf	6 211 000	1999-08-13
kfield05b.out	12 336	1999-08-13
kfield05c.avz.gz	41 439 040	1999-08-16
kfield05c.dat	8 195	1999-08-16
kfield05c.gf	6 211 000	1999-08-16
kfield05c.out	25 020	1999-08-16
path05.dat	18 346	1999-08-16
path05.out.gz	13 655 922	1999-08-16
path05.ps	1 982 557	1999-08-16
/net/abel/vp0/kemakta/beberg/anisotropy		
Anisotropy_flux.dat	8 213	1999-03-17
Anisotropy_flux.out	19 254	1999-03-17
Anisotropy_path.dat	18 387	1999-01-04
Anisotropy_path.out.gz	16 996 459	1999-01-04
kfield_sol_ani.avz.gz	13 113 372	1998-12-08
kfield_sol_ani.dat	7 713	1998-12-07
kfield_sol_ani.gf	4 879 144	1998-12-08
kfield_sol_ani.out.gz	6 794	1998-12-08
/net/abel/vp0/kemakta/beberg/salinity		
Salinity_flux.dat	8 314	1999-03-17
Salinity_flux.out	19 355	1999-03-17
Salinity_path.dat	18 371	1999-01-04
Salinity_path.out.gz	5 102 924	1999-01-04
kfield_sol_salt.avz.gz	14 225 399	1998-12-08
kfield_sol_salt.dat	7 821	1998-12-07
kfield_sol_salt.gf	4 879 144	1998-12-08
kfield_sol_salt.out	47 641	1998-12-08

A 4.2 List of Figures

The file names for the majority of the figures used in the report are listed in Table A - 7 and Table A - 8. The figures produced with Statistica are listed in Table A - 9. Since Statistica uses an automatic procedure giving names to the figures, the corresponding figures will have the same name for different variants.

Table A - 7 Summary #1 of image files generated.

File Name	*File Size*	*Date*	*Figure*
MODEL&TUNNELS.WMF	81 500	1999-02-09	Figure 3-1
PLNEQNlarge4.XLS	1 189 376	1998-12-01	Figure 3-2
PLNEQNlarge4.XLS	1 189 376	1998-12-01	Figure 3-3
HYDRAST_cond.eps	249 554	1999-09-17	Figure 3-4
AVS_cond.eps	250 646	1999-09-17	Figure 3-5
NAMMU_cond.eps	182 754	1999-09-17	Figure 3-6
BOX_DESCRIPTION.EPS	233 194	1999-03-19	Figure 3-8
BASE_P.TIF	853 178	1999-01-20	Figure 4-1
BASE_CH.TIF	843 412	1999-01-19	Figure 4-2
BASE_CV.TIF	872 196	1999-01-19	Figure 4-3
BASE_CH_XZ.TIF	914 230	1999-01-27	Figure 4-4
BASE_CH_YZ.TIF	915 498	1999-01-27	Figure 4-5
BASE_P_XZ.TIF	914 546	1999-01-27	Figure 4-6
BASE_P_YZ.TIF	913 262	1999-01-27	Figure 4-7
BASE_PATH.EPS	3 837 538	2000-02-04	Figure 4-8
BASE_EXITLOC.WMF	102 248	1999-02-09	Figure 4-9
BASE_FLOW.EPS	331 002	1999-03-10	Figure 4-10
BASEF_P.TIF	3 869 018	1999-12-21	Figure 5-1
BASEF_CX.TIF	3 978 218	1999-12-21	Figure 5-2
BASEF_CX_XZ.TIF	4 266 638	1999-12-21	Figure 5-3
BASEF_CX_YZ.TIF	4 266 638	1999-12-21	Figure 5-4
BASEF_P_XZ.TIF	4 266 638	1999-12-21	Figure 5-5
BASEF_P_YZ.TIF	4 266 638	1999-12-21	Figure 5-6
BASEFINE_PATH.EPS	5 014 798	2000-02-04	Figure 5-7
BASEFINE_EXITLOC.WMF	102 572	1999-09-02	Figure 5-8
BASEFINE_FLOW.EPS	344 698	1999-09-15	Figure 5-9
MATHEMATICALFORM.EPS	208 162	1999-09-29	Figure A - 1

Table A - 8 Summary #2 of image files generated.

File Name	*File Size*	*Date*	*Figure*
ANI_CH.TIF	859 822	1999-01-19	Figure 6-1
ANI_CV.TIF	863 824	1999-01-19	Figure 6-2
ANI_CH_XZ.TIF	915 272	1999-01-27	Figure 6-3
ANI_CH_YZ.TIF	916 230	1999-01-27	Figure 6-4
ANI_P_XZ.TIF	914 122	1999-01-27	Figure 6-5
ANI_P_YZ.TIF	915 122	1999-01-27	Figure 6-6
ANI_PATH.EPS	6 241 942	2000-02-04	Figure 6-7
ANI_EXITLOC.WMF	101 938	1999-02-09	Figure 6-8
ANI_FLOW.EPS	331 018	1999-03-10	Figure 6-9
SAL_P.TIF	847 666	1999-01-19	Figure 7-1
SAL_S.TIF	857 038	1999-01-19	Figure 7-2
SAL_P_XZ.TIF	914 436	1999-01-27	Figure 7-3
SAL_P_YZ.TIF	913 232	1999-01-27	Figure 7-4
SAL_S_XZ.TIF	915 252	1999-01-27	Figure 7-5
SAL_S_YZ_TXT.TIF	914 038	1999-09-27	Figure 7-6
SAL_S_C03YZ_TXT.TIF	914 936	1999-09-27	Figure 7-7
SAL_S_C08YZ_TXT.TIF	914 850	1999-09-27	Figure 7-8
SAL_S_C03.TIF	914 582	1999-01-27	Figure 7-9
SAL_S_C08.TIF	914 686	1999-01-27	Figure 7-10
SAL_PATH.EPS	2 735 782	2000-02-04	Figure 7-11
SAL_EXITLOC.WMF	102 560	1999-02-09	Figure 7-12
SAL_FLOW.EPS	328 638	1999-03-10	Figure 7-13

Table A - 9 Summary of files generated with Statistica for all variants.

File Name	*Base Case*	*BaseFine Case*	*Anisotropic Case*	*Saline Case*
HISTTlg1.STG	Figure 4-11	Figure 5-10	Figure 6-10	Figure 7-14
HISTTlg5.STG	Figure 4-12	Figure 5-11	Figure 6-11	Figure 7-15
BOXTTlg1.STG	Figure 4-13	Figure 5-12	Figure 6-12	Figure 7-16
HISCFlg1.STG	Figure 4-14	Figure 5-13	Figure 6-13	Figure 7-17
HISCFlg4.STG	Figure 4-15	Figure 5-14	Figure 6-14	Figure 7-18
BOXCFlg1.STG	Figure 4-16	Figure 5-15	Figure 6-15	Figure 7-19
SCA_lglg.STG	Figure 4-17	Figure 5-16	Figure 6-16	Figure 7-20

A 4.3 Variants

Table A - 10 summarises the input for the variants performed.

Table A - 10 Summary of input data used for all variants.

	Base Case	BaseFine Case	Anisotropic Case	Saline Case
Grid	kfield_big.ml	kfield05a.ml	kfield_big.ml	kfield_big.ml
HYDRASTAR permeability field obtained from	HYDRASTAR Variant 4, Permeability resultant	HYDRASTAR Variant 4, Permeability components	HYDRASTAR Variant 4, Regional Anisotropy (N 45 W)	HYDRASTAR Variant 4, Permeability resultant
Regional NAMMU variant supplying the Dirichlet Boundary Conditions	grlfresh62a.gfs	grlfresh62a.gfs	grlfresh62a.gfs	grltrans62a.gfs
Regional NAMMU variant supplying the salt concentration	-	-	-	grltrans62a.gfs
Regional NAMMU model used	grlmdls.mdl	grlmdls.mdl	grlmdls.mdl	grlmdls.mdl
Permeability file	conduc_1.dta	conduc_fine.dta	conduc_1.dta	conduc_1.dta
NAMMU data file (solves the groundwater flow equations for the residual pressure)	kfield_sol.dat	kfield05a.dat kfield05b.dat kfield05c.dat	kfield_sol_ani.dat	kfield_sol_salt.dat
NAMMU pathline file	Base_path.dat	path05.dat	Anisotropy_path.dat	Salinity_path.dat
NAMMU boundary flow file	Base_flux.dat	flux05.dat	Anisotropy_flux.dat	Salinity_flux.dat
Corresponding HYDRASTAR variant	Variant 4	Variant 4	-	Variant 1